Structure and Function of Aquaporins

Inauguraldissertation

zur
Erlangung der Würde eines Doktors der Philosophie
vorgelegt der
Philosophisch-Naturwissenschaftlichen Fakultät
der Universität Basel

von

Wanda Kukulski
aus Visp VS

Basel, 2006

Genehmigt von der Philosophisch-Naturwissenschaftlichen Fakultät
auf Antrag von
Prof. Dr. Andreas Engel & Prof. Dr. Per Kjellbom

Basel, den 21.11.2006

Prof. Dr. Hans-Peter Hauri
Dekan

Ich erkläre, dass ich die Dissertation "Structure and Function of Aquaporins" nur mit der darin angegebenen Hilfe verfasst und bei keiner anderen Universität und keiner anderen Fakultät der Universität Basel eingereicht habe.

Wanda Kukulski

Contents

1 Introduction 1
1.1 Biological Membranes and Membrane-spanning Proteins 1
1.2 Aquaporins 2
1.2.1 Human aquaporins 4
1.2.2 Plant aquaporins 5
1.2.3 Aquaporins are multifunctional proteins 7

2 Structure and Function of SoPIP2;1 9
2.1 Introduction 10
2.1.1 SoPIP2;1 - Structure determination of a plant aquaporin 10
2.1.2 Investigations on the mechanism of regulation of SoPIP2;1 11
2.2 Results: Wild Type SoPIP2;1 13
2.2.1 Purification and 2D crystallization of wild type SoPIP2;1 13
2.2.2 Structural analysis: The 5 Å structure determined by electron crystallography 15
2.2.3 Electron diffraction on SoPIP2;1 crystals 16
2.2.4 Phosphorylation and dephosphorylation of SoPIP2;1 2D crystals 19
2.2.5 Defining the phosphorylation state of 2D crystallized SoPIP2;1 by mass spectroscopy 22
2.3 Results: Mutants of SoPIP2;1 24
2.3.1 Expression of alanine and aspartate mutants of phosphorylation sites S115 and S274 24
2.3.2 Purification and 2D crystallization of mutant SoPIP2;1 forms 27
2.3.3 Structural analysis by electron crystallography 30
2.4 Results: Water Channel Activity of Wild type and Mutant SoPIP2;1 30
2.5 Discussion: Wild Type SoPIP2;1 31
2.5.1 2D crystallization of wild type SoPIP2;1 31
2.5.2 The 5 Å structure of SoPIP2;1 32

2.5.3 Phosphorylation and dephosphorylation of 2D crystals of SoPIP2;1 . . 32
2.5.4 Determination of the phosphorylation state of 2D crystallized SoPIP2;1 by mass spectroscopy 34
2.6 Discussion: Mutants of SoPIP2;1 36
2.6.1 Expression and purification of SoPIP2;1 mutants 36
2.6.2 2D crystallization and structural analysis of SoPIP2;1 mutants 37
2.7 Discussion: Water Channel Activity of Wild Type and Mutant SoPIP2;1 39
2.8 Materials and Methods 40
2.8.1 Purification and 2D crystallization of wild type SoPIP2;1 40
2.8.2 Electron microscopy 41
2.8.3 Electron diffraction 41
2.8.4 Image processing and structure determination 42
2.8.5 Phosphorylation and dephosphorylation of 2D crystals of SoPIP2;1 . . 46
2.8.6 Mass spectroscopy of reconstituted SoPIP2;1 47
2.8.7 Alanine and aspartate mutants of phosphorylation sites S115 and S274 48
2.8.8 Purification and 2D crystallization of mutants of SoPIP2;1 50
2.8.9 Electron diffraction 51
2.8.10 Activity assays 51
2.9 Conclusions 51

3 AQP8 **55**

3.1 Introduction 56
3.2 Results 57
3.2.1 Solubilization and stability 57
3.2.2 Single particles and sample homogenity 58
3.2.3 Screening for 2D crystallization conditions 60
3.2.4 Preliminary image processing 61
3.2.5 Water channel activity 61
3.3 Discussion 65
3.3.1 Purification 65
3.3.2 2D crystallization 66
3.3.3 Water channel activity 67
3.4 Materials and Methods 69
3.4.1 Solubilization and purification 69
3.4.2 Detergent screen and stability 69
3.4.3 Single particles and sample homogenity 70

3.4.4 Screening for 2D crystallization conditions 70
3.4.5 Activity assays 70
3.5 Conclusions and Outlook 71

A The 5 Å Structure of Heterologously Expressed SoPIP2;1 73

B Controlled 2D Crystallization of Membrane Proteins Using Methyl-β-Cyclodextrin 81

Abbreviations 91

Acknowledgements 101

List of Figures

1.1 Water permeation through AQP1 4

2.1 Two crystal forms of SoPIP2;1 14
2.2 Projection maps of single- and double-layered crystals 15
2.3 Symmetry of the double-layered crystals 16
2.4 An example for lattice line fitting: Lattice line (6,4) 17
2.5 The SoPIP2;1 potential map superimposed with the atomic model of AQP1 . . 18
2.6 Phosphorylation of SoPIP2;1 crystals using γ-^{32}P-ATP and PKC 20
2.7 Dephosphorylation reaction with Alkaline Phosphatase 22
2.8 Phosphorylation with γ-^{32}P-ATP following dephosphorylation 23
2.9 Nucleotide and amino acid sequence of SoPIP2;1 25
2.10 S115 and S274 mutants: Screen for best expressing clones 26
2.11 S115 and S274 mutants: Time course of expression 27
2.12 SDS-PAGE: Purfication of SoPIP2;1 mutants 28
2.13 2D crystals of SoPIP2;1 mutants 29
2.14 Activity of SoPIP2;1 wild type and mutants 30
2.15 Sequence alignment of SoPIP2;1 to PvTIP3;1 35
2.16 Electron diffraction on S274A 2D crystals 38
2.17 Overview of the automated image processing proceeding 42
2.18 Steps in the first round of unbending: Job2000a 43
2.19 The second round of unbending: Job2000b 44

3.1 AQP8 detergent screen 57
3.2 Purification in four different detergents 59
3.3 Single particles of AQP8 59
3.4 Crystallization trials using different lipids 60
3.5 2D crystals of AQP8 62
3.6 Proteoliposomes of AQP8 at different LPRs 63
3.7 Water transport activity of reconstituted AQP8 64

Chapter 1

Introduction

1.1 Biological Membranes and Membrane-spanning Proteins

The most simple definition of a living cell is that of an aqueous volume segregated into compartments and surrounded by biological membranes. To overcome the boundaries set by compartmentalization, the biological membranes contain proteins that specifically modify the membrane barrier, e. g. for the uptake of nutrients, water transport, sensing changes in the environment, signal reception and emission to communicate with neighbouring cells, and to maintain gradients ensuring energy storage. All these processes are tightly controlled and kept in a fine balance. In 1972, the 'fluid mosaic model' developed by Singer and Nicholson [1] described how membrane proteins are dispersed in a membrane, exposing a belt of hydrophobic residues to cope with the hydrophobic core of the lipid bilayer. Since then, however, many years of extensive research provide a much more complex picture. A revised model describes membranes as rather mosaic than fluid [2]: The distribution of membrane proteins in the lipid bilayer is not random as described by the Singer-Nicholson model, but segregated regions of specific protein composition exist to fulfill specialized functions. Moreover, the picture of membrane proteins organized in large functional complexes starts to emerge. A second correction of the Singer-Nicholson model concerns the crowdedness of biological membranes, which seems to be much higher than assumed. Additionally, many membrane proteins have in fact small membrane-spanning domains, but large ectodomains covering the surface of the membrane bilayer. Finally, the fluidity of the lipid bilayer does not necessarily imply unrestricted diffusion of proteins within the membrane plane. Their mobility is constrained by changing lipid composition, variations in membrane thickness, crowding, collisions with other membrane proteins or interactions with the cytoskeleton. When thinking of a cell's biological membrane, one should also consider the many different specializations of living cells (and cellular organelles), which are very often reflected by highly specific functions of the membrane. This gives an even more variable picture of biological membranes. As examples for highly specialized membranes one can think of the photosynthetic apparatus in thylakoid membranes or the respiratory chain complex in mitochondria.

1.2 Aquaporins

Water is the most abundant molecule in living organisms. It is the solvent for biochemical reactions and its properties result in the hydrophobic effect, which is the fundamental phenomenon that dictates the assembly of biological membranes. To pass the barrier formed by the lipid bilayer, water molecules need an activation energy of 10 - 20 kcal/mol [3]. However, plasma membranes of some cell types like red blood cells, secretory glands or renal tubules exhibit water transport rates that cannot be explained by spontaneous water diffusion through the bilayer. First evidence that these properties were due to the existence of proteinaceous pores that reduce the energy barrier to $E_a < 5$ kcal/mol was given by the observation that water permeability is inhibited by mercurials and can be reversed by reducive agents, suggesting that a reaction with cysteine residues somehow closes the water channel [4]. It has also been observed that although water permeability of red blood cells is high, no H^+ ions can pass the cell membrane, indicating that either a specific arrangement of charge exists or the water molecules within the channel do not form a continuum [4]. It was, however, only in 1992 when CHIP28, later renamed into Aquaporin-1 (AQP1), was discovered to be the water channel protein in human erythrocytes [5]. CHIP28, which was known to belong to a large family of integral membrane proteins with unknown functions, was expressed in *Xenopus laevis* oocytes by injection of in vitro transcribed RNA. When the oocytes were incubated in hypoosmotic solution, their volume increased due to water uptake. Cells in which no CHIP28 was expressed showed no relevant changes in cell volume. These experiments proved that the flow of water across the membrane was due to the presence of CHIP28 [5]. It was a real breakthrough for many scientific fields - membrane biology, physiology and medicine, as it turned out soon that aquaporins are involved in many common diseases, including nephrogenic diabetes insipidus (AQP2) and congenital cataract (AQP0). The Nobel Prize in Chemistry awarded to Peter Agre in 2003 documents the importance of these findings.

Since the discovery of AQP1 many members of the aquaporin family were described not only in mammalian cells, but also in cells of all other kingdoms of life - animals, fungi, bacteria, plants. Aquaporin family members are defined by some shared characteristics at the level of their secondary, ternary and quaternary structure. In biological membranes they exist as tetramers with each monomer operating as a separate water channel. Aquaporins are not active transporters but channels facilitating the water flow driven by an osmotic gradient. The monomer is composed of a conserved arrangement of six transmembrane helices, both the N- and C-terminus facing the cytosol. Two highly conserved asparagine-proline-alanine (NPA) motives are found on loops B and E, which fold back into the membrane forming the aqueous pore (hourglass model, [6]). This specific arrangement around a pseudo-twofold axis reflects an internal gene duplication [7]. The inhibition of water transport activity by mercurials, which has been one of the first hints on the proteinaceous nature of water transport, could be explained by indentification of Cys189 as the Hg^{++} inhibitory site [8].

The predicted hourglass model was confirmed by the first aquaporin structure that was determined in 1997 [9, 10], describing the characteristic fold of six transmembrane helices plus a seventh helix consisting of two half-helices formed by loops B and E. Further refinements of the structure allowed a more and more precise description of the mechanism of water permeation through the channel [11, 12, 13]. Two main topics were of special interest: (i) The high water transport rate of about 10^9 water molecules per second and (ii) the high selectivity for water, particularly in the context of proton exclusion.

In bulk water, protons are conducted by the Grotthus effect, a transfer via hydrogen bonds and transient hydronium ions. A file of water molecules through a virtual channel acts like a proton wire, thus the mechanism of proton exclusion in aquaporins despite the high water permeability remained a mystery until the first atomic structure solved by electron crystallography allowed initial speculations concerning interruptions of hydrogen bonds [12]. Because of the fast dynamics of water permeation inside the aquaporin channel, no direct experimental data could be obtained. To overcome this limitation, molecular dynamics (MD) simulations were performed, making it possible to observe transport of water molecules through the channel [14]. It became clear that two regions are critical: the NPA region in the center of the pore and the ar/R (aromatic/Arginine) region in the extracellular part of the channel. While throughout the channel, energetics are dominated by water-water interactions, in these two regions protein-water interactions are prominent. Additionally, a strong orientation of the water dipole was observed with a rotation by 180° at the NPA region. A second generation of MD simulations was combined with simulations of the quantum mechanical proton hopping to study the proton transfer reactions. This study showed efficient Grotthus transfer but also fast expulsion of protons from within the channel. It seems that the barrier resulting from electrostatic interactions rather than a proton wire interruption is the reason for proton exclusion in the aquaporin water channel [15, 16].

Over the past decade, several aquaporin structures have been solved by electron or X-ray crystallography. Beside the above described AQP1, structural data is available for the bacterial

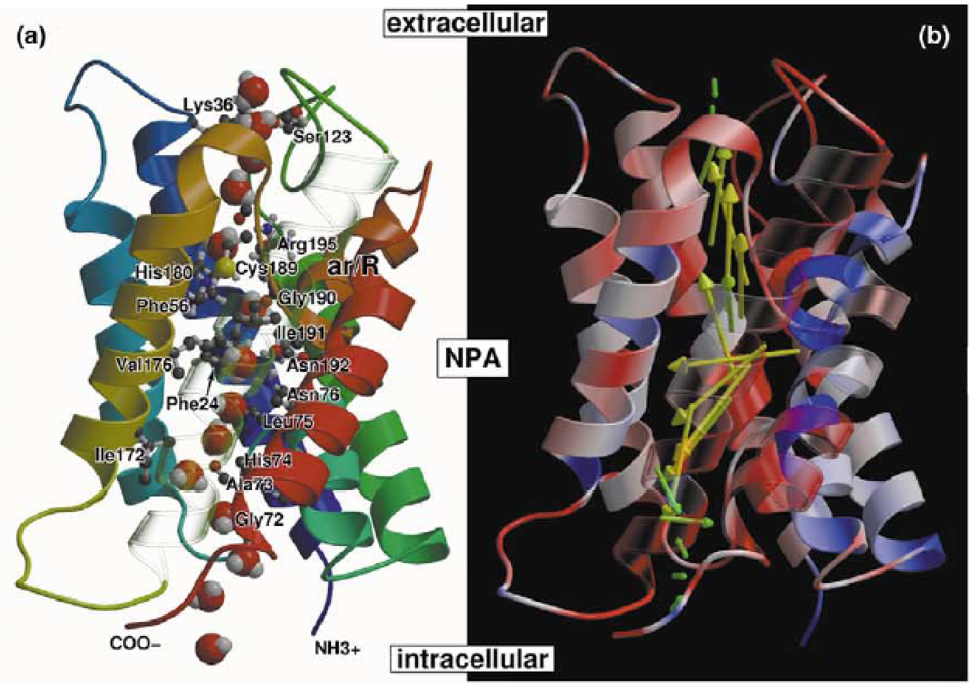

Figure 1.1: Water permeation through AQP1. (a) The pathway of water molecules through the AQP1 channel. (b) The orientation of water dipoles within the pore. A reorientation of the dipoles due to the electrostatics in the channel occurs in the NPA region. The electrostatic field (color coded on the protein backbone) poses the barrier for H^+ transfer, not the interruption of hydrogen bonds which is rather a secondary effect of the electrostatics. Figure directly taken from [16].

glycerol facilitator GlpF [17, 18], bacterial AqpZ [19], human AQP2 [20], human AQP4 [21]. Outstanding electron crystallographic work was done on AQP0 from eye lens fiber cells, where not only the structural basis of membrane junctions was solved [22], but also lipid-protein interactions could be visualized at 1.9 Å resolution [23].

The work presented in this thesis deals with two members of the aquaporin family, the plant aquaporin SoPIP2;1 and the human AQP8. Instead of covering the whole palette of aquaporins in all kind of species; fungi, bacteria, animals and plants, the following sections of this introduction are focused on aquaporin variety in mammals and on the role of aquaporins in plants.

1.2.1 Human aquaporins

Water constitutes about two third of the human body. To date, thirteen aquaporins were identified in mammals, unique in their tissue localization, transport properties and regulation. They are referred to as AQP0 - AQP12 and can be classed into two subsets: The classical aquaporins transporting water and the aquaglyceroporins that are permeated by water plus glycerol. The first group includes AQP0, AQP1, AQP2, AQP4, AQP5, AQP6 and AQP8. AQP1, which was the first member to be identified as a water channel, is found in the plasma membrane of many tissues as for example red blood cells and kidney. The kidney is a key organ in the maintenance of body water and salt balance and therefore contains several members of the aquaporin family. About 90 % of the 180 liters of water that is filtered by the kidney per day is readsorbed via AQP1. The remaining water readsorbtion is controlled by vasopressin-regulated AQP2 in the collecting duct [24]. Mutations in the AQP2 encoding gene result in severe nephrogenic diabetes insipidus. AQP0 is expressed in eye lens fiber cells where it is present in membrane junctions, having thus a dual role as water channel and adhesion protein [22]. Also AQP4, which is found in brain, has been shown to function both as water channel and cell adhesion protein [21]. In contrast to the other members, AQP8 and AQP6 are localized intracellularly rather than at the plasma membrane [25, 26]. Moreover, AQP6 was found to function as an ion channel [26], while AQP8 has been associated with ammonia transport [27].

The class of aquaglyceroporins transport glycerol additionally to water. AQP3 is found in many epithelial cells [28], e. g. in basolateral membranes of kidney collecting duct cells, sweat glands and airway epithelia. AQP7 is expressed in fat tissue, where it is responsible for glycerol release during fastening and starvation and has been proposed as a central agent in fat metabolism [29], while AQP9 in liver permits glycerol uptake for gluconeogenesis [30]. AQP10 exists as two isoforms, derived from two different transcripts, one being highly permeable to water, urea and glycerol, the other showing only poor water permeability and no permeability of other solutes [31, 32].

AQP11 and AQP12 comprise an unclassified subfamily which cannot be assigned to neither pure aquaporins nor glyceroporins. AQP11, which was found to be expressed in multiple rat tissues including kidney, liver, testes and brain, does not transport neither water, nor urea, glycerol or ions [33]. So far, no function could be assigned to AQP12 neither, which is localized at intracellular sites in acinar cell of the pancreas [34].

Most of the mammalian aquaporins are not exclusively expressed in one cell type but are found at different expression levels in different tissues, on the other hand several aquaporins have specific localizations in specialized tissue cells.

1.2.2 Plant aquaporins

Plants are often exposed to a rapidly changing environment but they are unable to evade from unfavorable conditions such as temperature, light, nutrients or water. To cope with drought stress or flooding, a fine tuned adaptation of water balance is of vital importance. This physiological relevance might explain the large number of aquaporin genes in plant genomes: 35 different aquaporin genes were found in *Arabidopsis* [35] and 33 in maize [36]. Aquaporins in plants can be divided into four subfamilies, the tonoplast intrinsic proteins (TIPs), nodulin

26-like intrinsic proteins (NIPs), small basic intrinsic proteins (SIPs) and plasma membrane intrinsic proteins (PIPs).

The plant vacuole, which is a cellular storage compartment with functions in turgor regulation, cell signaling and degradation, shows high water flux rates across its membrane. These high permeabilities, not only for water but also for urea and glycerol, were demonstrated to be due to the presence of TIP aquaporins [37]. TIPs have also been suggested to transport NH_3 [38]. Phosphorylation at a N-terminal serine residue was shown to regulate the water permeability of seed-specific α-TIP [39, 40].

Homologues of the soybean nodulin 26 protein form the NIP subfamily, expressed during the formation of symbiotic nitrogen fixing root nodules [41]. They are multifunctional channels involved in bidirectional flux of water, glycerol, NH_3 and other small solutes between the plant cytoplasm and symbiotic bacteroids. Two NIP subgroups are distinguishable, one having a Ca^{++} dependent protein kinase (CDPK) phosphorylation site at the C-terminus and a protein binding epitope [42]. Interacting proteins were identified, indicating a possible regulation by protein-protein interactions. The other NIP subgroup consists of glyceroporins and shares phosphorylation sites for MAP kinases.

SIP subfamily members are highly basic proteins with very short N-termini [43]. Their subcellular localization in the endoplasmatic reticulum was shown by GFP fusion experiments [44]. This smallest cluster within the plant aquaporin family remains to be characterized in more detail.

The plasma membrane intrinsic proteins represent the largest subfamily of plant aquaporins, consisting of 13 members in *Arabidopsis* and maize. They are divided into two subgroups named PIP1 and PIP2. The PIP2 aquaporins have a higher water channel activity than PIP1 members. Also, the former have a shorter N-terminus, a longer C-terminus and an additional stretch of eight amino acids in the first extracellular loop [45].

Although heterologously expressed PIP1 aquaporins display a low water permeability in various functional assays, experiments in planta do indicate an important role for PIP1s in water transport, suggesting that their water channel function needs to be activated in a still unknown way. On the other hand, permeability of PIP1 aquaporins for glycerol, urea, CO_2 or NH_3 was also observed and thus the PIP1 subgroup members could act as channels for these small solutes [46, 45].

PIP2 aquaporins induce an up to 20-fold higher water permeability than PIP1s [47]. Members of the PIP2 subgroup were identified in many species and are assumed to have roles in many different physiological processes. Regulation by phosphorylation was proposed for the spinach leaf aquaporin SoPIP2;1 [48, 49], and by changes in pH for the *Arabidopsis* AtPIP2;1

homologue [50]. A more detailed discussion of PIP2 regulation in the context of aquaporin gating in general is given in 2.1.2.

1.2.3 Aquaporins are multifunctional proteins

Conclusively, aquaporins are despite their highly conserved structural features more than just water channels. On one hand, they show varying substrate specificity for small solutes like glycerol, urea, NH_3 or CO_2, but on the other hand they also play roles in cell adhesion. Some have a constitutively high water channel activity, some need to be activated by very different regulation mechanisms, some have very poor intrinsic water channel activity. All these properties make aquaporins an exciting and very broad field of research, with a wealth of experimental information already available but also with many still unsolved riddles.

Chapter 2

Structure, Function and Regulation of the Plant Aquaporin SoPIP2;1

Abstract

SoPIP2;1 is one of the major integral proteins in spinach leaf plasma membranes. In the Xenopus oocyte expression system its water channel activity is regulated by phosphorylation at the C-terminus and in the first cytosolic loop. To assess its structure, SoPIP2;1 was heterologously expressed in *Pichia pastoris* as a His-tagged protein and in the non-tagged form. Both forms were reconstituted into two-dimensional crystals in the presence of lipids and analyzed by cryo-electron microscopy. Crystalline sheets were highly ordered and diffracted electrons to a resolution of 2.96 Å. High resolution projection maps of tilted specimens provided a three-dimensional structure at 5 Å resolution. The phosphorylation-related functional state, however, could not be determined at the given resolution. Therefore, electron diffraction patterns are being processed to solve the structure at atomic resolution using molecular replacement. In addition, mass spectroscopy (MS) was used to determine the phosphorylation state of the crystallized SoPIP2;1. To gain insight into the putative regulating mechanism of site-specific phosphorylation, in vitro phosphorylation and dephosphorylation attempts were made, but were not successful. As an alternative, the C-terminal and B-loop phosphorylation sites (Ser115 and Ser274) were mutated into both aspartates and alanines to imitate the phosphorylated and dephosphorylated state, respectively. The mutant forms of SoPIP2;1 were purified, reconstituted into 2D crystals and functionally characterized.

2.1 Introduction

2.1.1 SoPIP2;1 - Structure determination of a plant aquaporin

SoPIP2;1, previously called PM28A, is a PIP2 isoform in *Spinacia oleracea* (spinach) leaf plasma membranes, where aquaporins constitute 20% of all integral membrane proteins [48]. Two serine residues were found to be phosphorylated in vivo as a response to an increase of the apoplastic water potential. Phosphorylation of these serines located in the C-terminal region (Ser274) and in cytosolic loop B (Ser115) was suggested to regulate the water channel activity of SoPIP2;1 [49]. A hypothetical model was presented in which the extracellular water potential is perceived by an osmosensor that translates the signal into an increased intracellular Ca^{++} concentration, which in turn activates a Ca^{++}-dependent protein kinase (CDPK), leading to phosphorylation of the water channel and thus to increased water channel activity [49]. In times of drought, hence at low apoplastic water potential, the plasma membrane aquaporins are dephosphorylated and water channel activity is low, while aquaporins of the vacuole membrane are open to compensate for water loss of the cytosol to the apoplast [51]. The consensus phosphorylation site at Ser274 in the C-terminal region is conserved in all PIP2 isoforms, independent of species, but not in the PIP1 isoforms which have a shorter C-terminal region. In loop B, the consensus phosphorylation site Ser115 is conserved in all PIPs, i.e. in PIP1 as well as PIP2 isoforms [35].

Several aquaporin structures were solved in the past few years, human AQP1 [12, 52], AQP0 from sheep eye lenses [22, 53] as well as two bacterial members: GlpF [17] and AqpZ [19]. Together with molecular dynamics simulations [14, 54, 15, 55, 56], these structures gave insight into function and selectivity of water channels. However no structural data on direct gating upon phosphorylation of an aquaporin was available at the time the project on structure determination of SoPIP2;1 was started. Also, no 3D structure of plant aquaporins had been solved.

Both C-terminally His-tagged and untagged SoPIP2;1 have been heterologously overexpressed in the methylotrophic yeast *Pichia pastoris* to high levels of approximately 25 mg protein per liter of culture and shown to be functionally active when reconstituted into proteoliposomes [57]. Both forms were purified and reconstituted into 2D crystals in the presence of lipids. The density map presented here was the first 3D plant aquaporin structure (Appendix A). Furthermore, the present study reports to our knowledge the first structure of a heterologously expressed aquaporin in any eukaryotic species.

2.1.2 Investigations on the mechanism of regulation of SoPIP2;1

Regulation of aquaporins in all kind of species is known to occur at different stages and makes use of various mechanisms: Mammalian AQP0 from eye lens fibre cells is found in two forms, of which one is closed, forming highly ordered stacks of thin lens junctions, while the other, non-junctional form has an open water channel. Junctional, closed AQP0 is formed upon proteolytic cleavage of the cytoplasmic termini [58]. Additionally, changes in pH and Ca^{++} concentration were proposed to regulate AQP0 activity [59]. Human AQP2, which is located in renal collecting duct cells and is involved in urine concentration, is stored in intracellular vesicles. Upon binding of vasopressin to the V2-receptor on the basolateral membrane of the cell, AQP2 gets phosphorylated by the cAMP-dependent protein kinase A (PKA) and redistributed to the apical plasma membrane [24]. For plant PIP2;1 aquaporins, two models of regulation were proposed: The first one by [49] for SoPIP2;1 in spinach leaf plasma membranes, involving phosphorylation at two serines as described above. Another regulative mechanism was suggested for *Arabidopsis* PIP2;1 [50]. In this case, oxygen deprivation (anoxia) leads to an inhibition of water permeability in roots, which is mediated by a drop of cytosolic pH. In mutagenesis studies a histidine (H197) in the cytosolic D-loop of AtPIP2;1 was identified as the residue sensing pH dependency. In contrast to mammalian aquaporins which are regulated by external pH [60, 26, 59], AtPIP2;1 is regulated only by cytosolic pH.

Although the main interest in studying the structure of the plant aquaporin SoPIP2;1 lies in its specific regulation mechanism, our 3D map at the resolution of 5 Å (appendix A) gives no clues concerning this subject. However, few months after publication of our 5 Å map, an X-ray structure of SoPIP2;1 was published presenting both a closed conformation at a resolution of 2.1 Å and an open conformation at 3.9 Å [61]. The closed conformation was obtained from untagged SoPIP2;1, while the open conformation is from His-tagged SoPIP2;1. According to this paper, channel closure can be achieved either by dephosphorylation of S115 and S274 (occuring during drought stress) or by protonation of H193 following a drop in cytosolic pH. In the closed form, loop D forms hydrogen bonds with the N-terminus and is thus anchored under the channel pore, which is therefore blocked. Phosphorylation of S115 in loop B disrupts this anchor and loop D is released. The second discussed serine S274 located in the C-terminal region interacts with the adjacent monomer at the cytosolic end of helix 5/loop D. When S274 is phosphorylated, this interaction gets lost and also leads to a displacement of loop D. In case of flooding (anoxia), a fast closure of the channel is obtained by recovery of the anchoring of loop D to the N-terminus by a salt bridge formed by protonated H193.

SoPIP2;1 that crystallized in the open form is not phosphorylated, therefore, implications of phosphorylation on the opening/closure mechanism of SoPIP2;1 were gained by molecular dynamics (MD) simulations. The density of loop D in the structure of the open conformation could only be identified in one monomer within the tetramer, while in the crystal structure of the closed form, it is involved in crystal contacts and therefore present in all four monomers. These suggestions regarding the mechanism of opening and closure of the channel elegantly combine phosphorylation and pH regulation of PIP2;1 aquaporins, yet some questions remain unanswered. E. g., why is the open channel conformation not phosphorylated, which, according to the functional model, is a prerequisite? Do the in silico predicted conformational and activity changes take place if the phosphorylation state of crystallized SoPIP2;1 is changed? What phosphorylation state is present in our 2D crystals? Is the channel presented in our 3D map in its open or closed conformation?

Another aspect that has to be considered is the proposed inhibition by Ca^{++} ions [62], which might be replaced by Mg^{++} in our 2D crystals, since reconstitution into 2D crystals occurs in the presence of 50 mM $MgCl_2$ (Christophe Maurel, pers. com.) In the X-ray structure, a Cd^{++} is found to additionally anchor loop D and thereby stabilize the closed conformation. The Cd^{++} is proposed to be replaced by Ca^{++} in vivo. However, despite the presence of 50 mM $MgCl_2$, loop D in our electron crystallographic 3D map is not lying below the channel pore but rather on the side of the monomer (Fig. 2.5), contradicting the assumption that Ca^{++} or Mg^{++} ions anchor loop D below the channel pore. Additionally, inhibition of water channel activity by Ca^{++} ions interferes with the model proposed by [49] where increased cytosolic Ca^{++} concentration causes phosphorylation by a CDPK and thus activation of the water channel.

Approaching clarification of unanswered questions of the complex gating mechanism of SoPIP2;1 required trial of different experimental approaches. In a first step, 2D crystals of SoPIP2;1 were attempted to be phosphorylated and dephosphorylated. To test efficiency of phosphorylation, radioactively labeled γ-^{32}P-ATP was used. No complete phosphorylation or dephosphorylation could be detected in this way. Investigation of the phosphorylation state of crystallized SoPIP2;1 was therefore continued using mass spectroscopy of proteolytically cleaved SoPIP2;1, which demonstrated the C-terminal putative phosphorylation site to be unphosphorylated. To further investigate the effects of phosphorylation and dephosphorylation, both potentially phosphorylated serines were mutated into both alanine and aspartate, overexpressed in *Pichia pastoris*, purified and analyzed biochemically and by electron crystallography. These experiments are thought to shed some light into the complex regulating mechanisms that might complement each other in a way, but might also act independently.

Table 2.1: Conditions screened for 2D crystallization of His-tagged and untagged SoPIP2;1

	Parameter	Screened	Optimum
HT	Lipids	*E. coli*, brain, liver, soy & heart polar lipids, DOPS, DOPC, POPG	*E. coli* polar lipids
	LPR	0.1 - 1	0.1
	pH	5, 6, 7, 8, 8.5, 9, 9.5	9
	NaCl	0, 5, 100, 250, 500, 750 mM	500 mM
	$MgCl_2$	0, 2, 5, 50 mM	0 mM
	Additives	500 mM urea	–
	Detergent	OTG, OG, DDM/OG mix	OG
	Method	Buttons, machine	Machine
untagged	Lipids	*E. coli* polar lipids, DOPC, DMPC	*E. coli* polar lipids
	LPR	0.1 - 1	0.3 - 0.4
	pH	6, 7, 8, 9, 10	8
	NaCl	100, 500 mM	100 mM
	$MgCl_2$	0, 5, 50, 100 mM	50 mM
	Method	Buttons, machine	Machine

2.2 Results: Wild Type SoPIP2;1

2.2.1 Purification and 2D crystallization of wild type SoPIP2;1

Pichia pastoris membranes containing heterologously expressed SoPIP2;1 were prewashed using the alkaline/urea stripping to remove membrane-associated peripheral proteins. His-tagged SoPIP2;1 was purified according to [57], while the purification protocol for untagged protein was established by adaptation of the procedure used for purification of native SoPIP2;1 from spinach leaf plasma membranes [63]. Very high yields as reported by [57] were obtained for both His-tagged and untagged SoPIP2;1. Protein concentration of eluted His-tagged SoPIP2;1 was typically 1.5 - 2 mg/ml, in the case of untagged SoPIP2;1, concentrations of 5 - 8 mg/ml could be routinely obtained, giving the possibility of setting up crystallization trials at protein concentrations above 2 mg/ml. Although His-tagged SoPIP2;1 crystallized readily, crystal form and symmetry were depending very much on the given conditions (results not shown, see [64]). Best-ordered crystals of His-tagged SoPIP2;1 were of tubular shape with alternating rows of up and down oriented tetramers which were however not suitable for structure determination due to anisotropic ordering. When studying 2D crystallization conditions for aquaporins, it is remarkable that 5 - 50 mM $MgCl_2$ are used in almost all cases (see table 3.3). It has been suggested that divalent ions such as Mg^{++} have a significant influence on 2D crystallization because they affect surface charges of the lipid bilayer [65]. The use of $MgCl_2$ is however limited by the fact that His-tagged proteins have a tendency to aggregate in the presence of divalent ions. Therefore most His-tagged aquaporins were crystallized in the presence of only

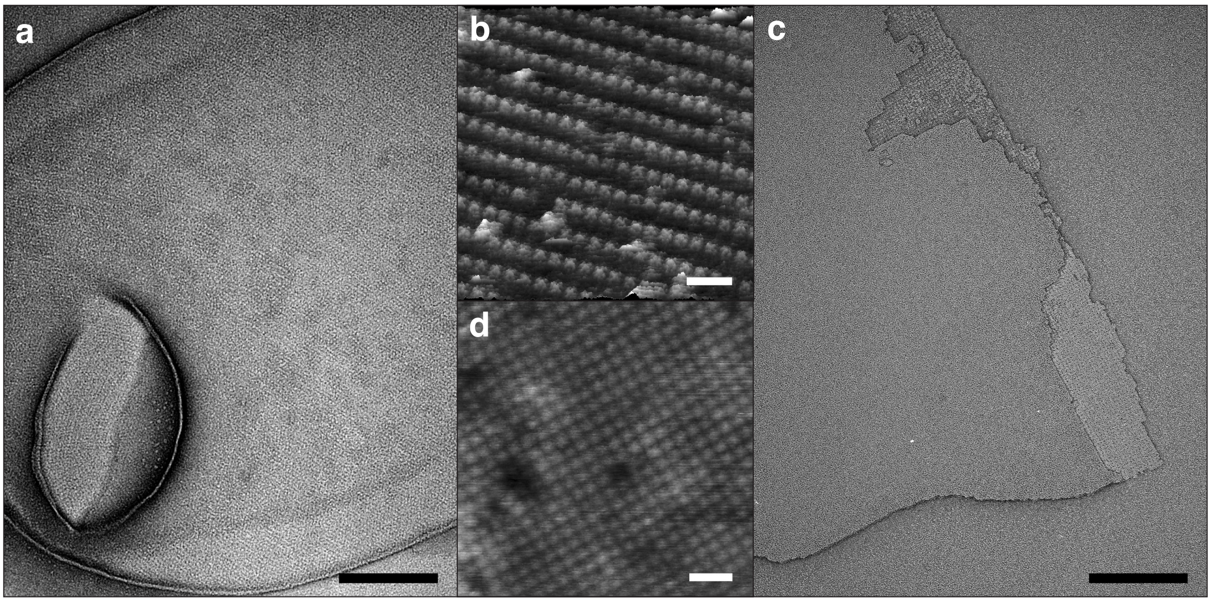

Figure 2.1: Two crystal forms of SoPIP2;1. (a) Vesicular crystals consisting of rows with SoPIP2;1 tetramers oriented inside out and right side out. (b) AFM height image of a crystal of the same type as depicted in a, revealing the alternating orientation of the tetramers. (c) Double-layered crystalline sheets of equally oriented SoPIP2;1 tetramers. Sheets are stacked face-to-face with the extracellular side, which exhibits a higher contrast after negative staining compared to the cytoplasmic side, as seen at ruptures of the top layer. (d) AFM height image of a crystal sheet as shown in b, demonstrating the equal orientation of SoPIP2;1 tetramers. Scale bars are 200 nm in (a) and (c), 20 nm in (b) and (d). Grey levels in the AFM images correspond to height differences 0-3 nm in (b) and 0-4 nm in (d). AFM pictures were taken by Thomas C. Kaufmann and Patrick Frederix.

5 mM $MgCl_2$. It turned out that in the case of His-tagged SoPIP2;1, already 5 mM $MgCl_2$ lead to aggregation and the formation of small vesicles. The expectation that the use of 50 mM $MgCl_2$ for crystallization of untagged SoPIP2;1 would not pose aggregation problems turned out to be true. Moreover, it became clear that the high concentration of $MgCl_2$ was even decisive in obtaining highly ordered crystalline sheets of SoPIP2;1 (Fig. 2.1c). Under crystallization conditions without $MgCl_2$, tubular crystals of the same kind as observed for His-tagged SoPIP2;1 were obtained (Fig. 2.1a).

Another difference between 2D crystallization of His-tagged SoPIP2;1 and the untagged version concerns the pH optimum which is more basic for the His-tagged protein (pH 9 - 9.5) than for the untagged (pH 7 - 8).

Highly ordered crystals of untagged SoPIP2;1 were grown in the presence of 50 mM $MgCl_2$, 20 mM Tris-HCl; pH 8, 100 mM NaCl, 2 mM DTT, 0.01% NaN_3. These crystals are double-layered crystalline sheets of several μm in size. SoPIP2;1 tetramers are equally oriented and ordered in a tetragonal lattice. The two crystalline layers adhere to each other with their extracellular faces as indicated by the higher contrast of the inner surface of the double layer seen at ruptures (Fig. 2.1c) [66].

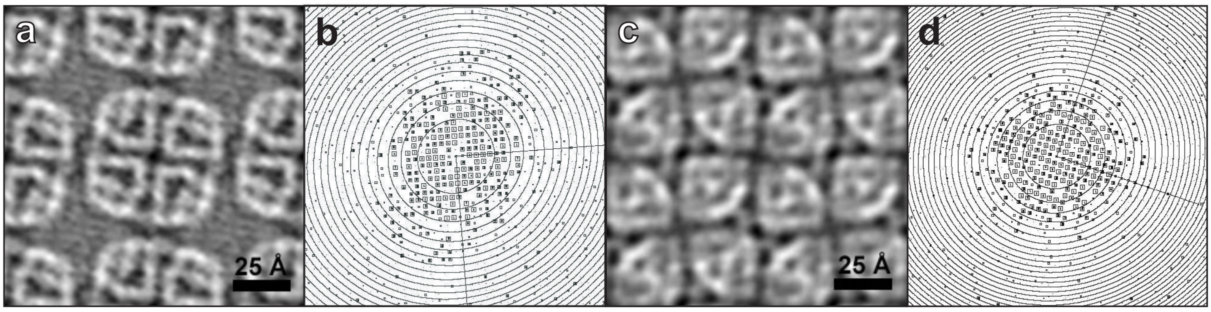

Figure 2.2: Projection maps and corresponding IQ-plots of single-layered (a, b) and double-layered (c, d) crystals. In IQ-plots, reflections are weighted corresponding to their signal-to-noise ratio. Best spots are displayed as largest squares with IQ number=1, weakest ones are small squares and IQ=9. The border of the IQ plot corresponds to a resolution of 3 Å.

2.2.2 Structural analysis: The 5 Å structure determined by electron crystallography

When crystalline sheets of untagged SoPIP2:1 were imaged in cryo EM, slight differences in contrast between individual crystals within one sample, indicating different numbers of membrane layers, could be observed. Electron micrograph taken from such sheets were processed using the automated proceeding described in the materials and methods section. When displaying the calculated projection maps of processed images, it became clear that about 10-20% of the crystals were single-layered while the remaining were double-layered (as shown in Fig. 2.1). A doubtless distinction between the two crystal types could not be made before the output of the processing, the projection map, was viewed. Neither the differences in contrast were strong enough, nor any clear differences in the power spectrum were found to selectively take images of double- or single-layered crystals. From inspection of processed data it could be estimated that double-layered crystals were slightly better ordered. Examples of projection maps of both single- and double-layered crystals as well as the corresponding IQ-plots are given in Fig. 2.2. Single layers clearly show one aquaporin tetramer per unit cell, all tetramers being equally oriented. A projection of the double-layered crystal on the other hand does not allow easy identification of the tetramer. The overlay of two crystalline layers that are shifted against each other by half a unit cell gives a more complex pattern. Fig. 2.3 explains how two crystalline single layers are combined resulting in the projection of a double layer. In the subsequent merging of data to obtain a 3D data set, only images of double-layered crystals were selected, for two main reasons: First, about 80 % of processed images were from double-layered crystals and second, double-layers seemed to be of better quality than single-layers. A density map at 5 Å resolution could be derived from processed micrographs of tilted and untilted double-layered crystalline sheets of SoPIP2;1. First, only untilted images were merged. Higher tilt angle images were successively added to the merge, cycling through

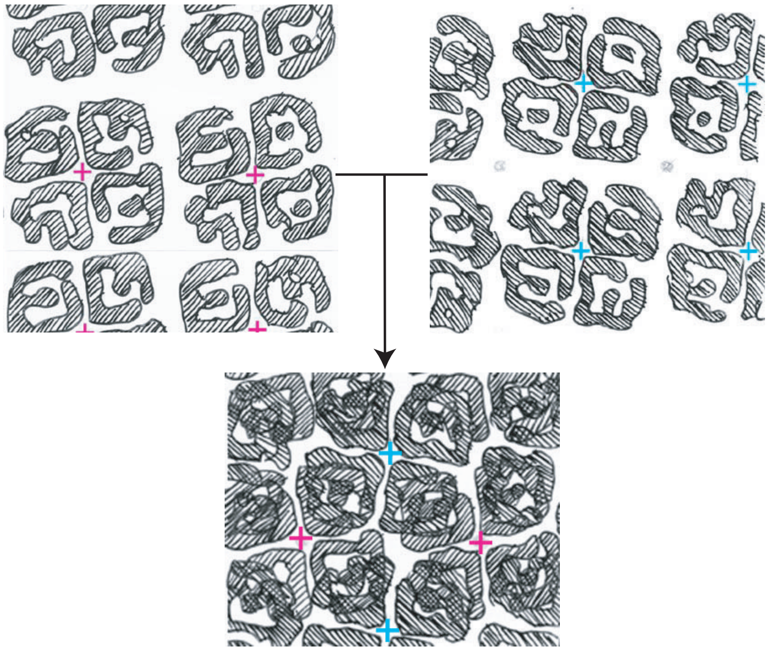

Figure 2.3: Symmetry of the double-layered crystals illustrated by overlaying two single layer projections. One layer is shifted by half a tetramer in x and y direction respective to the other and mirrored. The latter reflects the fact that the two layers are not equally oriented but stacked on each other with their extracellular faces.

several rounds of phase origin refinement and careful inspection of the 3D data set, e. g. the calculated map and the fitting of lattice lines, by eye. An example of a lattice line fit is shown Fig. 2.4. Eventually, 156 images were merged applying a p4 symmetry to obtain a 3D data set. Phase residuals below 50° at a resolution of 5 Å allowed merging of data up to 5 Å in the membrane plane. Perpendicular to the membrane, the resolution limit applied was 7.14 Å. Crystallographic data and a detailed description of the structure are given in appendix A. The crystallographic unit cell comprises two lipid bilayer planes containing one SoPIP2;1 tetramer in one plane and four monomers in the other. Each monomer consists of seven rod-like structures that can, by comparison to AQP1 [14], be assigned to α-helices 1 to 6 and loops B and E that fold back into the membrane forming to half-helices that meet in the middle of the channel. SoPIP2;1 monomers face each other with their extracellular side. As a particularity that distinguishes the SoPIP2;1 structure from other aquaporin structures, helix 1 appears to be longer and straighter than in AQP1. Together with helix 2, it protrudes farther out of the membrane plane and points towards the fourfold axis, filling the gap between neighbouring tetramers of the opposing layer.

2.2.3 Electron diffraction on SoPIP2;1 crystals

The electron dose at which diffraction patterns were taken was measured as follows. The Philips CM200 FEG was aligned according to the usual protocol for electron diffraction. With-

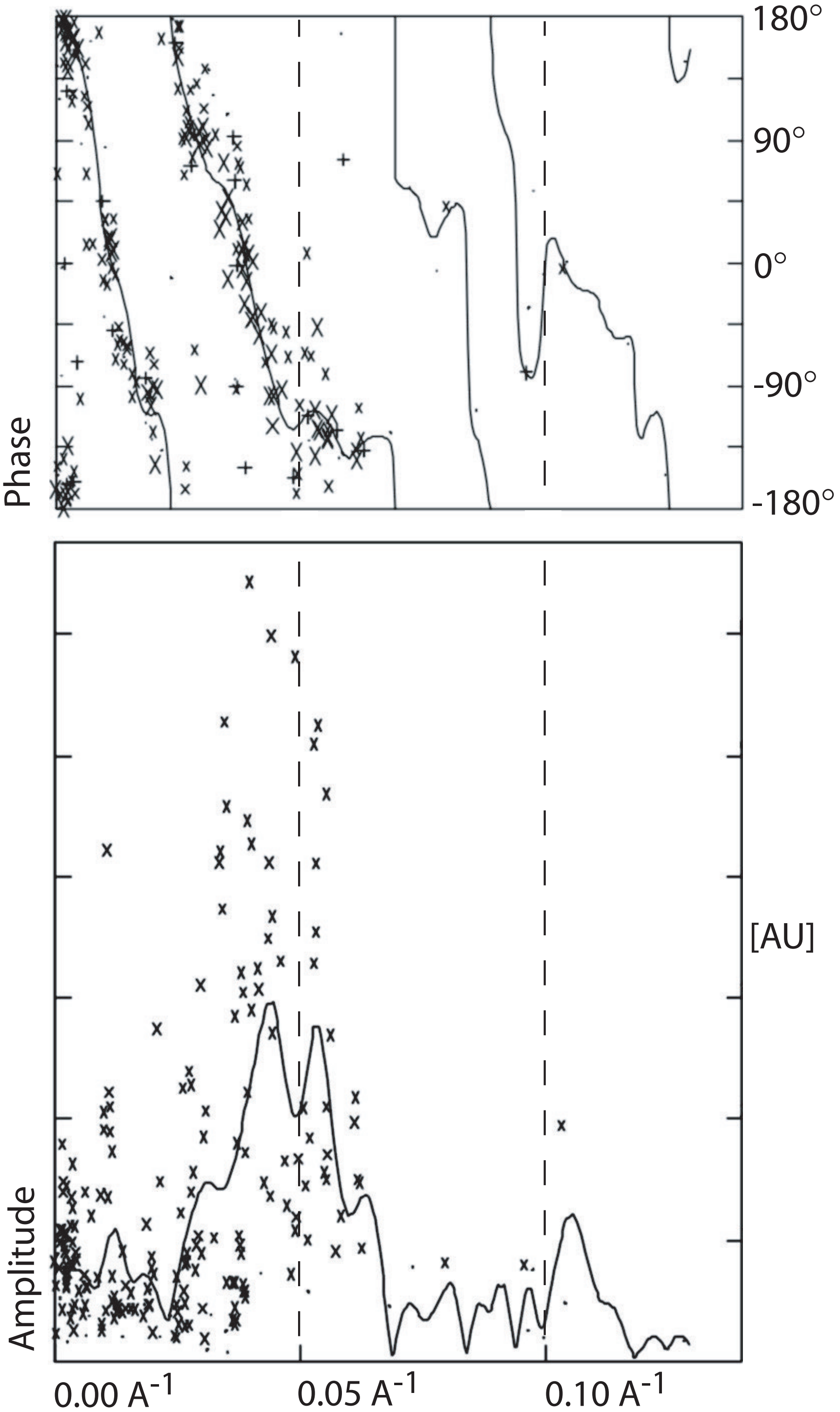

Figure 2.4: An example for lattice line fitting. Phases and amplitudes of reflections on lattice line (6,4) are plotted against z∗ and the lattice line is fitted to the data set. Data points from single reflections are displayed by crosses which size represents the weighing of the data point.

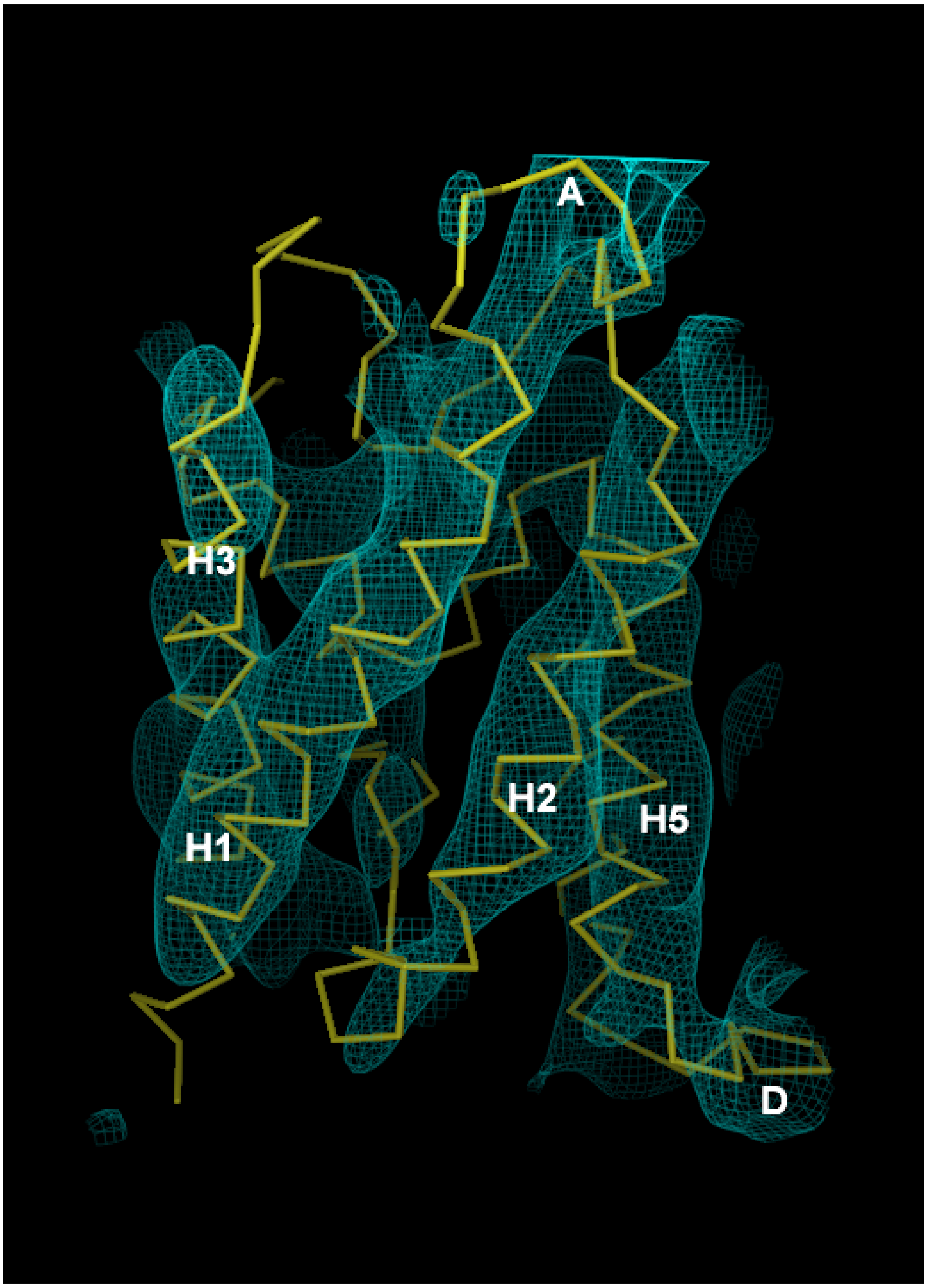

Figure 2.5: The SoPIP2;1 potential map (cyan) superimposed with the C_α-backbone of the atomic model of AQP1 (yellow). Beside helices 1, 2, 3 and 5, this view shows the specific arrangement of loop A. Note that also loop D is remarkably well resolved, not capping the channel as in the X-ray structure proposed by [61] but rather on the side as in AQP1.

out changing settings of lenses, spotsize or apertures, the mode was changed to imaging and Kodak SO 163 film was exposed for 10 sec. In this way, the illuminated area and exposure time correspond to the dose on the selected area in diffraction mode. Negatives were developed according to the common protocol provided by Kodak. The sensitivity S=0.305 of Kodak SO 163 film was calculated from table 2 in [67]: An optical density OD=0.36 corresponds to 0.11 electrons/μm^2 at the emulsion, and S is defined as the number of electrons resulting in OD=1. The OD of negatives taken at magnifications of 50'000 x were measured to be 0.21 - 0.22 on crystals and 0.19 on C-film. The resulting electron doses are therefore calculated to be below 2 electrons/Å^2 which seems to be very low. Thereby it has to be considered that the film developing time used by [67] was 12 min, while here negatives were developed for only 9 min. These results still allow the conclusion that the dose used for electron diffraction is sufficiently low to minimize radiation damage.

A set of electron diffraction patterns was taken covering tilt angles between 0° and 60°. Examples are given in Fig. 1 of Appendix A, demonstrating the quality of SoPIP2;1 crystals. At 0° tilt and at 60°, reflections corresponding to a resolution of 2.96 Å and 4 Å, respectively, can be observed. The data set that was recorded so far contains 66 diffraction patterns at 0 ° tilt, 9 at 10° tilt, 20 at 30° tilt, 57 at 45° tilt and 31 at 60° tilt. This data is not included in the 3D map presented in appendix A but is presently being processed using a new software named IPLT [68], aiming to build a high resolution model by means of molecular replacement techniques.

2.2.4 Phosphorylation and dephosphorylation of SoPIP2;1 2D crystals

All structural studies are performed with heterologously overexpressed SoPIP2;1 [57]. Whether this highly expressed aquaporin gets phosphorylated and activated by *Pichia pastoris* native kinases is unclear and therefore it is not known beforehand in which state the crystallized and purified protein is. However, activity measurements performed on proteoliposomes showed overexpressed SoPIP2;1 to have a significant water channel activity compared to control liposomes containing no protein [57]. The ultimate goal of the following series of experiments was to investigate by electron diffraction how phosphorylation and dephosphorylation influence the structure of SoPIP2;1. Therefore, 2D crystals of heterologously expressed SoPIP2;1 were subjected to phosphorylation reactions by protein kinase C (PKC) and dephosphorylation by alkaline phosphatase. The difficulty of performing such experiments lies not only in the search for optimal experimental conditions but also in an appropriate detection method to monitor the experimental result. In some cases, phosphorylation-induced mobility changes on SDS-PAGE

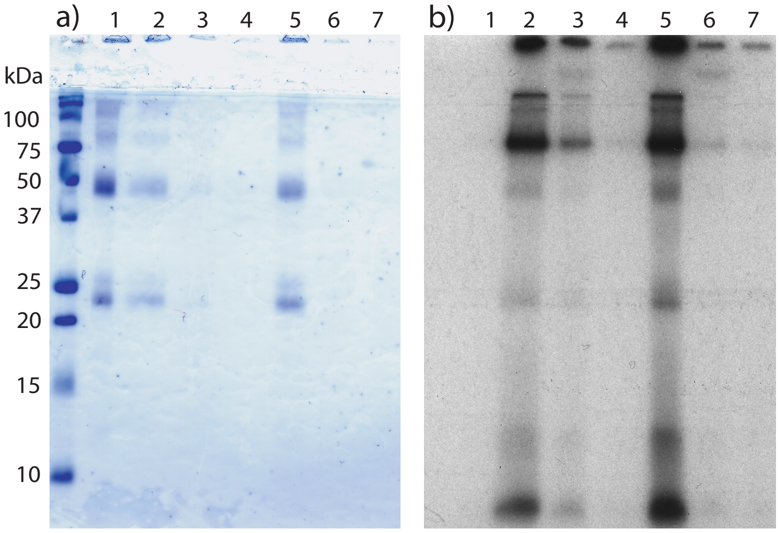

Figure 2.6: Phosphorylation by PKC: Coomassie Blue stained SDS-PAGE (a) and corresponding autoradiography (b). Lanes: 1) no reaction performed. 2) Phosphorylation reaction 1 with Phorbolester as activator. 3) First wash of reaction 1. 4) Second wash of reaction 1. 5) Phosphorylation reaction 2 with DAG as activator. 6) First wash of reaction 2. 7) Second wash of reaction 2.

were reported in the literature [69, 70, 71]. However, these mobility changes are rather due to large conformational changes [72] or extensive multiple phosphorylation [71] than changes in mass, as a phosphate moiety of 80 Da constitutes a mass change of $< 0.3\%$ in a protein of about 30 kDa. In most cases individual phosphorylation or dephosphorylation events cannot be expected to be detectable by SDS-PAGE. The use of γ-^{32}P-ATP, however, makes it possible to monitor the success of phosphorylation by autoradiography. Even quantification of the phosphorylation efficiency is possible by scientillation counting.
Both phosphorylation sites S115 and S274 lie in typical recognition sequences for vertebrate protein kinase C, which are Ser-X-Arg [73] and Arg-Lys-X-Ser-X-X-Arg [74] and were therefore shown to be possibly phosphorylated in vitro by PKC [48, 49, 57]. Initial attempts to dephosphorylate SoPIP2;1 using calf intestine alkaline phosphatase (CIAP) gave also promising results (S. Sjövall-Larsen, unpublished results and [57],). In a first attempt to radioactively label reconstituted SoPIP2;1 by phosphorylation, two reactions containing 2D crystals of SoPIP2;1, PKC, γ-^{32}P-ATP, Ca^{++}, Mg^{++} and either Phorbol 12,13-dibutyrate (Phorbolester) or 1,2-Dioctanoyl-sn-glycerol (DAG) as activators of PKC were performed. The reaction was saturated with cold ATP and stopped by washing the pelleted 2D crystals twice. A SDS-PAGE was run with reaction mixtures, supernatants from washing and a control sample were no reaction took place. The typical ladder pattern of SoPIIP2;1 looks familiar at first sight, it is however shifted towards lower molecular weight; the monomer band being at apparent 22 kDa instead of 30 kDa. The autoradiography of the gel illustrates the phosphorylation reaction in a qualitative

way (Fig. 2.6b). Both reactions yield radioactive signals on the electrophoretic bands reflecting SoPIP2;1 monomers, dimers and tetramers. Remarkably, the most prominent bands on the Coomassie Blue stained SDS-PAGE are the dimer and the monomer band (apparent molecular weight approx. 45 kDa and 22 kDa, respectively), while the strongest radioactive signal comes from a higher molecular weight band probably representing the SoPIP2;1 tetramer. Hence the tetrameric state, which is the most weakly populated one, is the one that is best phosphorylated. It is noteworthy that during the reaction, all reconstituted SoPIP2;1 is assumed to have been in a tetrameric state. The monomeric and dimeric states observed on SDS-PAGE are due to solubilization by SDS, which occured after the phosphorylation reaction. This observation therefore suggests that phosphorylation makes the tetramer more resistant to solubilization by SDS. Yet the shift in molecular weight of monomer and dimers indicates proteolytic cleavage, possibly of the C-terminus. This might also explain the additional radioactive band at the bottom of the gel, which might be the phosphorylated C-terminal peptide.

However, the relatively weak signal observed for monomer and dimer bands also indicates that the phosphorylation event was not complete. In fact, the 10 μCi γ-^{32}P-ATP that were used for phosphorylation correspond to 0.003 nmol ATP. When mixed with 1 nmol cold ATP and applied to 1 nmol of protein, most of the radioactive signal should be incorporated. Yet the radioactive signal estimated with the Geiger counter was much higher in the supernatant after washing the crystals than in the pellet, although the volume of the supernatant was approximately 7 times larger, meaning that much more γ-^{32}P-ATP was still in the supernatant than incorporated into the crystals. There are several possible reasons for the incompleteness of the reaction. First, the reaction time was too short. However, considering that 1 unit of PKC transfers 1 nmol of phosphate per minute at 22°C, pH 7, the 0.06 units of PKC used in our experiment would need 17 min to transfer 1 nmol. Hence a total incubation time of 30 min at 30°C should be enough. A second possible reason for the unefficient phosphorylation could be that SoPIP2;1 was already phosphorylated in the 2D crystal. To improve the phosphorylation efficiency, it would be therefore necessary to dephosphorylate beforehand. Dephosphorylation was performed under standard conditions, using an excess of alkaline phosphatase and varying the reaction time. No difference (e. g. in form of a mobility shift) between untreated and dephosphorylated samples could be detected by silver stained SDS-PAGE 2.7). However, one of the resulting presumably dephosphorylated samples was further used for phosphorylation (Fig. 2.8). The reaction was performed as described above, including untreated crystals, a reaction without PKC, two different activators (DAG and phorbolester), a reaction without activator and the previously dephosphorylated sample. The silver stained SDS-PAGE performed after the reaction displayed one striking feature: The previously dephosphorylated sample displayed

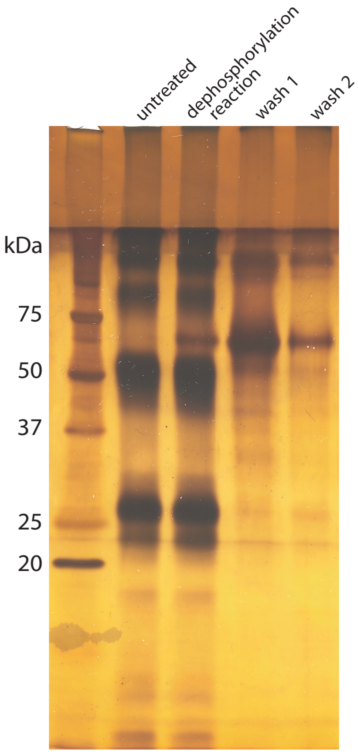

Figure 2.7: Silver stained SDS-PAGE of a dephosphorylation reaction in order to monitor a putative mobility shift. As control, crystals with no reaction performed were loaded.

a shift of the typical ladder pattern of SoPIP2;1 towards lower apparent molecular weights (Fig. 2.8, lane 10). Additionally, no radioactive signal appears in the corresponding lane of the autoradiography. One possibility would be that the sample still contained alkaline phosphatase, the dephosphorylation reaction went on for several days, and the observed mobility shift is due to dephosphorylation. The lack of a radioactive signal could be due to enduring, strong activity of alkaline phosphatase, which continuously removes incorporated phosphates. However, another reason for the apparent mass loss could be proteolytic activity in the sample. If PKC was able to phosphorylate only the C-terminal phosphorylation site, a cleavage of the C-terminus could also explain the absent radioactive signal. It should be noted that on many SDS-PAGEs of SoPIP2;1 the monomer band sometimes appears as a double band with varying intensity proportion. Whether this phenomenon is due to proteolytic cleavage, phosphorylation or another post-translational modification remains unclear. It could however not be unambiguously reproduced by dephosphorylation experiments under various conditions.

2.2.5 Defining the phosphorylation state of 2D crystallized SoPIP2;1 by mass spectroscopy

As depicted above, it is not clear if S115 and S274 of overexpressed SoPIP2;1 are phosphorylated in *Pichia pastoris* and if yes, to what extend. To determine the phosphorylation state

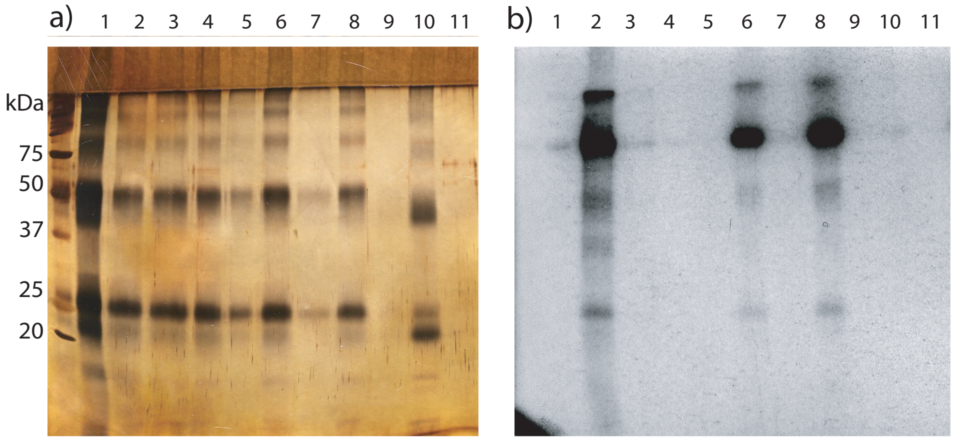

Figure 2.8: Silver stained SDS-PAGE (a) and corresponding autoradiography (b) Lanes: 1) no reaction performed. 2) Reaction I with DAG as activator. 3) Wash of reaction I. 4) Control reaction mix without PKC. 5) Wash of control mix. 6) Reaction II with phorbolester as activator. 7) Wash of reaction II. 8) Reaction III without activator. 9) Wash of reaction III. 10) Reaction IV using dephosphorylated sample from experiment 2.7, DAG as activator. 11) Wash of reaction IV.

of the two potential phosphorylation sites, several experiments consisting of various digestion reactions of reconstituted SoPIP2;1 followed by fragment separation by liquid chromatography and mass spectroscopy (LC-MS) were performed. Endoproteinase LysC digestion resulted in only few peaks that could be assigned. Nevertheless, the C-terminal fragment containing S274 could be assigned and defined as unphosphorylated. Only 2-3% are apparently present in the phosphorylated state, but it could be up to 10%, because the ionization efficiency of phosphorylated fragments is poorer compared to unphosphorylated peptides.

The peptide containing phosphorylation site S115 could not be identified, probably due to more hydrophobic cleavage sites that are buried within the lipid bilayer and hence not accessible to LysC. Therefore chemical digestion by CNBr under denaturing conditions (solubilization in 70% formic acid) was undertaken. The digest was applied to a C18 reverse phase column on a HPLC using varying organic B solvents like acetonitrile, n-propanol or formic acid to separate the hydrophobic peptides. Yet the fragment containing S115 could not be isolated. A similar, promising method for mass spectroscopy on membrane proteins has been proposed by [75]. This approach is used for unsolubilized membrane proteins, just like our case of reconstituted SoPIP2;1. High-pH treatment disrupts sealed membrane compartments, but the lipid bilayer is neither denatured nor solubilized. Subsequent digestion with robust, nonspecific protease Proteinase K cleaves the soluble domains of membrane proteins and allows identification of modifications such as phosphorylation or methylation by LC-MS. Application of Proteinase K on SoPIP2;1 according to [75] did however not allow identification of the B-loop fragment containing S115.

Table 2.2: LysC fragments of SoPIP2;1 digestion

Frag.	Residue	Mass	Mass+P_i	Sequence
1	1-3	365.2		MSK
2	4-16	1449.7		EVSEEAQAHQHGK
3	17-33	1919.9		DYVDPPPAPFFDLGELK
4	34-64	3537.9		LWSFWRAAIAEFIATLLFLYITVATVIGHSK
5	65-113	5012.6		ETVVCGSVGLLGIAWAFGGMIFVLVYCTAGISGGHINPAVTFGLFLARK
6	114-138	2590.5	2670.4	VSLLRALVYMIAQCLGAICGVGLVK
7	139-142	496.3		AFMK
8	143-161	1913.9		GPYNQFGGGANSVALGYNK
9	162-186	2570.4		GTALGAEIIGTFVLVYTVFSATDPK
10	187-237	5367.9		RSARDSHVPILAPLPIGFAVFMVHLATIPITGTGINPARSFGPAVIFNSNK
11	238-270	3732.9		VWDDQWIFWVGPFIGAAVAAAYHQYVLRAAAIK
12∗	271-281	1163.6	1243.5	ALGSFRSNPTN

∗The identified fragment is indicated with an asterisk.

2.3 Results: Mutants of SoPIP2;1

2.3.1 Expression of alanine and aspartate mutants of phosphorylation sites S115 and S274

As a consequence of the impossibility to completely phosphorylate and dephosphorylate SoPIP2;1 in 2D crystals, the study of mutants of both phosphorylation sites was encountered. Mutating serine into alanine prevents phosphorylation at this site, while a mutation to aspartate mimics a phosphorylated serine. Both potential phosphorylation sites were thus mutated to alanine and to aspartate, overexpressed in *Pichia pastoris* like the wild type [57], purified and reconstituted into 2D crystals.

Cloning, Transformation and Expression

pPICZB with subcloned SoPIP2;1 was kindly provided by the laboratory of Per Kjellbom, Sweden [57]. Primers were designed to introduce single amino acid mutations into the SoPIP2;1 gene by PCR. The nucleotide sequence of the SoPIP2;1 gene is shown in 2.9 and the resulting amino acid code is given in every other line, the two mutated serines are highlighted in red. The PCR product was linearized and transformed into yeast cells by electroporation. The construct was integrated into the *Pichia pastoris* genome by homologous recombination, and recombinant yeast cells were selected using the antibiotic Zeocin as selection marker. Since gene expression was under the control of the AOX1 alcohol oxidase promoter, protein production was induced by switching from glycerol to methanol as carbon source in the growth medium. Induction was kept up for several days before cells were harvested and disrupted using the Bead Beater method. Pelleted membranes were homogenized and stored at -70°C before purification.

```
#1       ATG TCT AAG GAA GTA AGT GAA GAA GCA CAA GCT CAC CAA CAT GGA
         M   S   K   E   V   S   E   E   A   Q   A   H   Q   H   G

#46      AAG GAC TAC GTA GAT CCA CCA CCA GCA CCA TTC TTT GAC TTA GGG
         K   D   Y   V   D   P   P   P   A   P   F   F   D   L   G

#91      GAG CTC AAA TTG TGG TCT TTC TGG AGA GCT GCT ATT GCT GAG TTT
         E   L   K   L   W   S   F   W   R   A   A   I   A   E   F

#136     ATT GCG ACG CTT TTG TTT CTA TAC ATA ACC GTC GCC ACT GTC ATT
         I   A   T   L   L   F   L   Y   I   T   V   A   T   V   I

#181     GGT CAC TCC AAG GAA ACT GTT GTT TGT GGT TCT GTT GGC CTT CTT
         G   H   S   K   E   T   V   V   C   G   S   V   G   L   L

#226     GGT ATT GCT TGG GCT TTT GGT GGC ATG ATC TTT GTC CTT GTT TAC
         G   I   A   W   A   F   G   G   M   I   F   V   L   V   Y

#271     TGC ACC GCC GGT ATC TCT GGA GGG CAC ATC AAC CCA GCA GTG ACT
         C   T   A   G   I   S   G   G   H   I   N   P   A   V   T

#316     TTC GGA CTA TTC CTA GCA AGG AAG GTG TCC TTA CTA AGG GCA CTA
         F   G   L   F   L   A   R   K   V   S   L   L   R   A   L

#361     GTC TAC ATG ATA GCC CAA TGT TTA GGA GCC ATA TGT GGT GTA GGA
         V   Y   M   I   A   Q   C   L   G   A   I   C   G   V   G

#406     CTA GTG AAG GCC TTC ATG AAG GGT CCT TAC AAC CAA TTT GGT GGT
         L   V   K   A   F   M   K   G   P   Y   N   Q   F   G   G

#451     GGG GCT AAC TCT GTT GCT CTT GGA TAC AAC AAA GGT ACT GCC TTA
         G   A   N   S   V   A   L   G   Y   N   K   G   T   A   L

#496     GGA GCT GAG ATT ATC GGC ACC TTT GTT CTT GTG TAC ACC GTC TTC
         G   A   E   I   I   G   T   F   V   L   V   Y   T   V   F

#541     TCT GCT ACT GAC CCT AAG AGG AGC GCA CGT GAC TCT CAC GTG CCT
         S   A   T   D   P   K   R   S   A   R   D   S   H   V   P

#586     ATC TTG GCC CCA CTT CCC ATT GGT TTT GCT GTG TTC ATG GTT CAC
         I   L   A   P   L   P   I   G   F   A   V   F   M   V   H

#631     TTG GCC ACT ATT CCC ATC ACT GGC ACT GGT ATC AAC CCT GCT AGA
         L   A   T   I   P   I   T   G   T   G   I   N   P   A   R

#676     AGC TTT GGC GCT GCT GTT ATC TTC AAC AGC AAC AAG GTT TGG GAT
         S   F   G   A   A   V   I   F   N   S   N   K   V   W   D

#721     GAC CAA TGG ATA TTC TGG GTC GGA CCA TTC ATT GGA GCA GCA GTA
         D   Q   W   I   F   W   V   G   P   F   I   G   A   A   V

#766     GCA GCA GCA TAC CAC CAA TAT GTA TTG AGG GCA GCA GCA ATT AAG
         A   A   A   Y   H   Q   Y   V   L   R   A   A   A   I   K

#811     GCG TTG GGA TCC TTC AGA AGC AAC CCT ACC AAT TAA
         A   L   G   S   F   R   S   N   P   T   N   .
```

Figure 2.9: The nucleotide and corresponding amino acid sequences of SoPIP2;1. The two putative phosphorylation sites that were mutated into both alanine and aspartate are highlighted in red.

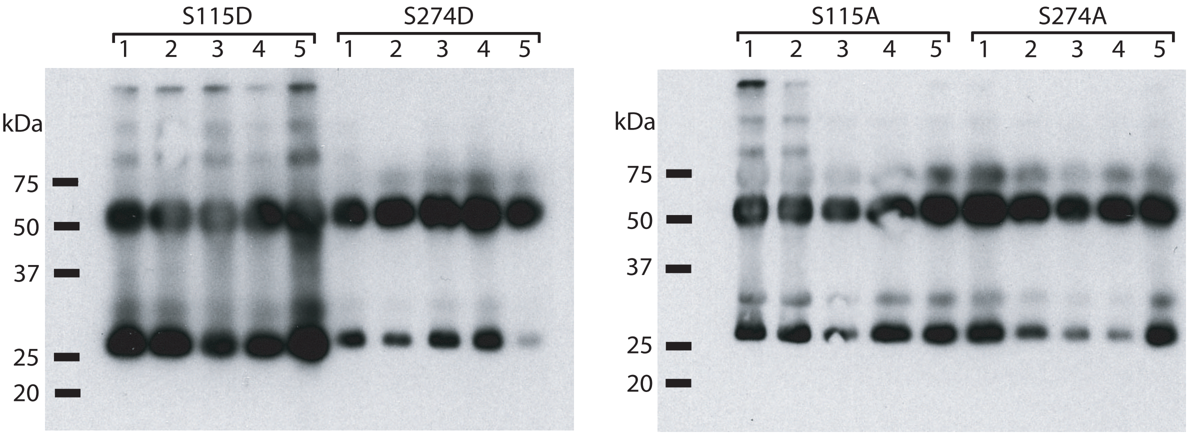

Figure 2.10: 5 clones of each mutant were checked for expression after induction by growth on methanol during 3 days. The following clones were selected for long term storage and large scale expression: 1 and 5 for S115D, 3 and 4 for S274D, 1 and 5 for S115A, 1 and 5 for S274A.

Screening for best expressing clones and following time course of expression

Selection of successfully recombined cells has been carried out on plates with increasing antibiotic concentrations. As multiple insertions are possible to occur during homologous recombination, yielding in increased protein production as well as increased Zeocin resistance, it is desirable to select a clone that grows and expresses the protein of interest on as high antibiotic concentrations as possible. Therefore five clones of each mutant were picked from the plate with highest Zeocin concentration and checked for expression after three days by Western Blot analysis (Fig. 2.10). All clones express SoPIP2;1 mutants at high levels, yet the 2 clones of each mutant giving the strongest signal were prepared for storage in glycerol stocks and further large-scale expression. It might be noteworthy that clones of S274D do not show trimer and tetramer bands but a very strong dimeric band, while S115D has equally strong dimer and monomer bands and is also present in higher oligomeric bands. This observation is less pronounced for the alanine mutants, yet S274A displays also more intense dimer than monomer bands. As the signal is generally very strong, most monomer and some dimer bands are again present as double bands, similar to those observed during phosphorylation experiments, but running at slightly higher apparent molecular weights (see 2.2.4). To check the time-dependance of protein production, one clone of each mutant was chosen and grown for 5 days after induction by exchange to growth on methanol medium. To compensate for evaporation and consumption, 0.5% methanol had to be added daily. Samples were taken every 24 h, starting at time point 0 when protein production was induced, cells were harvested by centrifugation and stored at -20° until they were checked by Western Blot analysis (Fig. 2.11). All mutants showed similar expression levels, expressing SoPIP2;1 already after 1 day

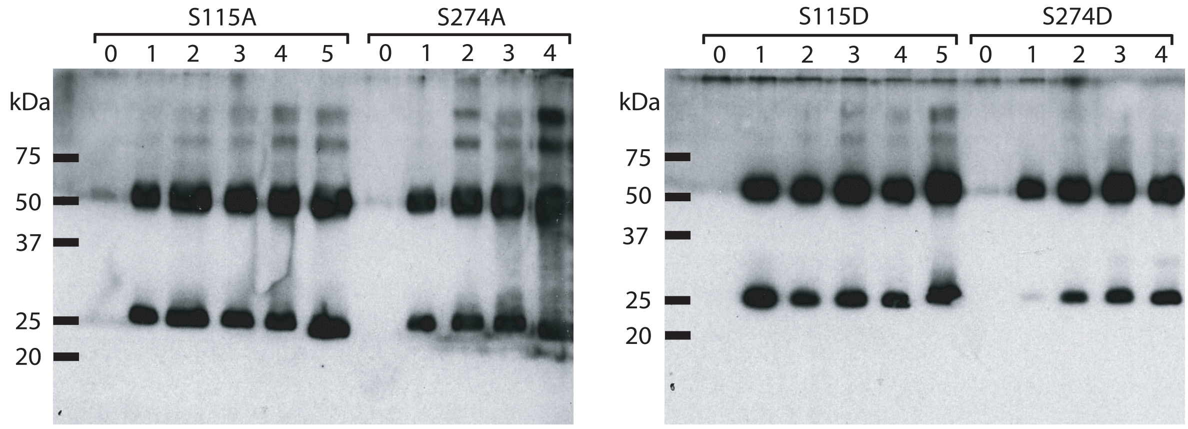

Figure 2.11: To follow the time-dependance of expression, samples were taken every 24h, starting from induction up to 5 days of growth (time points 0-5). Expression levels are high already after 1-2 days and do not remarkably increase after 3 days.

at relatively high levels. Expression still increases until day 3, it remains however more or less constant from then on. Consequently, subsequent large scale protein production was induced during 3 days.

2.3.2 Purification and 2D crystallization of mutant SoPIP2;1 forms

The native form of SoPIP2;1 overexpressed in *Pichia pastoris* was purified as described in 2.2.1: A cation exchange chromatography was performed after solubilization in OG, which yielded highly pure protein for 2D crystallization. The same cation exchanger protocol was applied first to purification of the alanine mutants, resulting in an elution of pure protein but also a considerable loss during flowthrough and wash of the column. This losses might have occured as well for native SoPIP2;1 but were negligible due to the high level of expression. However, when the same protocol was applied to purify the aspartate mutants S115D and S274D, only very small amounts of protein were found to have bound to the column. This was even more pronounced for S274D, where almost no protein could be detected by SDS-PAGE of the elution fractions. Due to the additional introduction of negative charges by the aspartates, the theoretical pI of the protein had changed from 9.03 to 8.86. The effective pI of the aspartate mutants can be even lower since the negative charges are presumably on the protein surface, specially in the case of S274D on the C-terminus which is highly exposed to the environment. For efficient binding to the cation exchange column it is however important to use a pH at least 1 unit below the pI of the protein. Although the pH of binding and washing buffer were adjusted according to these considerations, the binding of the aspartate mutants was not at its optimum yet. It turned out to be crucial to adjust solubilization and washing buffers by using phosphate buffer and in order to avoid any salt concentrations above 25 mM

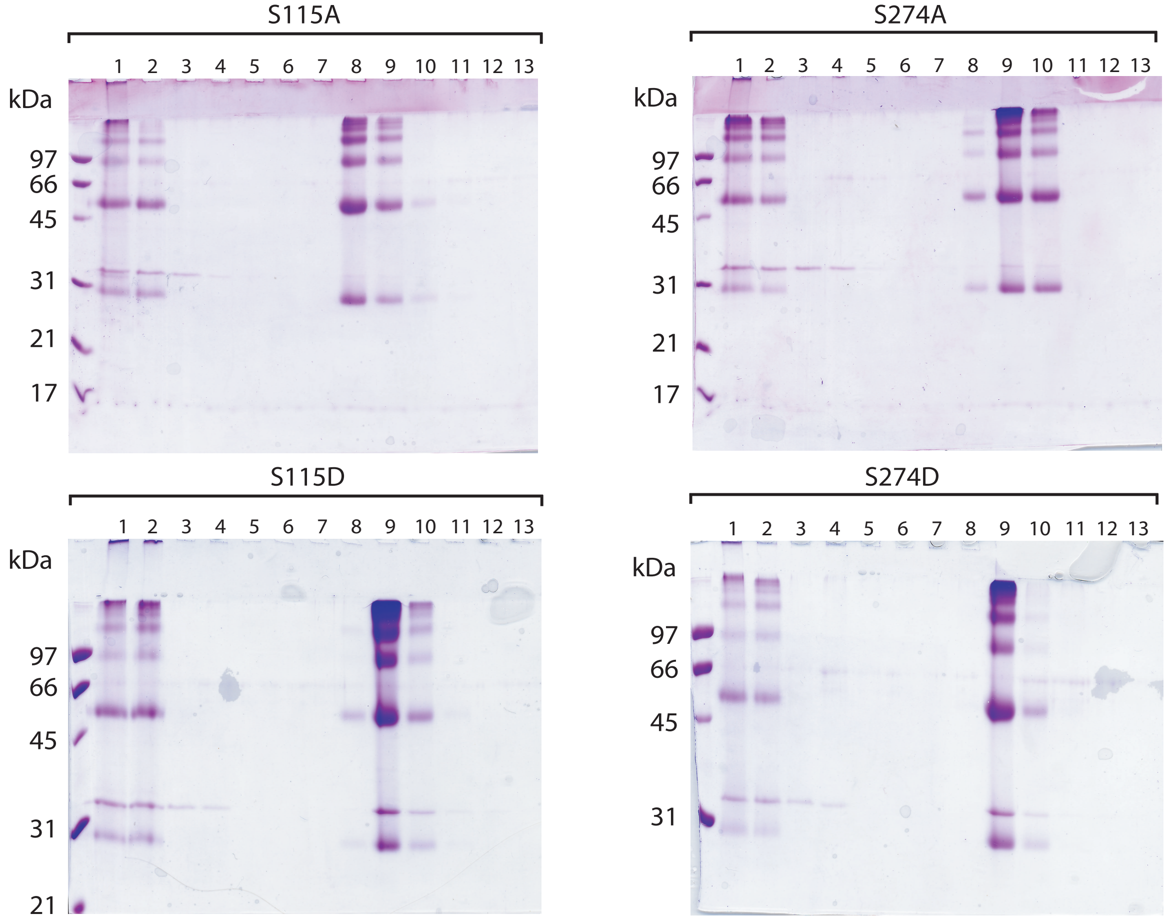
S115A
1 2 3 4 5 6 7 8 9 10 11 12 13
kDa
97
66
45
31
21
17
S274A
1 2 3 4 5 6 7 8 9 10 11 12 13
kDa
97
66
45
31
21
17
S115D
1 2 3 4 5 6 7 8 9 10 11 12 13
kDa
97
66
45
31
21
S274D
1 2 3 4 5 6 7 8 9 10 11 12 13
kDa
97
66
45
31

Figure 2.12: SDS-PAGE monitoring purifications of SoPIP2;1 mutants. Numbering of lanes: 1) Membranes after urea/alkaline stripping. 2) Solubilized material. 3) Flowthrough column. 4) - 7) Wash fractions W1 - W4. 8) - 13) Elution fractions E1 - E6.

during binding. Elution was done using 200 mM NaCl. All mutants were successfully purified according to this protocol (Fig 2.12). Despite a minor impurity observed on the SDS-PAGE, the homogenity and tetrameric state of all four mutants could be confirmed by single particle electron microscopy. Protein yields of approx. 10 mg per liter of culture were similar for all 4 mutants, but still much lower than reported for the wild type, where 25 mg per liter of culture were achieved [57]. The protein concentrations obtained were between 2 - 4 mg/ml, allowing the set up of 2D crystallization at a scale comparable to the wild type. All four mutants crystallized readily at the conditions known for wild type SoPIP2;1. By screening the samples using negative stain electron microscopy, the crystals were found to be mostly double-layered sheets of several μm in size with a rectangular lattice of a = b = 65 Å, as for the wild type (Fig 2.13).

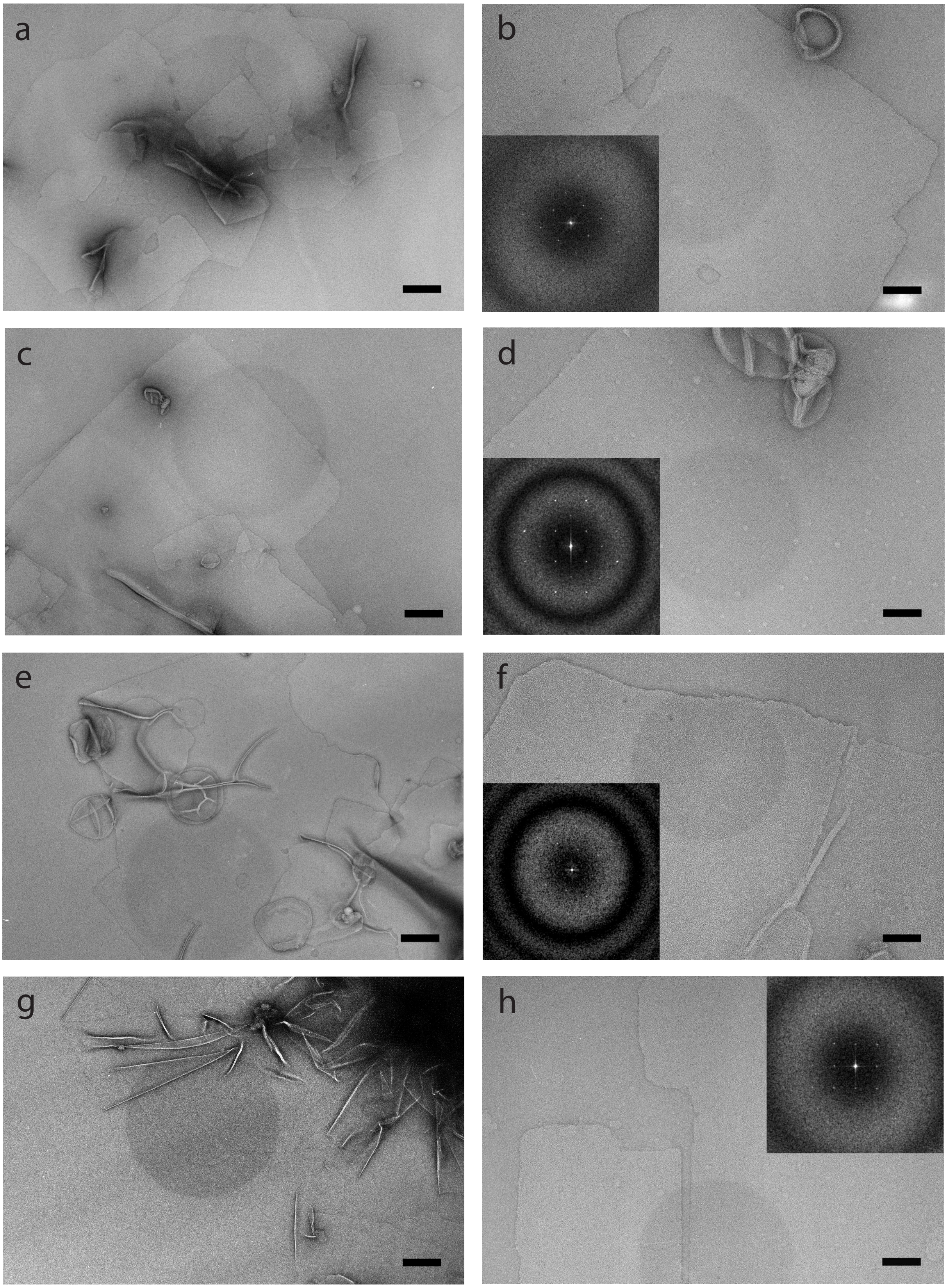

Figure 2.13: 2D crystals of SoPIP2;1 mutants. On the left, overview images taken at a magnification of 10'000x are given, while on the right side electron micrographs taken at 50'000x magnification are shown with power spectra of crystalline regions as insets. a) and b) show crystals of mutant S115A, c) and d) are crystals of S274A, e) and f) correspond to S115D, g) and h) are crystals of mutant S274D. Scale bars are 500 nm in a, c, e, g and 100 nm in b, d, f, h, respectively.

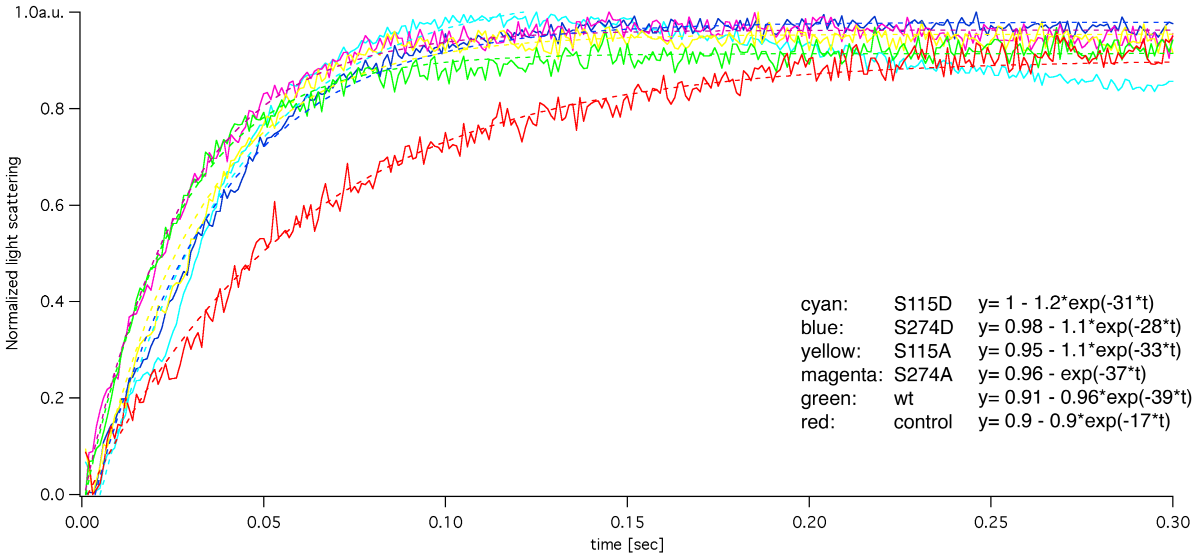

Figure 2.14: Activity of SoPIP2;1 wild type and mutants reconstituted at LPR 90, compared to empty *E. coli* lipid vesicles as control. Color coding of traces and corresponding fitted single exponential equations are given in the figure legend.

2.3.3 Structural analysis by electron crystallography

Samples for electron diffraction by cryo electron microscopy where prepared using a different technique than the glucose-embedding method used for the wild-type. Crystals were adsorbed on Quantifoil® holey carbon grids, quick-frozen in liquid ethane and imaged only where crystalline sheets were covering the holes in the carbon film. A resulting diffraction pattern of high quality is shown in Fig. 2.16. Diffraction spot (26,10), which corresponds to a resolution of 2.3 Å, is highlighted by a circle. Such a high resolution was achieved immediately in a first attempt, indicating that this new preparation method using holey carbon grids gives diffraction patterns of superior quality than the previously used glucose embedding method (see 2.2.3).

2.4 Results: Water Channel Activity of Wild type and Mutant SoPIP2;1

To measure the activity of mutant SoPIP2;1 compared to the wild type and to empty control vesicles, a standard method combining stopped flow with 90° light scattering was used, as previously described for many aquaporins as well as heterologously expressed SoPIP2;1 [76, 77, 57]. For these experiments, all isoforms were reconstituted at LPRs 30, 60 and 90 into proteoliposomes using *E. coli* polar lipids. After exposing proteoliposomes to an inwardly directed sucrose gradient, the time-course of light scattering that increases due to shrinking of proteoliposomes was recorded. In Fig. 2.14, average traces of all five isoforms at LPR 90 plus the control are plotted against time. To determine the rate constants of water transport, the curves were fitted to model equations. The kinetics of the water efflux are those of a first order reaction with a linear decrease of the reaction rate $\frac{da}{dt}$, which describes the change of signal a over time t. Hence the reaction obeys the equation: $-\frac{da}{dt} = ka$ with the rate constant $k = [s^{-1}]$ In the integrated form, the reaction will become a single exponential equation: $a = a_0 e^{-kt}$. In our case, the signal (the change in light scattering) increases with time until it reaches saturation, thus $a = 1 - a_0 e^{-kt}$. From Fig. 2.14 it is clear that all isoforms show water transport activity higher than the control vesicles, exhibiting rate constants of 28 - 39 s^{-1} in contrast to 17 s^{-1} for the control. There are however no clear differences between individual mutants and the wild type, suggesting that all isoforms have similarly high water transport rates. A similar picture is obtained at other LPRs. A reliable evaluation of the given data is however problematic since some averaged traces fit better to double-exponential equations while other fit to single-exponentials, making exact quantitative comparisons impossible. Morever, when plotting different LPRs of one individual mutant or the wild type, no distinction between the LPRs can be made, although this would be a prerequisite for a more quantitative analysis.

2.5 Discussion: Wild Type SoPIP2;1

2.5.1 2D crystallization of wild type SoPIP2;1

The strong improvement of crystal quality due to the presence of 50 mM $MgCl_2$ confirms the important role of divalent ions in 2D crystallization of membrane proteins. It is required for 2D crystallization of many aquaporins (see table 3.3) as well as other membrane proteins like photosystem I reaction center, bovine lens connexin and outer membrane porins [78, 79, 80]. A possible role for $MgCl_2$ is modulation of electrostatic interactions by influencing charges of the lipid bilayer surface [65]. But the presented results also suggest to reconsider the role and necessity of purification tags. The expression level of SoPIP2;1 in *Pichia pastoris* allows an easy purification of the untagged protein with an even simpler protocol than for the His-tagged version because the binding time to the Ni-NTA column material is left out. Thus in the case of SoPIP2;1, the His-tag is not only unnecessary but turned out to interfere with the optimal crystallization conditions, as the addition of 50 mM $MgCl_2$ which is crucial to form highly ordered 2D crystals of SoPIP2;1 leads to aggregation of His-tagged SoPIP2;1.

The presumable correlation between pI of the protein and the optimal pH for crystallization does not withstand the experimental results. The theoretical pI of His-tagged SoPIP2;1 is 7.78 while it crystallizes best at pH 9 - 9.5. Untagged SoPIP2;1 has a calculated pI of 9.03 and a pH optimum for crystallization around 7 - 8. Thus while His-tagged SoPIP2;1 crystallizes at higher pH meaning that it carries positive net charges, untagged SoPIP2;1 seems to crystallize at negative net charges. However, conclusions implicating the theoretical pI of membrane proteins have to be treated with caution since charged residues might be buried within the protein and local charges on the protein surface exposed to the solvent mainly contribute to the apparent electrostatics. Because the change in pI between His-tagged and untagged SoPIP2;1 is due to the additional 22 amino acids at the C-terminus, which is likely to be surface exposed, the additional charges might very well change the electrostatic behavior of SoPIP2;1.

2.5.2 The 5 Å structure of SoPIP2;1

An elaborated discussion of the structure of SoPIP2;1 is given in Appendix A. In short, the specific arrangement of helices 1 and 2 and the connecting loop A are pointed out and their possible in vivo role is discussed. The tongue-and-groove packing of the two extracellular faces of the crystalline layers is presumably stabilized by loop A which sticks out of the membrane plane and fills the space between adjacent tetramers of the opposing layer. This specific assembly might represent native protein-protein interactions within invaginations of the plant plasma membrane that accompany fast volume changes of the plant cell. PIP subfamily members have been associated with such plasmalemmasomes [81]. Other members of the aquaporin family have been found to play roles in cell adhesion. AQP0 forms junctions in fiber cells of the eye lens which are also stabilized by loop A [22]. AQP4 occurs in ordered arrays in glial lamellae of the hypothalamus. A recently reported electron crystallographic structure suggests that in these orthogonal arrays AQP4 plays a key role in membrane adhesion [21]. Both AQP0 and AQP4 2D crystals were double-layered, sticking together with their extracellular faces, and the molecular interactions leading to the membrane junction were derived from crystal contacts between the two crystalline layers. While AQP0 tetramers of the two layers share the four-fold axis, one layer of the AQP4 crystal is shifted by half a unit cell in x- and y-direction with respect to the other. Hence, AQP4 packs an arrangement identical to that of SoPIP2;1. These examples demonstrate the combination of water channel function and cell adhesion in aquaporins, a double function that needs further investigation to possibly identify other members with adhesive properties.

2.5.3 Phosphorylation and dephosphorylation of 2D crystals of SoPIP2;1

Experiments aiming a complete and detectable phosphorylation or dephosphorylation of one or both putative phosphorylation sites S115 and S274 of SoPIP2;1 were undertaken. However, only partial phosphorylation by Protein Kinase C could be achieved using radioactively labeled phosphate, while dephosphorylation by Alkaline Phosphatase could not be clearly demonstrated. Nevertheless some resulting details should be considered. A comparison between the autoradiography, which monitors the phosphorylation reaction, and the corresponding SDS-PAGE shows a discrepancy between the intensity of radioactivity signals and Coomassie staining of the individual bands that represent monomers, dimers, trimers and tetramers of SoPIP2;1 (Fig. 2.6). The tetrameric band, which is the weakest band on the Coomassie stained SDS-PAGE, is the one that is best phosphorylated. Because lower oligomeric states are a result of solubilization by SDS and SoPIP2;1 was present only as tetramer at the time the reaction took place, one can conclude that phosphorylation tends to stabilize the tetramer against solublization in SDS. It must be pointed out that the X-ray structure and molecular dynamics on SoPIP2;1 that were proposed by [61] suggest an interaction between unphosporylated S274 with a neighboring monomer, while in the open conformation the C-terminus is disordered. This interpretation would suggest that phosphorylation, which is assumed to lead to the open conformation, induces a destabilization rather than a stabilization of the tetrameric complex. As to the mobility shift towards lower molecular weights observed on gel 2.6, one could argue that only the uncleaved protein was phosphorylated, while the cleaved one lacking the C-terminus cannot be phosphorylated. Nevertheless, what can be phosphorylated remains in a higher oligomeric state, while unphosphorylated (and possibly cleaved) tetramers fall apart in SDS. On the other hand, the poor incorporation of γ-^{32}P-ATP is still true in other experiments, where no apparent loss of molecular weight is observed (Fig. 2.8), suggesting that this loss does not significantly influence the experiment.

The band shift that was observed in the next phosphorylation experiment, where previously dephosphorylated crystals were used, could not be identified as a phosphorylation-induced mobility shift like in cases described for other proteins [69, 70, 72]. To distinguish whether it is a matter of proteolytic activity or posttranslational modification, mass spectroscopy after extraction from excised bands could be used.

The use of radioactively labeled ATP is not the only possibility for detecting phosphorylation. There are commercially available phosphoprotein gel stains like Pro-Q® Diamond stain, or antibodies that specifically detect phosphorylated residues within a particular epitope. Several trials to use the Pro-Q Diamond stain were undertaken but without success; the detected signal was too weak in any case to discriminate between phosphorylated and control protein. As a pre-requisite for the use of phospho-specific antibodies, the sequence around the phosphorylated residue must correspond to a known epitope for one of the commercially available antibodies. Still, the efficiency of detection depends on the accessibility and folding of the epitope. Attempts with such antibodies were done in the collaborating laboratory of Per Kjellbom, but did not give any results (E. Alexandersson, pers. com.).

Recently, the characterization of two protein kinases acting on SoPIP2;1 in vivo was reported

[82]. The kinase phosphorylating S115 was found to be in the soluble protein fraction from spinach leaves, while the kinase for S274 was identified as membrane associated CDPK. Both kinases could be partly purified and shown to phosphorylate peptides containing the two phosphorylation sites in in vitro and in-gel phosphorylation assays. However no sufficient amounts of the kinases could be isolated for identification by mass spectroscopy and subsequent use for complete phosphorylation of purified SoPIP2;1.

An example of successful phosphorylation of a plant aquaporin and detection of the phosphorylation by mass spectroscopy was recently reported by [40]. The seed-specific PvTIP3;1 was previously shown to be acitvated by Ca^{++}-dependent phosporylation [39]. Three potential phosphorylation sites for calcium dependent protein kinase (CDPK) were found in the sequence: S7, S23 and S99. Daniels and Yeager [40] have shown by mass spectroscopy that only S7 was phosphorylated in native PvTIP3;1. Also, this residue was the only one to be phosphorylated in vitro by protein kinase A (PKA). S7 lies in a model consensus sequence for PKA (Arg-Arg-X-Ser/Thr-B where B is a large hydrophobic residue), while S23 and S99 lie in the rather poor PKA motif Arg-X-Ser. Molecular modeling revealed that S23 is deeply buried in the lipid bilayer within transmembrane helix 1 and S99 which is located amino-terminally at transmembrane helix3 on the turn following the first halfhelix. The authors argue that for these sterical reasons, rather than due to their poor PKA signal sequence, those two residues are not likely to be accessible to kinases [40]. A sequence comparison with SoPIP2;1 shows that inaccessible S99 in PvTIP3;1 corresponds to S115 in SoPIP2;1, challenging the suggestion that phosphorylation of S115 is involved in gating of the channel [61] (Fig. 2.15).

2.5.4 Determination of the phosphorylation state of 2D crystallized SoPIP2;1 by mass spectroscopy

To determine whether the putative phosphorylation sites S115 and S274 are phosphorylated in 2D crystals of SoPIP2;1, a series of experiments consisting of proteolytic or chemical digestion followed by LC-MS were performed. As a result, digestion with endoproteinase LysC followed by LC ESI-MS allowed identification of S274 as unphosphorylated. However, all experiments concerning the phosphorylation state of S115 failed. Mass spectroscopic analysis of membrane proteins encounters several problems, of which many have emerged during attempts to analyze the phosphorylation state of S115. First, cleavage sites can be inaccessible if they are located in large hydrophobic regions, resulting in incomplete digestions. This problem can be avoided by chemical cleavage under denaturing conditions. It remains still the difficulty of separating very hydrophobic fragments by chromatographic methods. Furthermore, ionization of hydrophobic peptides is much more difficult than in the case of soluble ones.

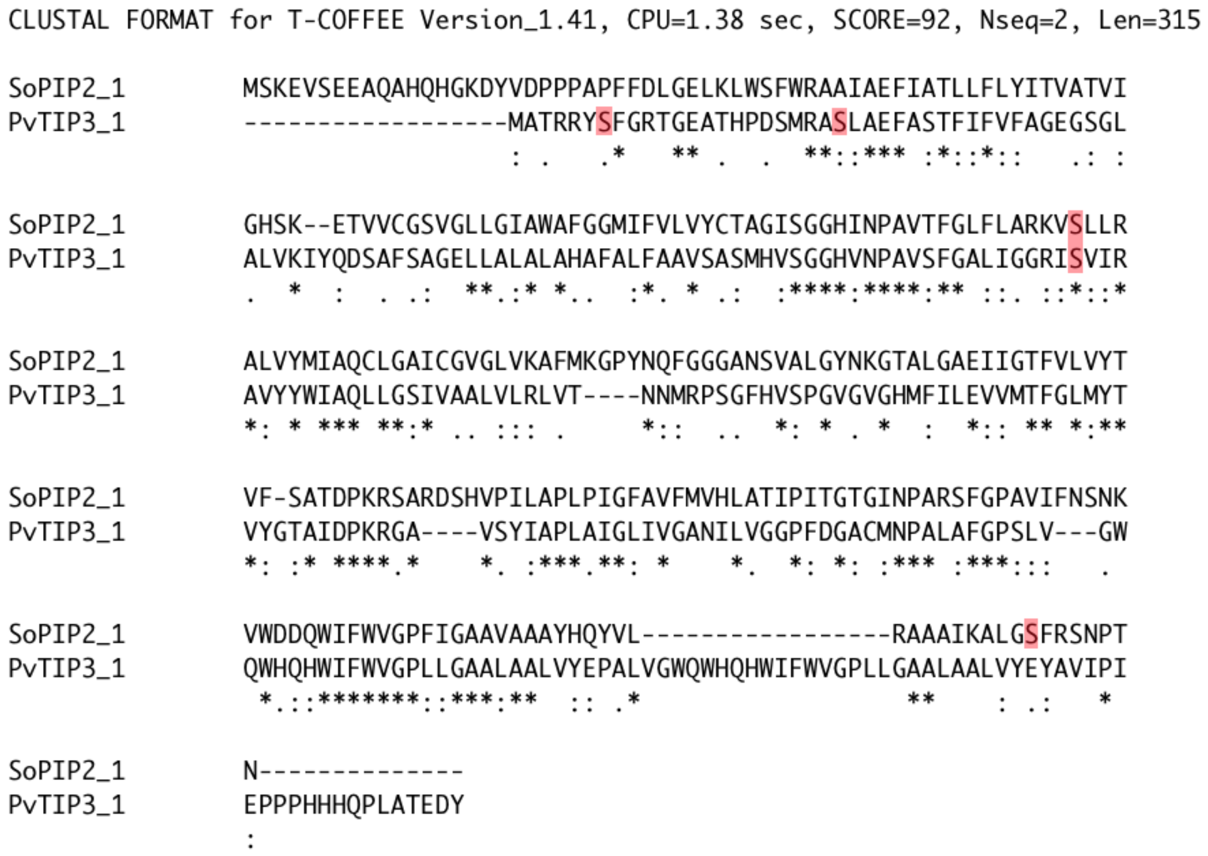

```
CLUSTAL FORMAT for T-COFFEE Version_1.41, CPU=1.38 sec, SCORE=92, Nseq=2, Len=315

SoPIP2_1        MSKEVSEEAQAHQHGKDYVDPPPAPFFDLGELKLWSFWRAAIAEFIATLLFLYITVATVI
PvTIP3_1        ------------------MATRRYSFGRTGEATHPDSMRASLAEFASTFIFVFAGEGSGL
                                  : .   .*   ** .  .  **::*** :*::*::   .: :

SoPIP2_1        GHSK--ETVVCGSVGLLGIAWAFGGMIFVLVYCTAGISGGHINPAVTFGLFLARKVSLLR
PvTIP3_1        ALVKIYQDSAFSAGELLALALAHAFALFAAVSASMHVSGGHVNPAVSFGALIGGRISVIR
                .  *  :  . .:  **.:* *..  :*. *  .:  :****:****:** ::. ::*::*

SoPIP2_1        ALVYMIAQCLGAICGVGLVKAFMKGPYNQFGGGANSVALGYNKGTALGAEIIGTFVLVYT
PvTIP3_1        AVYYWIAQLLGSIVAALVLRLVT----NNMRPSGFHVSPGVGVGHMFILEVVMTFGLMYT
                *: * *** **:* .. ::: .     *::  ..  *: * . *  :  *:: ** *:**

SoPIP2_1        VF-SATDPKRSARDSHVPILAPLPIGFAVFMVHLATIPITGTGINPARSFGPAVIFNSNK
PvTIP3_1        VYGTAIDPKRGA----VSYIAPLAIGLIVGANILVGGPFDGACMNPALAFGPSLV---GW
                *: :* ****.*    *. :***.**: *    *.  *: *: :*** :***:::   .

SoPIP2_1        VWDDQWIFWVGPFIGAAVAAAYHQYVL-----------------RAAAIKALGSFRSNPT
PvTIP3_1        QWHQHWIFWVGPLLGAALAALVYEPALVGWQWHQHWIFWVGPLLGAALAALVYEYAVIPI
                 *.::*******::***:**  :: .*                  **    : .:   *

SoPIP2_1        N--------------
PvTIP3_1        EPPPHHHQPLATEDY
                :
```

Figure 2.15: Sequence alignment of SoPIP2;1 to PvTIP3;1. Putative phosphorylation sites are highlighted in red. According to [40], S99 in PvTIP3;1 which corresponds to S115 in SoPIP2;1 is sterically not accessible to kinases and therefore not a phosphorylation site in vivo. The sequence alignment was done using T-COFFEE at http://www.ch.embnet.org

As mentioned in the discussion about phosphorylation experiments, a successfull determination of the phosphorylation state of a plant aquaporin by mass spectroscopy was presented by [40]. Using chemical digestion by CNBr, a sequence coverage of 79% of the amino acid sequence could be achieved. And most importantly, a hydrophobic fragment corresponding to the B-loop of SoPIP2;1 which contains S115 could be identified. The protocol used in this paper was not yet applied to SoPIP2;1, it remains thus unclear if S115 in SoPIP2;1 is phosphorylated or not.

2.6 Discussion: Mutants of SoPIP2;1

To elucidate the structural role of phosphorylation in the gating of SoPIP2;1 by electron crystallography, a major fraction of crystallized protein must be in a defined phosphorylation state. Despite all attempts it was not possible to obtain large portions of unambiguously ascertained phosphorylated or dephosphorylated SoPIP2;1 by kinase/phosphatase treatments. As an alternative, it is a common approach to imitate phosphorylation and dephosphorylation by mutagenesis of potentially phosphorylated serines into alanines (unphosphorylated) and aspartates (phosphorylated). Recently published work on the Kv2.1 potassium channel is an excellent example where this kind of mutations helped elucidating the phosphorylation-dependent functionality of a membrane protein [71].

2.6.1 Expression and purification of SoPIP2;1 mutants

All four mutant forms of SoPIP2;1 behaved analogously to the wild type during expression in *Pichia pastoris*, indicating that the functional changes induced by the mutations, even if considerable, have no toxic or harmful effect on the cells. First differences became apparent when the aspartate mutants were purified according to the wild type protocol. Difficulties emerged due to the introduction of additional negative charges: The aspartate mutants seem to clearly differ in their isoelectric point and thus in their charge when compared to the wild type. This effect is even more pronounced if the aspartate is at the S274 position. From MS analysis it is known that the wild type expressed in *Pichia pastoris* is not phosphorylated at this position, which explains why the aspartate mutant shows different behavior. Though not as strong as in the case of S274D, the change in electrostatic behaviour was also observed for S115D, suggesting that the wild type form, produced in *Pichia pastoris*, is not phosphorylated at this position either.

2.6.2 2D crystallization and structural analysis of SoPIP2;1 mutants

Mutant forms of SoPIP2;1 crystallized at the same or very close conditions to those used for the wild type. It is therefore not likely that the electrostatic changes influencing the purification in such a strong manner are inducing large conformational changes. However, wild type SoPIP2;1 crystallized readily at a relatively broad range of conditions, being not very sensitive to e. g. changes in pH of 0.5 units or LPR of +/- 0.1. The alanine mutants have the same broad range of crystallization conditions, while the aspartate mutants seem to need more precise specifications of the parameters to form large, highly ordered crystalline sheets (pH 8, LPR 0.4, 50 mM MgCl). At slightly different conditions, smaller sheets, stacked membranes or vesicles were obtained instead of highly ordered large sheets. This might indeed be a consequence of the changes in charge at the positions of putative phosphorylation. The similarity in the appearance of the crystals, being double-layered sheets of the same unit cell dimensions like the wild type crystals, also indicates that no large changes in the structure are introduced by the mutations.

After the first screenings of crystallization trials in negative stain were done, the observed crystals were inspected by cryo EM. A new, improved technique for the preparation of 2D crystals for cryo EM makes use of commercially available Quantifoil holey carbon grids, on which crystals are adsorbed and quick-frozen in liquid ethane (M. Chami, unpublished results). It seems that by using this technique, a general improvement in resolution is achieved compared to glucose-embedding (Fig. 2.16). Beside beam-induced specimen charging, the roughness and wrinkling of the carbon film were shown to affect resolution in cryo EM [83, 84, 85]. These problems do not affect crystals prepared on holey carbon film if only crystalline regions covering the 1 μm holes are imaged. However, this technique is only applicable for 2D crystals of considerable size.

As an alternative to structure determination from digitized electron micrographs that were subjected to image processing using the traditional software tools for electron crystallography [86], electron diffraction data processing combined with molecular replacement methods has recently become very successful. It was a landmark in electron crystallography when the AQP0 structure was initially solved at 3 Å resolution, followed by an improved structure at 1.9 Å resolution [22, 23]. It is however still not a routinely used method, which is on one hand due to the sparseness of high quality electron diffraction patterns and on the other hand to the lack of generally accessible image processing software for the extraction of electron diffraction data. Although some groups within the EM community have produced home-made software solutions, these are often not available to the whole community or not generally applicable because they are too specific. A new software library for electron microscopic images (IPLT)

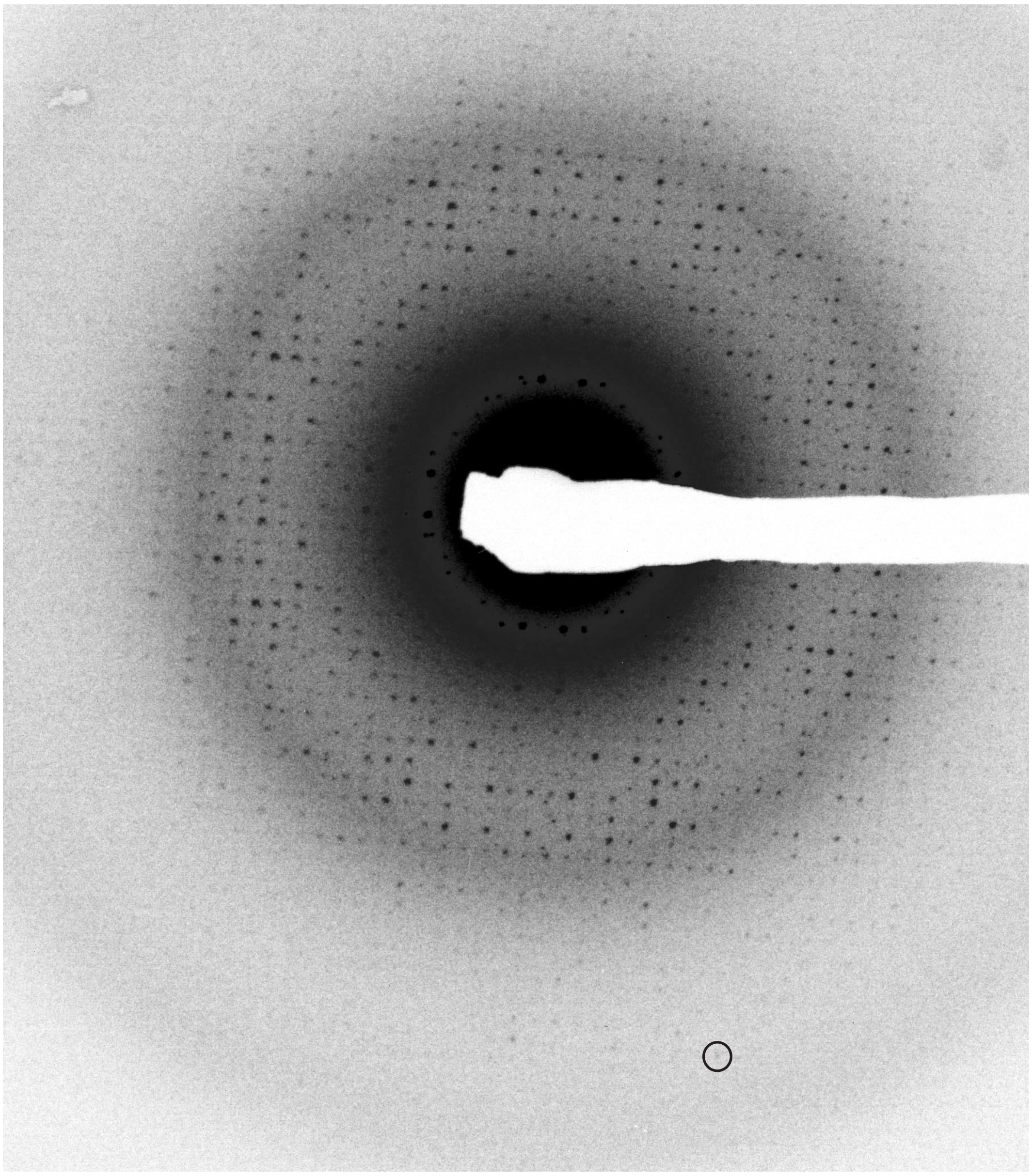

Figure 2.16: Electron diffraction pattern of a 2D crystal of the mutant S274A. The black circle indicates spot (26,10) which corresponds to a resolution of 2.3 Å.

being presently developed, provides among others tools for data extraction from electron diffraction patterns [68]. It is a direct objective of this project to process diffraction data of SoPIP2;1 wild type as well as mutants using the IPLT software to eventually solve the structures by molecular replacement. The expected improvement in resolution will hopefully give insight into the structural changes accompanying the mutations of potential phosphorylation sites.

2.7 Discussion: Water Channel Activity of Wild Type and Mutant SoPIP2;1

Two now well-established tests for water channel activity of aquaporins have been developed in the AQP field: In the first, cRNA of the aquaporin of interest is injected into Xenopus oocytes and their swelling after an osmotic shock is observed by light microscopy and compared to oocytes with no cRNA injected [5]. This experimental setup is used for identification of putative aquaporin family members as water channels. In the other test, purified protein is reconstituted into proteoliposomes and shrinking after an osmotic shock is observed by measuring changes in light scattering or fluorescence quenching, if proteoliposomes where produced in the presence of fluorescein [87, 88]. This test is specially usefull when heterologously expressed aquaporins need to be tested for proper folding and functional activity. Also, heterologously expressed SoPIP2;1 was shown to be active in this test, with a dependency of the rate constant on the LPR [57]. A third functional assay was recently developed for recombinant aquaporins expressed in *Pichia pastoris*. In this test, the change in optical absorbance of *Pichia pastoris* spheroplasts following an osmotic shock is measured. Optical absorption will increase with increased volume of spheroplasts, but if lysis occur (due to water channel activity), the optical absorbance will decrease [89].

To test the activity of SoPIP2,1 mutants, the proteoliposomes approach was used since it is well-characterized and was previously shown to be useful in determining the activity of wild type SoPIP2;1. As depicted in 2.4, all four mutants show similar water transport rates to the wild type when compared to control *E. coli* liposomes without protein. Problems arise when one wants to compare different LPRs of the same isoforms. The traces do not appear consistently as single- or double-exponentials, and the initial slopes of the traces do not allow distinctions between the individual LPRs. These artefacts do neither permit quantification of the resulting data nor any statements about which mutants are more active than others. Yet there are ways to interpret these results and to make suggestions for improvement of the experimental design in order to obtain data for a better comparison. The fitting to double instead of single exponential functions has already been observed for reconstituted CHIP28 (AQP1) and has been associated with varying size of the proteoliposomes [76]. Indeed mass and number of scatterers have been reported to have strong influences on the intensity of scattered light in such experiments [90]. To extract indications of osmotically induced changes to the proteoliposomes from the light scattering data, it is necessary to first account for changes in scattered light due to mass and number of proteoliposomes, or to strictly control those factors [90]. One pre-requisite is that all samples have to consist of one population of proteoliposomes having a defined diameter. Those can be produced using an extruder, a simple, commercially available device composed of two syringes and a filter unit of defined pore size in between. The sample is passed several times through the filter unit until a single population of particles with given size is obtained. Freeze-fracture EM of proteoliposomes, where single channels reconstituted in the membrane can be identified and statistically evaluated, would permit a more quantitative comparison [91].

In conclusion, the experiments aiming a functional characterization of the mutants and a quantitative comparison between mutants and wild type need to be redone with an improved experimental setup, in order to reproduce results published on the wild type [57] and extend these to the four mutants.

2.8 Materials and Methods

2.8.1 Purification and 2D crystallization of wild type SoPIP2;1

All purification steps were carried out at 4°C unless otherwise noted. Crude membranes were prepared according to [57] and stored at -70°C. Removal of peripheral proteins was achieved by urea/alkaline stripping as described by [92]: Approximately 2.5 ml crude membranes were homogenized in approximately 90 ml 4 M urea, 5 mM Tris-HCl; pH 9.5, 5 mM EDTA, 5 mM EGTA, 0.01% NaN_3, pelleted at 150'000 g, 1h, 4°C, homogenized in 20 mM NaOH, pelleted at 150'000 g, 1h, 4°C, homogenized in 5 mM Tris-HCl, pH 8, 2 mM EDTA, 2 mM EGTA, 100 mM NaCl, centrifuged at 150'000 g, 1h, 4°C and resuspended in 4 ml of 10 mM phosphate buffer; pH 7.8, 50 mM NaCl, 10% glycerol, 0.03% NaN_3. Aliquots of stripped membranes were stored at -20°C.

His-tagged SoPIP2;1 was solubilized in 6% OG at room temperature for 30 min. Unsolubilized material was pelleted by ultracentrifugation at 230'000 g, 4°C, 40 min. Solubilized protein was diluted 1:1 with buffer A (20 mM Hepes-NaOH; pH 7.8, 50 mM NaCl, 10 % (v/v) glycerol, 0.03 % NaN_3) and added to Ni-NTA agarose (1 ml bed volume per 20 ml protein solution) previously equilibrated with buffer B (20 mM Hepes-NaOH; pH 7.8, 300 mM NaCl, 10 % (v/v) glycerol, 2 % OG, 0.03 % NaN_3) with 2 mM histidine. For binding, the mixture was incubated at 4°C for 3h before transfer onto a Promega spin column (10 ml protein solution and 0.5 ml Ni-NTA bed volume per column). Bound protein was washed with 40x bed volume of buffer B with 1 mM histidine and 20x bed volume of buffer B with 2 mM histidine. The column bottom was closed before adding one bed volume of buffer B with 200 mM histidine and incubation at 4°C for 1h while shaking. The protein was eluted by centrifugation at 2000 rpm for 1 min. Elution 2 was collected after 10 min incubation time. Protein purity was checked by SDS-PAGE and the concentration was determined by measuring absorbance at 280 nm.

SoPIP2;1 without tag was solubilized in 6% OG at room temperature for 30 min. Unsolubilized material was pelleted by ultracentrifugation at 230'000 g, 4°C, 40 min. The protein solution was loaded on a BioRad mini column packed with CM Sepharose Fast Flow, previously washed with 10x bed volume 1M NaCl and equilibrated with 10x bed volume equilibration buffer (20 mM Bicine-NaOH; pH 8.75, 2% OG, 0.01% NaN_3). The column was washed with 10x bed volume of equilibration buffer and washes were collected in 1 ml fractions. The protein was eluted in 0.5 ml fractions with elution buffer (20 mM Bicine-NaOH; pH 8.75, 2% OG, 300 mM NaCl, 0.01% NaN_3). Protein purity and concentration were checked by SDS-PAGE and measuring absorbance at 280 nm. For crystallization, pure protein was mixed with OG-solubilized lipids at various LPR (see table 2.1) and protein end concentrations between 1 - 2.5 mg/ml and incubated for 1 - 2 hours prior to dialysis which was performed either in dialysis buttons or using an open flow dialysis machine [65]. The ternary mixture of protein, lipid and detergent was dialyzed against various buffers (see table 2.1) following a temperature profile of 24h room temperature, 24h 37°C and 24h room temperature.

2.8.2 Electron microscopy

The quality of crystallization trials was initially checked by negative stain electron microscopy. 4 μl sample were adsorbed for 1.5 min to carbon-coated copper grids previously rendered hydrophilic by glow discharging, washed three times with water and stained twice 12 sec with 5 μl of 2% uranyl acetate. Electron micrographs were taken at a Hitachi-H8000 transmission electron microscope operated at 200 kV.

Best-diffracting samples were imaged in cryo EM for structure determination. Crystal samples were embedded in 2% glucose on molybdenum grids covered with a carbon film that was previously evaporated on mica and floated on the grid. For taking tilt series, a second carbon film was evaporated on the back side of the grid after sample adsorption to decrease the effect of beam-induced specimen charging [83]. Electron micrographs of tilted specimen were taken at magnifications of 50'000x with a Philips CM200 FEG operated at 200 kV. The quality of the micrographs was evaluated by diffraction on an optical bench with a laser beam. Best-diffracting negatives were digitized at a stepsize of 5 μm using a Heidelberg Primescan drum scanner.

2.8.3 Electron diffraction

Electron diffraction patterns were recorded at low electron doses ($<$5 electrons per Å^2) on a Gatan 2Kx2K CCD camera with a Philips CM200 FEG operated at 200 kV. Electron doses were measured by aligning the CM200 according to the usual alignment protocol for diffraction with a camera length of 1 m. Without changing lens settings, spotsize or apertures, the mode

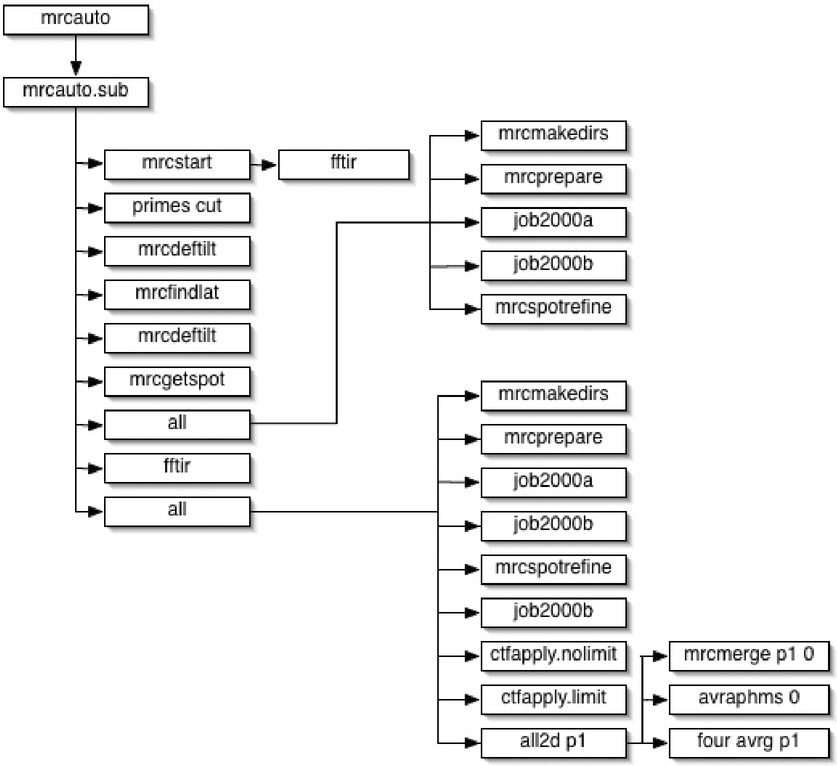
mrcauto
mrcauto.sub
mrcstart
fftir
primes cut
mrcdeftilt
mrcfindlat
mrcdeftilt
mrcgetspot
all
fftir
all
mrcmakedirs
mrcprepare
job2000a
job2000b
mrcspotrefine
mrcmakedirs
mrcprepare
job2000a
job2000b
mrcspotrefine
job2000b
ctfapply.nolimit
ctfapply.limit
all2d p1
mrcmerge p1 0
avraphms 0
four avrg p1

Figure 2.17: Overview of the automated image processing proceeding using the MRC image processing software.

was set to imaging instead of diffraction and images were taken on Kodak SO 163 film, both at 50'000x and 38'000x magnification. Optical densities of negatives were measured using a Heidelberg Primescan drum scanner in transmission mode.

2.8.4 Image processing and structure determination

Image processing was performed using the MRC crystallography program suite [86]. Briefly, images were corrected for lattice distortions, taking the Fourier-filtered images themselves as references. Phases and amplitudes were measured and corrected for the tilted contrast transfer function. Amplitudes and phases from processed images were merged imposing p4 symmetry. After phase origin refinement, lattice lines for the amplitudes and phases normal to the membrane plane were fitted to create a 3D data set. The proceeding of automated image processing that was used is displayed in Figs. 2.17, 2.18 and 2.19 in more detail. The automated processing is covered in the C shell script `mrcauto` that contains `mrcstart`, which creates the DATAFILE.dat in the image directory. `primes cut` checks the image size for its prime numbers, while `mrcdeftilt` determines the tilt geometry from defocus values at 49 locations on the image. If there is no fourier transform at this point, `fftir` will create one. Also, the defocus of the image is determined at the image center. `mrcfindlat`: Briefly, the lattice is determined and the spotlist generated. Therefore, the FFT of the image is blurred

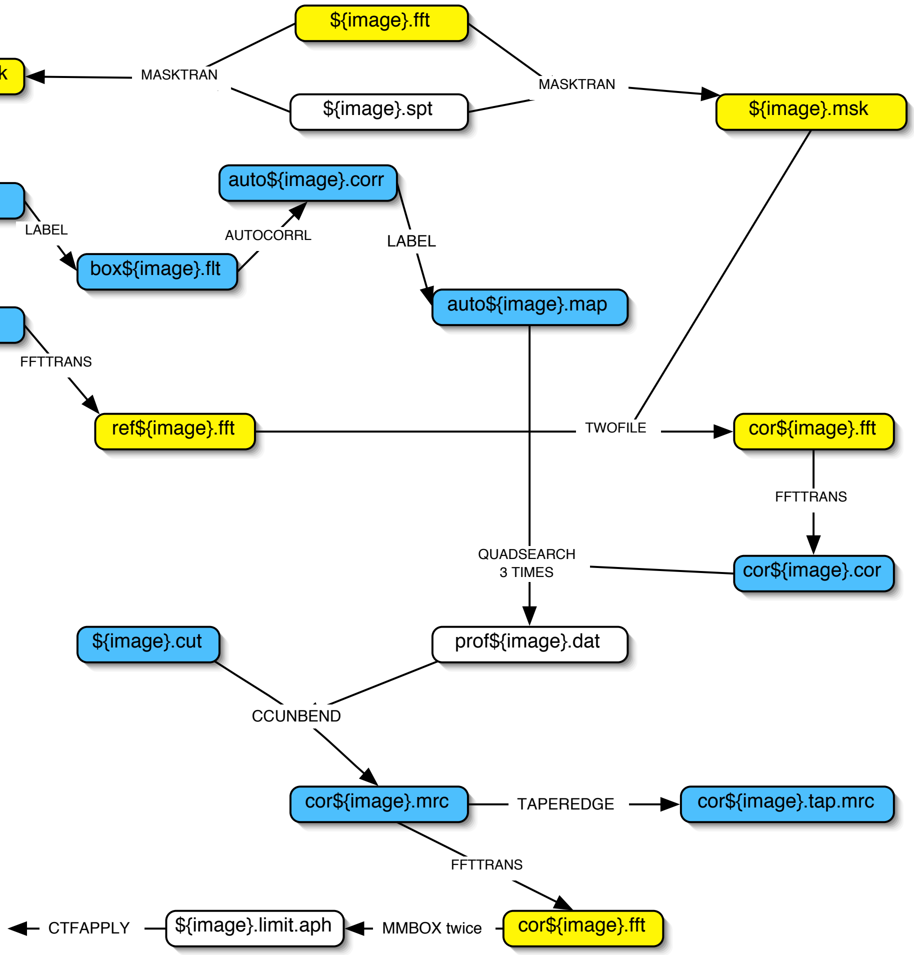
${image}.fft
${image}.ref.msk
MASKTRAN
${image}.spt
MASKTRAN
${image}.msk
FFTRANS
${image}.ref.flt
auto${image}.corr
LABEL
AUTOCORRL
LABEL
BOXIMAGE
box${image}.flt
auto${image}.map
ref${image}.flt
FFTTRANS
ref${image}.fft
TWOFILE
cor${image}.fft
FFTTRANS
QUADSEARCH
3 TIMES
cor${image}.cor
${image}.cut
prof${image}.dat
CCUNBEND
cor${image}.mrc
TAPEREDGE
cor${image}.tap.mrc
FFTTRANS
CTFAPPLY
${image}.limit.aph
MMBOX twice
cor${image}.fft

Figure 2.18: Steps of image processing in the first round of unbending: overview of job2000a. Note that this sequence of steps only aims at generating a better reference for the second round. The output of job2000a is cor${image}.mrc which is used as crosscorrelation reference in 2.19.

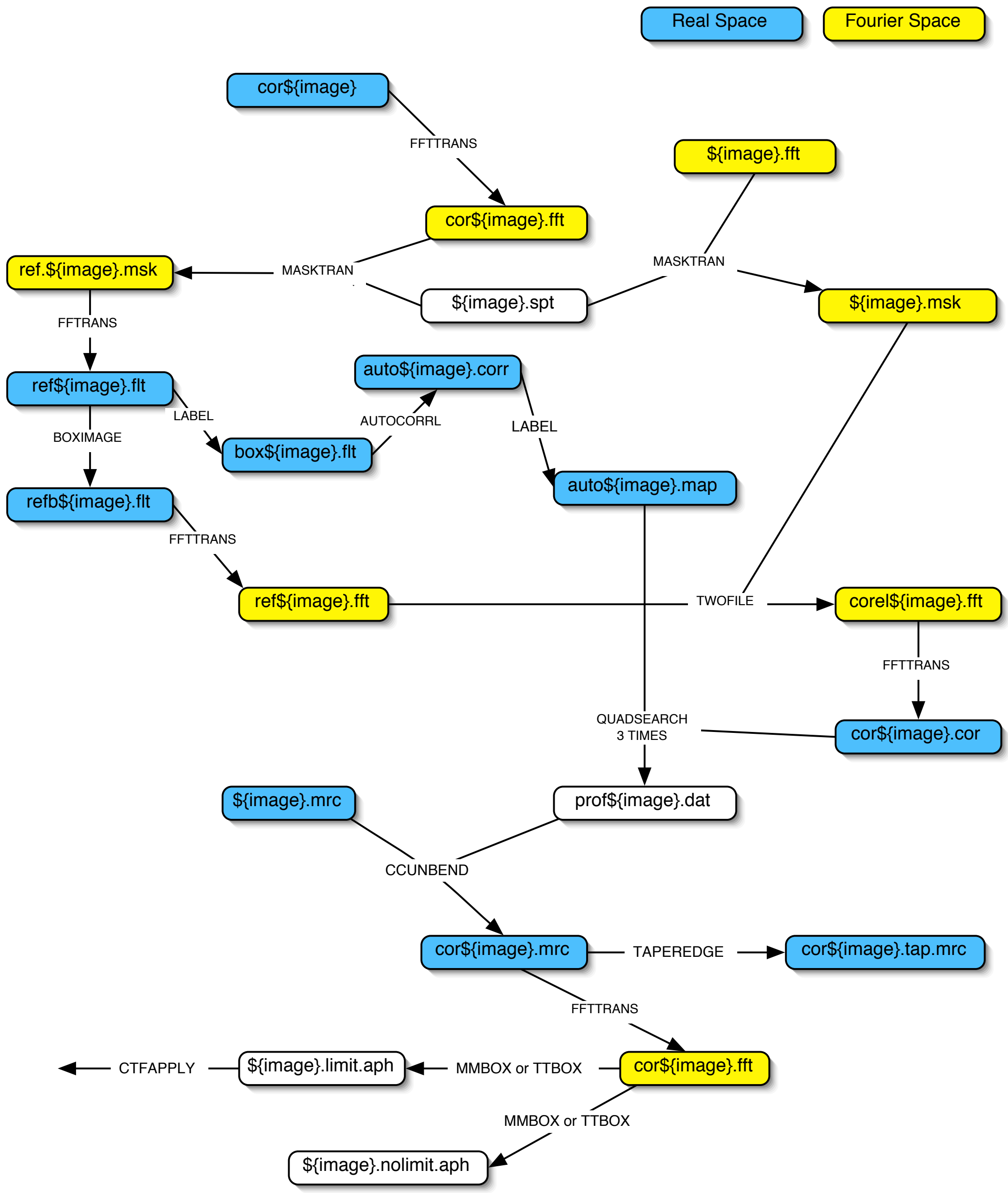
Real Space
Fourier Space
cor${image}
FFTTRANS
${image}.fft
cor${image}.fft
ref.${image}.msk
MASKTRAN
MASKTRAN
${image}.spt
${image}.msk
FFTRANS
ref${image}.flt
auto${image}.corr
LABEL
AUTOCORRL
LABEL
BOXIMAGE
box${image}.flt
auto${image}.map
refb${image}.flt
FFTTRANS
ref${image}.fft
TWOFILE
corel${image}.fft
FFTTRANS
QUADSEARCH
3 TIMES
cor${image}.cor
${image}.mrc
prof${image}.dat
CCUNBEND
cor${image}.mrc
TAPEREDGE
cor${image}.tap.mrc
FFTTRANS
CTFAPPLY
${image}.limit.aph
MMBOX or TTBOX
cor${image}.fft
MMBOX or TTBOX
${image}.nolimit.aph

Figure 2.19: Steps of image processing in the second round of unbending: overview of job2000b. Both job2000a and job2000b are included in `all` which is run twice, the first time for generating an image where low quality crystalline areas are masked, in the second round for the final unbending of the original image.

to make a peak search. Lattice vector length and angle are taken from the merge datafile (created beforehand) and the tilt geometry parameters from the image datafile. A hypothetical lattice is calculated and rotated around the origin of the FFT until the lattice points cover most peaks from the peak search. `mrcdeftilt5 1`: The tilt geometry is re-determined with the lattice parameters. `mrcgetspot` creates the spotlist by searching the fourier transform for peaks from mrcfindlat in 15 px radius from the calculated lattice points.

The first round of `all` creates a mask according to the position of the crystal within the image. The masked image is called m{image}.mrc and it replaces the original image in the second round. Within `all`, two major scripts are run: `job2000a` and `job2000b`. Basically, the same processing happens, but the purpose is different: `job2000a` uses the original image as input and a tightly fourier filtered image as reference. In this job the original image is unbent with the goal to serve as a better reference for the crosscorrelation in `job2000b`. As mentioned before, in the first round of `all` the best part of the crystal is found and the rest is masked. This masked image is processed in the same way in the second round of `all`. Therefore, no unbending in job2000b is made in this first round of `all`. The final crystal unbending for the average map is not done before `job2000b` in the second round of `all`.

`job2000a`: `MASKTRAN` is used to mask the fourier transform of the image according to the spotlist.Two masked images are needed in the first round of unbending: A loosely masked FFT and a tightly masked FFT, which is used as a reference. `MASKTRAN` extracts the hole diameters for the filtering from the datafile. To obtain a fourier filtered image that serves as a reference, the tightly masked FFT is backtransformed using `ffttrans`. From this filtered image, only a small region is cut out by `label` for the reference autocorrelation. `AUTOCORRL` calculates an autocorrelation of the boxed reference region and samples it up to 500x500 pixels. This is done in reciprocal space: the FFT of the boxed reference is oversampled and multiplied with its complex conjugate. Backtransformation results in the autocorrelation map. Beside boxing for creating an autocorrelation peak, the tightly filtered reference image is used for crosscorrelation with the loosely filtered image. Therefore, an area of the reference is boxed using `BOXIMAGE`. Crosscorrelation is done in reciprocal space, therefore `FFTTRANS` calculates the FFT of the reference. `TWOFILE` then calculates the crosscorrelation by multiplying the loosely masked FFT of the image with the complex conjugate of the reference FFT. The output is backtransformed with `FFTTRANS` generating the crosscorrelation map. `QUADSEARCH` searches along the x and y axis of the real space crosscorrelation map for peaks using the autocorrelation peak as reference. The peak positions are saved since they contain the information about the lattice distortions. `QUADSERCH` is run 2 or 3 times, and there is an option to learn and predict peak positions. The real peak is only searched for within a chosen radius around the predicted peak. This radius is set by the parameters KDC and KDR along the x and y axis of the crosscorrelation map. x and y do not refer to the lattice and therefore, if they are badly chosen, the peak of the next unit cell could by mistake be taken for the a strong lattice distortion. The maximum setting for KDC and KDR is 14 px, and this should be less than half a unit cell, otherwise KDR and KDC need to be readjusted. All information is contained in the datafile prof.image.dat which is successively replaced after each round. The output file from quadsearch is used by `CCUNBEND` to unbend the lattice distortions by reinterpolation. Only where the crosscorrelation peak's height reaches a set threshold, the lattice is corrected. For correction, the image is divided into gridsquares of the size of approximately one unit cell and it is determined by what vector the pixels have to be moved to be in register with the reference area. This unbending procedure does not take into account the rotational misalignment of the unit cell, but only the translational misalignment in x and y direction.

`MMBOX` extracts phases and amplitudes of reflections from the unbent image. To correct for the contrast transfer function (CTF), `ctfapply` is run. The resulting .aph file is the final output of a processed image. Merging phases and amplitudes of a 3D data set is done by using `mrcmerge`. If the loopnumber given is 0, phases and amplitudes are averaged by `avramphs` and the given symmetry is imposed when creating a map by `four`. If a loopnumber higher than 0 is given, n rounds of phase origin refinements by `origtiltd.exe` in `mrcmergea` with subsequent averaging of the data by `avramphs` are performed. The phase residuals serve as a parameter for quality control. Images above the user-definded phase residual limit are not further used in the next round of merge. The program `latline` performs fitting of the lattice lines to phases and amplitudes of the reflections in `z*` direction. `four latfitted p4` generates the 3D map with imposed p4 symmetry from sampling the lattice lines and back-transformation.

2.8.5 Phosphorylation and dephosphorylation of 2D crystals of SoPIP2;1

Phosphorylation experiments were done using rat brain Protein Kinase C from Calbiochem and were performed in the isotope laboratory. 25 μl of reaction mixture were prepared as follows: 1.2 mg/ml reconstituted SoPIP2;1 (1 nmol protein), 100 μM $CaCl_2$, 5 mM $MgCl_2$, 20 mM Hepes; pH 7.4 and either 140 μM Phorbol 12,13-dibutyrate (Phorbolester) or 3.8 μM 1,2-Dioctanoyl-sn-glycerol (DAG) or no activator of PKC. To this mixture, 10 μCi γ-^{32}P-ATP, 40 μM cold ATP and 0.06 units of PKC were added. The reaction was performed at 30°C for 20 min before adding 4 mM cold ATP and incubating for another 10 min. The reaction was stopped by adding 172 μl crystallization buffer (20 mM Tris-HCl; pH 8, 50 mM $MgCl_2$, 100 mM NaCl, 2 mM DTT, 0.03% NaN_3) and centrifugation at 10'000 rpm, 20 min. This washing was repeated twice before phosphorylated crystals, controls and supernatants from washes were loaded on SDS-PAGE. The gel was stained, dried on filter paper and exposed during 1-2 days to a Kodak BioMax XAR film for autoradiography.

Dephosphorylation experiments were done using Calf Intestine Alkaline Phosphatase (CIAP) from Calbiochem. 1 μl (33.6 units) of CIAP were added to 20 μl reconstituted SoPIP2;1 (protein concentration 1.5 mg/ml) and incubated at room temperature or 37°for 10 min-2 days. The reaction was performed in crystallization buffer (20 mM Tris-HCl; pH 8, 50 mM $MgCl_2$, 100 mM NaCl, 2 mM DTT, 0.03% NaN_3) or in 50 mM Bicine buffer at pH 9.5, 100 mM NaCl, 10 mM $MgCl_2$, 1 mM $ZnCl_2$, 0.01% NaN_3. Phosphorylation trials of previously dephosphorylated samples were prepared by addition of phosphatase inhibitors (poison mix) containg 10 mM NaF, 10 mM NaN_3, 10 mM p-Nitrophenylphosphate (pNPP), 10 mM β-Glycerophosphate (β-GP), 10 mM Sodium Pyrophosphate ($NaPP_i$).

2.8.6 Mass spectroscopy of reconstituted SoPIP2;1

SoPIP2;1 reconstituted into 2D crystals was proteolytically or chemically digested using various methods, followed by C18 reverse phase chromatography with varying solvents and Electrospray Ionisation Mass Spectroscopy (ESI-MS).

Endoproteinase LysC from Roche was added to reconstituted SoPIP2;1 (concentration 1.1 mg/ml) at a ratio of 1:10 in 30 μl reaction volume and incubated at room temperature for 24 h. Reaction was stopped by pelleting membranes and undigested material at 14'000 rpm, 30 min, 4°C. 2 μl of the supernatant were used to separate peptides on liquid chromatography coupled to ESI-MS. Chemical digestion using CNBr was performed as follows. 1 μg of reconstituted SoPIP2;1 was pelleted and resuspended in 70% formic acid. 1 μg CNBr was added to the dissolved membranes and the reaction was performed overnight at room temperature in the dark. Peptides were separated on a C18 reverse phase chromatography using various B solvents: A = 0.1% triflouroacetic acid (TFA), B = 80% acetonitrile, n-propanol or formic acid, running a gradient from 2 - 75% solvent B in 90 min. Undigested SoPIP2;1 reconstituted into lipid membranes was prepared for MS by dissolving in 70% formic acid followed by addition of the same volume of isopropanol and pelleting of undissolved material. Digestion using proteinase K was basically performed according to [75]: Reconstituted SoPIP2;1 was pelleted and the buffer was exchanged to 200 mM Na_2CO_3; pH 11 to a protein end concentration of 1 mg/ml. The mixture was passed 5 times through a syringe and let stand on ice. Proteinase K was added at a (w/w) ratio of 1:50, the mixture was incubated in a thermomixer at 37°C for 3 h when a second proteinase K aliquot was added and incubated for another 1.5 h. The reaction

Table 2.3: Primers designed for mutating S115 and S274 into alanine and aspartate.

Primer	Sequence
S115AForward	GAC TAT TCC TAG CAA GGA AGG TGG CTT TAC TAA GGG CAC TAG TC
S115AReverse	GAC TAG TGC CCT TAG TAA AGC CAC CTT CTT TGC TAG GAA TAG TC
S274AForward	GCA GCA ATT AAG GCG TTG GGA GCT TTC AGA AGC AAC CC
S274AReverse	GGG TTG CTT CTG AAA GCT CCC AAC GCC TTA ATT GCT GC
S115DForward	GGA CTA TTC CTA GCA AGG AAG GTG GAT TTA CTA AGG GCA CTA GTC
S115DReverse	GAC TAG TGC CCT TAG TAA ATC CAC CTT CCT TGC TAG GAA TAG TCC
S274DForward	GCA GCAC GCA ATT AAG GCG TTG GGA GAT TTC AGA AGC AAC CC
S274DReverse	GGG TTG CTT CTG AAA TCT CCC AAC GCC TTA ATT GCT GCT GC

was stopped by adding formic acid to an end concentration of 5%, centrifugation at 18'000 rpm, 4°C, 15 min. The supernatant was diluted 120 times in 0.1% TFA, centrifuged at 13'500 rpm, room temperature, 10 min, before loading onto the liquid chromatography coupled to MS.

2.8.7 Alanine and aspartate mutants of phosphorylation sites S115 and S274

Cloning and PCR

Point mutations were introduced into the pPICZα vector containing the wildtype SoPIP2;1 gene (kindly provided by Per Kjellbom) using the QuikChange® Site-Directed Mutagenesis Kit from Stratagene. Reverse and forward primers (sequences are displayed in table 2.3) were ordered at Microsynth. The oligonucleotide primers were diluted to an end concentration of 10 μM. PCR was set up for amplification of mutated SoPIP2;1 gene in the pPICZα vector. The optimal PCR mix contained 12 ng of parental DNA, 40 nM of forward and reverse primer, 0.5 μl of dNTP mix to a total reaction volume of 25 μl. PCR was performed under the following conditions: 1 cycle of 30 sec at 95°C , 18 cycles of 30 sec at 95°C, 1 min at 53°C, 10 min at 68°C, and 1 cycle of 7 min at 68°C. For digestion of parental, methylated DNA, DpnI was added and digestion was performed at 37°C, 1h. The PCR product was checked by agarose gel electrophoresis and stored at -20°C.

Transformation of electrocompetent E.coli cells

Electrocompetent *E.coli* cells were prepared following a standard protocol. Briefly, a colony from a LB medium plate was picked and 5 ml liquid low salt LB medium were inoculated and grown overnight. 250 ml liquid low salt LB was inoculated with 2.5 ml overnight culture and grown to an OD_{600}= 0.5. Cells were pelleted at 5'000 rpm, 10 min, 4°C and resuspended in 100 ml ice-cold water twice, pelleted and resuspended in 10 ml 10% glycerol twice, pelleted and resuspended in 200 μl 10% glycerol. Aliquots were quick-frozen in liquid nitrogen and stored at -70°C. For electroporation, 40 μl electrocompetent cells were mixed with 1 μl of 1:5 diluted PCR product in a 0.1 cm electroporation cuvette. Electroporation was performed using a GenePulser apparatus from Bio-Rad according to the provided protocol and settings; charging voltage 1.5 kV, capacitance 25 μF, resistance 200 Ω. 0.5 ml SOC or LB medium was added immediately and transformed cells were incubated for 30 min without shaking plus 1 h on rotational wheel at 37°C for recovery. 50 μl and 450 μl transformed cells were plated evenly on LB plates containing 25 μg/ml Zeocin and grown at 37 °C overnight. Efficiency of transformation was calculated using an online tool on www.sciencegateway.org/tools/transform.htm.

Plasmid isolation, linearization, purification and sequencing

Plasmid isolation from transformed *E.coli* cells grown overnight in liquid low salt LB medium was done using the Qiagen Miniprep Kit or the Qiagen Midiprep Kit, following the provided protocols. The presence of correct mutations was ensured by sequencing isolated DNA (Solvias AG, Basel-CH). Plasmid linearization was achieved by PmeI digestion at 37 °C, 3h and checked by agarose gel electrophoresis. For purification of isolated and linearized DNA, the Qiaquick PCR Purification Kit was used according to the provided protocol. Elution was done in water to avoid high salt concentrations for transformation of electrocompetent *Pichia pastoris* cells.

Transformation of electrocompetent X-33 Pichia pastoris cells

X-33 cells were grown on YPD plates at 30°C for 2 days when colonies were picked and grown in 5 ml YPD liquid medium overnight at 30°C. 250 ml YPD were inoculated with 500 μl of the overnight culture and grown at 30°C to an OD_{600}= 1.6. Cells were pelleted at 2'000 rpm, 4°C, 5 min, resuspended in 125 ml sterile, ice-cold water, pelleted, resuspended a second time in 60 ml sterile, ice-cold water, pelleted, resuspended in 5 ml sterile, ice-cold 1M sorbitol solution, pelleted, resuspend in 0.25 ml sterile, ice-cold 1M sorbitol and kept on ice. 80 μl of electrocompetent cells were added to 5 μl purified DNA in water (DNA concentration approx. 0.5 mg/ml) and transfered to an ice-cold 0.1 cm electroporation cuvette. Electroporation was performed using a GenePulser apparatus from Bio-Rad according to the provided protocol and settings; charging voltage 1.5 kV, capacitance 25 μF, resistance 200 Ω. Immediately after application of one pulse 1 ml of ice-cold, sterile 1M sorbitol was added to the cuvette. Transformants were incubated at 30°C for 2 h of recovery. 200 μl were plated evenly on YPD plates containing 200, 400 and 1000 μg/ml Zeocin and incubated at 30°in the dark for 3 days.

Storage, growth and breakage of Pichia pastoris cells

Glycerol stocks for long term storage were prepared as follows: Best expressing clones were purified by streaking out on YPD plates containing 200 μg/ml Zeocin with an inoculation loop.

Single colonies were picked and grown in 4 ml liquid YPD at 29°C overnight. 0.3 ml of sterile 50% glycerol were added to aliquots of 0.7 ml culture in sterile cryo tubes, the glycerol stocks were quick-frozen in liquid nitrogen and stored at -70°C. To grow cultures for overexpression, BMGY medium was inoculated with the glycerol stock and grown at 29°C and shaking at 180 rpm. After 48h overexpression was induced by exchanging the medium to BMMY and increasing the volume 10 times. To compensate for evaporation and consumption, 0.5% of sterile methanol were added every 24h. Expression in BMMY medium at 29°was kept up for 3 days before cell breakage. Cells from 500 ml culture were pelleted at 2'000 rpm, 5 min and resuspended in 40 ml breaking buffer (50 mM phosphate buffer; pH 7.4, 1 mM EDTA, 5% glycerol, 1 mM Pefabloc or PMSF added shortly before use). Cells were broken using a Bead Beater with a 50 ml chamber half-filled with glass beads, by 7 runs of 30 seconds each and 2 min cooling time in between. The cell lysate was saved, beads washed with 50 ml of breaking buffer. To pellet remaining glass beads, cell lysate and wash were centrifuged at 2'000 rpm, 5 min, 4°C. A second low spin at 9'000 rpm, 10 min, 4°C was done to remove cell walls and unbroken cells. Membranes were pelleted by ultracentrifugation at 150'000 g, 4°C for 2h, resuspended and homogenized in 3 ml breaking buffer, aliquoted, quick-frozen in liquid nitrogen and stored at -70°C.

2.8.8 Purification and 2D crystallization of mutants of SoPIP2;1

To enhance solubilization, peripheral proteins adhering to the membranes were removed by urea/alkaline stripping as described by [92]. Approx. 2.5 ml crude membranes were homogenized in approximately 90 ml 4 M urea, 5 mM Tris-HCl; pH 9.5, 5 mM EDTA, 5 mM EGTA, 0.01% NaN_3, pelleted at 150'000 g, 1h, 4°C, homogenized in 20 mM NaOH, pelleted at 150'000 g, 1h, 4°C, homogenized in 5 mM Tris-HCl, pH 8, 2 mM EDTA, 2 mM EGTA, 100 mM NaCl, centrifuged at 150'000 g, 1h, 4°C and resuspended in 4 ml of 10 mM phosphate buffer; pH 7.8, 50 mM NaCl, 10% glycerol, 0.03% NaN_3. Aliquots of 2 ml were stored at -20°C before solubilization. Membranes solubilized by mixing with 10 mM phosphate buffer; pH 7.8, 12% OG, 10% glycerol, 0.03% NaN_3 to an end concentration of 6% OG and incubation at room temperature for 30 min. Unsolubilized material was pelleted by ultracentrifugation for 40 min at 230'000 g and 4°C. The supernatant was diluted 1:1 with equilibration buffer (10 mM phosphate buffer; pH 7.8, 2% OG, 0.01% NaN_3) to lower the salt concentration before binding to the cation exchange column consisting of CM Sepharose Fast Flow, which was previously washed with approx. 10x bed volume of 1 M NaCl and 10x bed volume of equilibration buffer. Column-bound material was washed with 5-10x bed volume of equilibration buffer and the wash was collected in 1 ml fractions. SoPIP2;1 mutants were eluted with 10 mM phosphate

buffer; pH 7.8, 2% OG, 200 mM NaCl, 0.01% NaN_3. Elution was collected in fractions of 0.5 ml. The elution profile was determined by SDS-PAGE and protein concentration by measuring absorbance at 280 nm. Wild type SoPIP2;1 used for reconstitution into proteoliposomes as described in 2.8.10 was purified according to the same protocol as the mutants.
2D crystals of mutants of SoPIP2;1 could be generally obtained at the same conditions as determined for wild type SoPIP2;1 (see table 2.1). Pure protein was mixed with OG solubilized *E. coli* polar lipid extract at LPRs 0.2 - 0.4 and protein end concentrations of 1-2 mg/ml. Detergent removal was achieved by dialysis in dialysis buttons or using open flow dialysis machine described by [65]. The protein-lipid-detergent ternary mixture was dialyzed against 20 mM Tris-HCl; pH 8, 50 mM $MgCl_2$, 100 mM NaCl, 0.05% NaN_3 for three days, following a temperature profile of 24h room temperature, 24h 37°C and 24h room temperature. Crystal quality was checked by negative stain EM as described above for the wild type.

2.8.9 Electron diffraction

Best-ordered crystal samples were adsorbed to Quantifoil® holey carbon grids for 3 min, blotted and plunge-frozen in liquid ethane using a home-built vitrification device. Electron diffraction patterns were recorded at low electron doses (<5 electrons per $Å^2$) on a Gatan 2Kx2K CCD camera with a Philips CM-200 FEG microscope operated at 200 kV.

2.8.10 Activity assays

All four mutants and wild type SoPIP;2 were reconstituted into proteoliposomes at LPR 30, 60 and 90. Therefore, purified protein was mixed with OG-solubilized *E. coli* polar lipid extract to a protein end concentration of 0.06 mg/ml and an OG end concentration of 4% in an end volume of 10 ml, filled into dialysis tubes with a cut-off of 12 - 14 kDa and dialyzed against 20 mM Tris-HCl; pH 8, 154 mM NaCl, 0.01% NaN_3 for 3 - 5 days. Control vesicles were prepared without protein. Proteoliposomes were filtered using a Minisart 0.2 μm filter unit and checked by negative stain EM. Activity was measured by exposing the proteoliposomes to an inwardly directed 100 mM sucrose gradient in a stopped flow apparatus and following the increase in 90° light scattering. Data from 5 - 10 measurements was averaged, normalized and fitted to single- or double-exponential functions using the program Igor Pro.

2.9 Conclusions

The main interest in structure determination of the plant aquaporin SoPIP2;1 has been - and still is - the gating mechanism. Two main regulative models have been proposed, one involving phosphorylation at two serine residues in the B-loop and at the C-terminus [49], the other being a pH-dependency that implicates a conserved histidine in loop D [50]. To obtain a structural basis for elucidating the sequence of events turning water channel activity either up or down, SoPIP2;1 was 2D crystallized and the structure was determined to a resolution of 5 Å by cryo electron crystallography. Although no clues concerning regulation could be obtained at the given resolution, other specific structural features were found and could be interpreted giving the possibility of an adhesive function beside the known water channel function of SoPIP2;1 (Appendix A): It is thought that the crystal contacts formed between extracellular faces of SoPIP2;1 tetramers are stabilizing double-layered 2D crystals of SoPIP2;1 and are thus recapitulating a native situation in plasmalemmasomes. These invaginations of the plant plasma membrane are formed upon fast volume changes of the plant cells. Other examples for the dual function of aquaporins as water channel and cell adhesion proteins are mammalian AQP0 and AQP4. In both cases, as for SoPIP2;1, 2D crystals of preferentially double-layered character could be obtained and the determined structure allowed identification of structural features involved in the adhesive function [22, 21]. The combination of aquaporin and cell adhesion function is astonishing, yet further experiments will be needed to characterize the possible roles of aquaporin proteins.

While an X-ray crystallographic study attempted to integrate the phosphorylation- and pH-dependent regulation into a model of one comprehensive gating mechanism [61], the remaining open questions were adressed by application of biochemical methods, mass spectroscopy and mutagenesis. First, attempts to phosphorylate and dephosphorylate SoPIP2;1 in the crystal were made but were not successfull in producing sufficient amounts of one phosphorylation state to be used for crystallography. Second, mass spectroscopy was used to determine the phosphorlyation state of heterologously expressed SoPIP2;1. Phosphorylation site S274 was by this means identified as dephosphorylated, but no results could be derived concerning S115. As a final part of this project, overexpression of mutant forms of SoPIP2;1 mimicking phosphorylation and dephosphorylation was required. Aspartate and alanine mutants of both phosphorylation sites could be produced, purified and crystallized. Functional characterization of the mutants is ongoing and preliminary results do only allow the statement that all mutants as well as the wild type exhibit higher rate constants for water transport than control lipid vesicles, but no clear distinction between the activity of individual isoforms can be made at this stage.

This project is thus not concluded yet, but it is in a decisive phase, where no closing answers to the questions posed in the introduction can be given yet. A large step towards clarification is however done, and the structural and functional characterization of the mutants will hopefully elucidate the mechanism of regulation of SoPIP2;1.

Chapter 3

Purification and 2D Crystallization of Heterologously Expressed Human AQP8

Abstract

Human AQP8 was heterologously overexpressed in the methylotrophic yeast *Pichia pastoris* and high amounts could be purified to homogenity suitable for structural studies. In the presented work, AQP8 solubilization and purification was further developed using various detergents. The monodispersity of purified AQP8 was verified by single particle EM, confirming its tetrameric state. When reconstituted in proteoliposomes, the water channel activity of heterologously expressed AQP8 could be demonstrated. Initial 2D crystallization trials resulted in long tubular crystals that were analyzed in preliminary image processing analysis. These results provide a solid basis for future high resolution structural studies of AQP8.

3.1 Introduction

Although AQP8 was discovered already several years ago and a wealth of experimental data has been published since then, the emerging picture about the properties of AQP8 is controversial. AQP8 cDNA has been cloned from human in 1998 [93], after its identification in rat [94, 95] and mouse [96]. It shares about 30 - 35% sequence homology to other aquaporins with highest similary to the plant aquaporin γ-TIP [95]. The amino acid sequence of AQP8 has a long N terminus and a shorter C terminus just like γ-TIP, a structure that is unusual compared with other mammalian aquaporins.

In humans, AQP8 has been found to be a waterselective channel that is neither permeable to urea nor to glycerol [93], whereas urea conductance was reported for mouse AQP8 [96]. In a study using the *Xenopus* oocytes expression assay, NH_3 and NH_4^+ conductivity of several aquaporins was tested and AQP8 as well as AQP3, AQP9 and plant aquaporin TaTIP2;1 were identified as ammonia transporters [38]. Rat AQP8 was found to be abundant in kidney cells where it is localized predominantly in intracellular vesicles [25]. This is also the case in liver, and it could be even demonstrated that AQP8 in cultured hepatocytes can be redirected from intracellular domains to the plasma membrane via a cAMP-dependent mechanism [97]. Additional evidence was found for mitochondrial localization of AQP8 in hepatocytes, suggesting a physiological role of NH_4^+ uptake to supply the urea cycle [27]. Also in many other cell types where AQP8 is present (gastrointestinal tract, respiratory system, testis as well as multiple other glands), its presence appears to be mainly in intracellular vesicles. This localization would suggest that AQP8 is involved in rapid osmoequilibrium between cytoplasmic and vesicular compartments rather than in transcellular water transport [25]. It remains to be determined whether trafficking as described for hepatocytes [97] plays a role in regulation of AQP8 mediated transport and how it occurs. Beside AQP8, the only mammalian aquaporins that were reported to be localized at intracellular sites were AQP6 [26] and AQP12 [34] .

However, functional expression and subcellular localization of AQP8 is still a topic of debate and contradicting views are still being published. Recent reports demonstrate AQP8 expression on the plasma membrane but only weak intracellular expression [98]. Furthermore, recently published results provide evidence against functionally significant expression of AQP8 in rat brain, liver and kidney mitochondria [99]. The physiological role as well as subcellular distribution and characterization of mammalian AQP8 are thus a field with many unanswered questions, pointing at the particularities of AQP8 within the aquaporin family.

Human AQP8 was heterologously overexpressed in the methylotrophic yeast *Pichia pastoris* and purified on Ni-affinity chromatography using a 6xHis-tag, resulting in high amounts of pure protein suitable for 2D crystallization and structural studies (Maria A. Fellert, unpub-

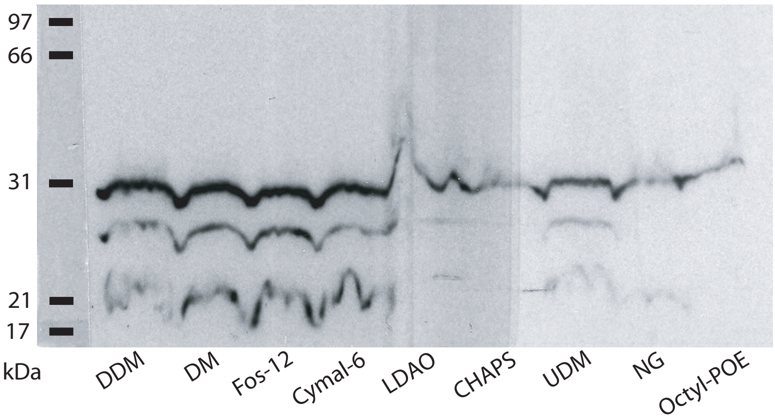

Figure 3.1: In order to find the most suitable detergent to solubilize AQP8, several detergents were used for small-scale solubilization of crude membranes. The used detergents and the concentration at which they were used is given in table 3.1.

lished results). This was the starting point for the presented work.

3.2 Results

3.2.1 Solubilization and stability

A purification of heterologously expressed AQP8 from *Pichia pastoris* membranes was established in the laboratory of P. Kjellbom. The commonly used alkaline/urea stripping protocol to remove membrane-associated protein and thus enhance solubilization [92, 57] resulted in large losses of AQP8, therefore crude membranes are directly solubilized in DDM (Maria A. Fellert, unpublished results). Solubilization is nevertheless efficient and after subsequent affinity purification on Ni-NTA agarose, a fraction of highly pure AQP8 can be obtained. However, screening for other detergents with a possibly higher CMC than that of DDM was required because, having a low CMC, DDM is rather difficult to dialyze for the reconstitution of 2D crystals. Therefore a screen using 8 other detergents for solubilization of a small batch of crude membranes was performed. After 1 hour of incubation, unsolubilized material was pelleted and supernatants containing solubilized protein were checked by Western blot analysis (Fig. 3.1). Compared to DDM, DM, Fos-choline-12 and Cymal-6 turned out to be potential detergents for solubilization of AQP8. LDAO, CHAPS, UDM, NG and Octyl-POE solublize AQP8 to a significantly lower extent. In a further step, the best-solubilizing detergents DDM, DM, Fos-choline-12 and Cymal-6 were used in a parallel purification experiment. To be able to compare the purification efficiency in a quantitative manner, the experiment was started by solublizing all membranes in DDM and loading the same starting material on four columns. Detergent exchange occured thus on the column, when washing and elution of the bound protein was

Table 3.1: Concentrations and CMC of detergents used for solubilization of AQP8

Detergent	CMC	Solubilization conc.
DDM	0.0087 %	2 %
DM	0.087 %	2 %
Fos-choline-12	0.053 %	2 %
Cymal-6	0.028 %	2 %
LDAO	0.046 %	2 %
CHAPS	0.49 %	4 %
UDM	0.029 %	2 %
NG	0.2 %	4 %
Octyl-POE	0.25 %	4 %

performed with the respective detergents in the corresponding buffer. Fractions from all four purifications were loaded on SDS-PAGE to compare purity and efficiency (Fig. 3.2). In all four cases impurities were efficiently washed off from the column in early wash steps (see lanes W3). A major impurity is removed around wash fraction 20, but is still present in the main elution fractions of all four purifications. In the SDS-PAGE of the Fos-choline-12 purification, a weak band around 30 kDa in the wash 20 lane indicates that part of the bound AQP8 is already eluted during washing. Protein concentrations of the respective elution fraction 2 were determined by absorbance measurements: 0.16 mg/ml in 0.04 % DDM, 0.14 mg/ml in 0.4 % DM, 0.13 mg/ml in 0.15 % Cymal-6 and 0.05 mg/ml in 0.3 % Fos-choline-12. To test the stability of AQP8 in these detergents, elution 2 samples of each purification were stored at 4 °and room temperature for 2 days. Potentially aggregated protein was pelleted by ultracentrifugation, and supernatants were loaded on SDS-PAGE. Ultracentrifugation resulted in no visible pellets, indicating that no severe aggregation had occured in any of the tested detergents. The SDS-PAGE showed clear single bands at 30 kDa without degradation or impurities. Due to the differences in the starting protein concentration, however, no further quantitative conclusions can be drawn.

Taking these results together, DM which has a CMC of 0.087 % and can be easily removed by dialysis after 5 days, was decided to be used in following purifications.

3.2.2 Single particles and sample homogenity

Sample homogenity and monodispersity were checked by negative stain electron microscopy of single protein particles. Micrographs were taken at a magnification of 50'000 x, scanned and a top view class average was calculated from 490 boxed particles (Fig. 3.3a) (average calculation by Nora Eifler). The evident fourfold symmetry of the complex confirms its tetrameric nature that is typical for all known aquaporins.

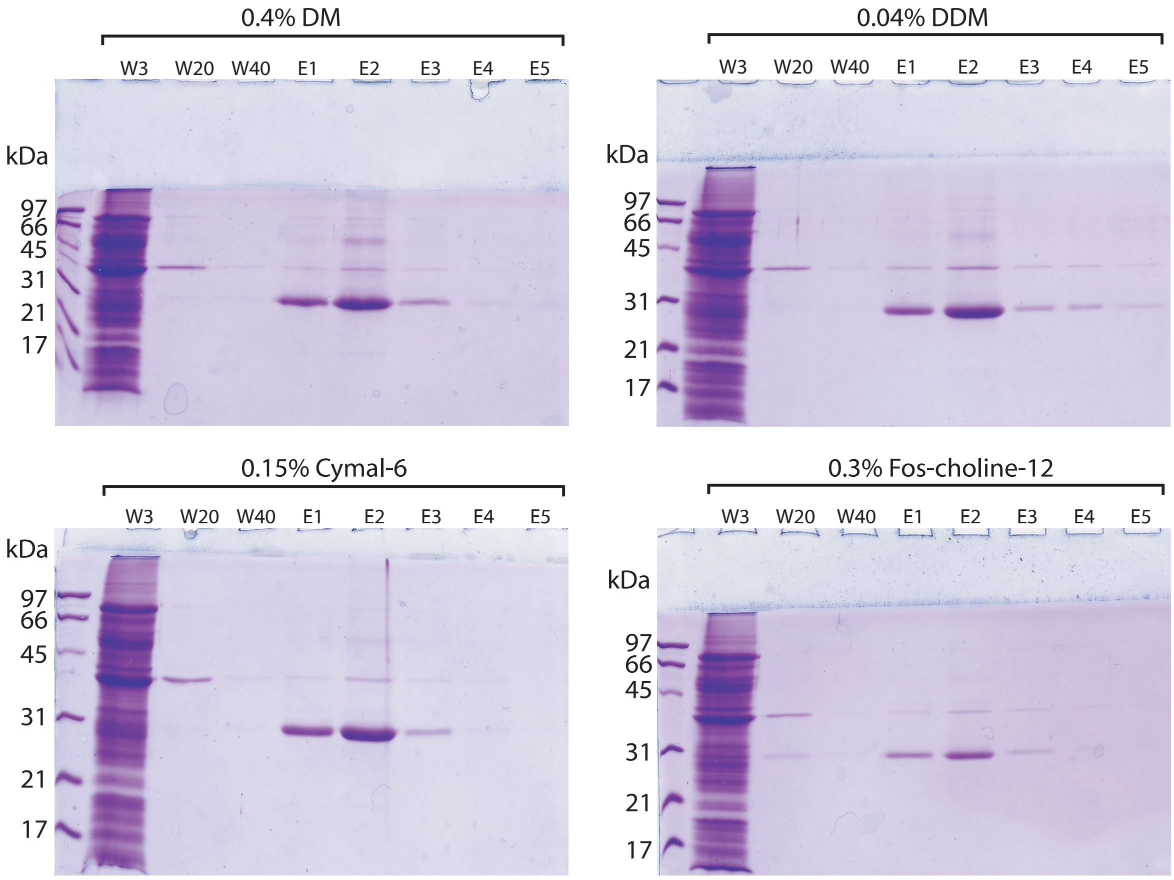
0.4% DM
W3
W20
W40
E1
E2
E3
E4
E5
kDa
97
66
45
31
21
17
0.04% DDM
W3
W20
W40
E1
E2
E3
E4
E5
kDa
97
66
45
31
21
17
0.15% Cymal-6
W3
W20
W40
E1
E2
E3
E4
E5
kDa
97
66
45
31
21
17
0.3% Fos-choline-12
W3
W20
W40
E1
E2
E3
E4
E5
kDa
97
66
45
31
21
17

Figure 3.2: The three best solubilizing detergents from the experiment shown in Fig. 3.1 were tested in parallel purifications after solubilization in DDM, for comparison with DDM. Wash fractions W3, W20, W40 and elution fractions E1 - E5 were checked by SDS-PAGE.

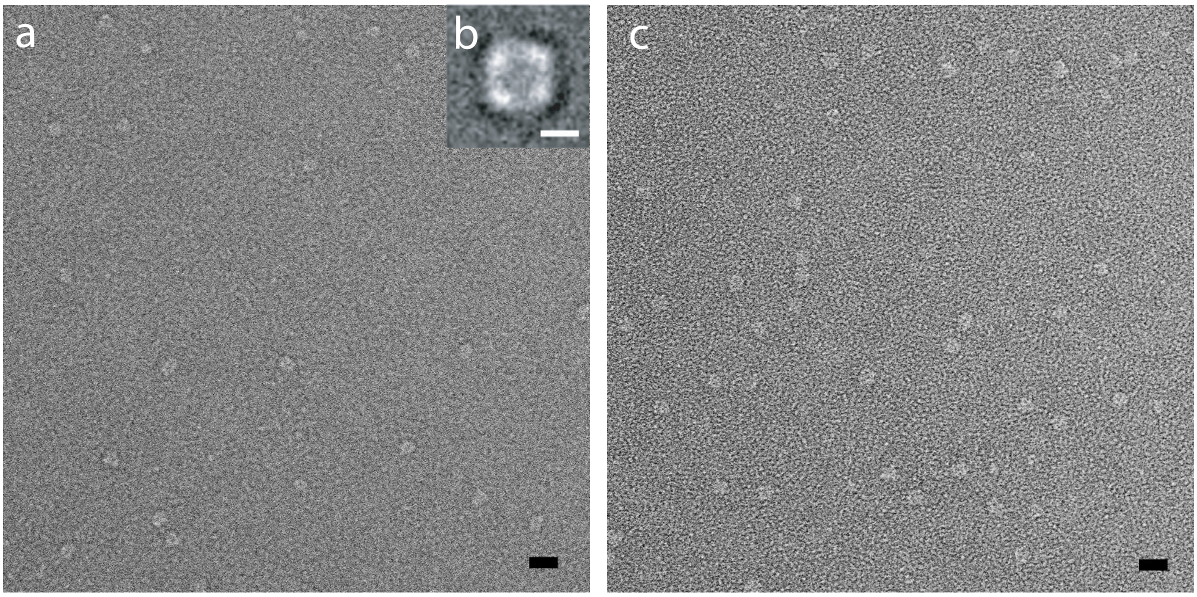

Figure 3.3: Single particles of AQP8 imaged in negative stain. a) Purified in DDM and c) Purified in DM. The inset b) shows a top view class average comprising 490 DDM purified particles. Scale bars correspond to 20 nm in a) and c) and 5 nm in inset b).

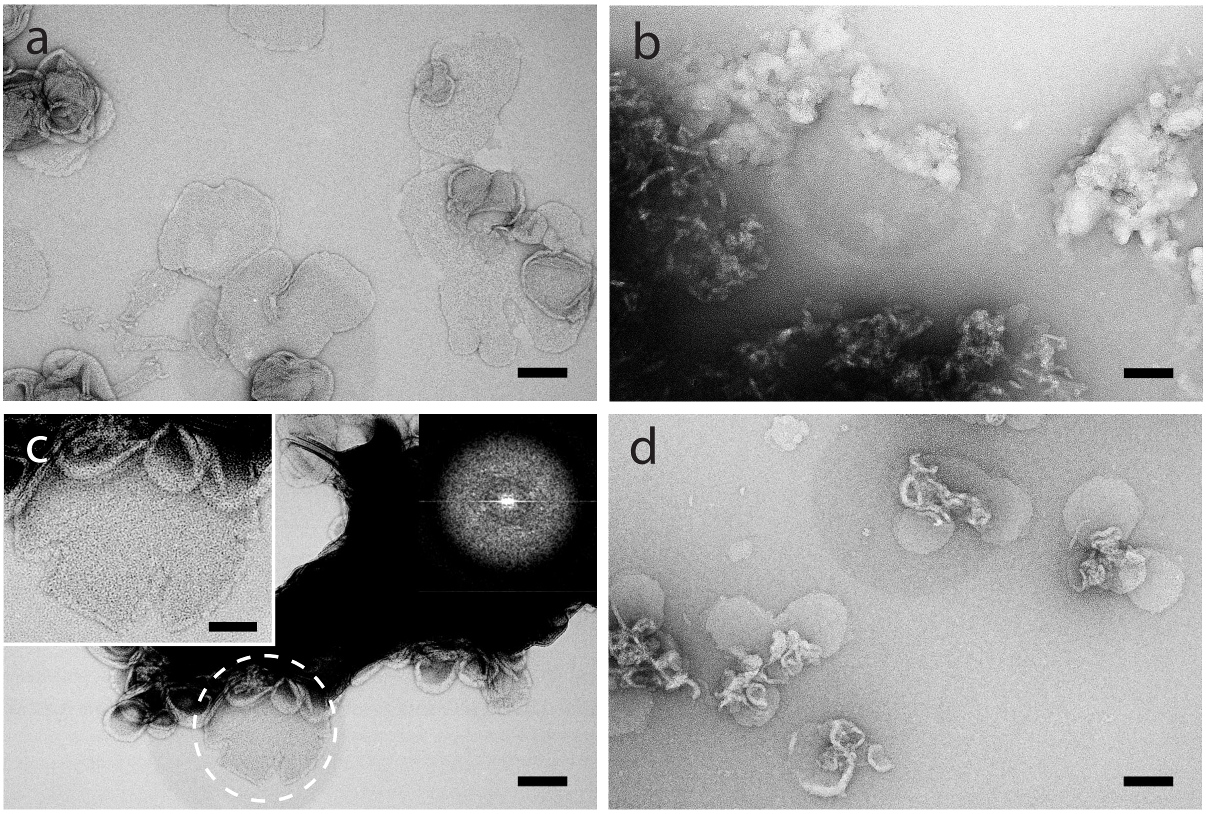

Figure 3.4: Examples of crystallization trials using different lipids. a) *E. coli* polar lipids, LPR 0.7, pH 6 with 5 mM $MgCl_2$. b) DMPC lipids, LPR 0.2, pH 8 with 10% glycerol. c) POPS lipids LPR 0.5 pH 7 with 5 mM $MgCl_2$. Left inset: Enlarged crystalline region of the dashed circle. Right inset: Powerspectrum of the dashed circle. d) POPS:POPC=3:7 mixture at LPR 0.5, pH 7. Scale bars are 100 nm (a, b, c, d) and 50 nm (left inset in c).

3.2.3 Screening for 2D crystallization conditions

2D crystallization trials were set up mainly in dialysis buttons, although few trials were made using MBCD to remove the detergent (see Appendix B) and the monolayer technique [100]. The latter two methods yielded only aggregates and were therefore not used for further trials. A table of the conditions that were screened in buttons is given in table 3.2. In initial attempts, *E. coli* polar lipid extract, which was successfully used for several other aquaporins, resulted in vesicles and small lipid sheets that did however not exhibit any crystallinity (Fig. 3.4a). DMPC, which is a commonly used synthetic lipid for 2D crystallization, gave aggregates and was therefore not further used (Fig. 3.4b). Reconstitution in POPS, a phophatidylserine lipid which is positively charged at pH 7, resulted in small (100 nm in diameter) crystalline arrays (Fig. 3.4c) which were promising and thus considered in further experiments. When reconstitution was done in a mixture of POPS with the neutral phosphatidylcholine POPC at a ratio of 3:7, AQP8 formed 2D crystals of long and narrow tubular shape (Fig. 3.5). However, these crystals were only found when the protein concentration in the crystallization trials was raised to approximately 2 mg/ml, and the samples were not homogenous, consisting to about

Table 3.2: Conditions screened for 2D crystallization of AQP8

Parameter	Screened	Best results
Lipids	*E. coli*, soy, liver, brain lipids, DMPC, DOPS POPS, DOPS:DOPC (3:7), POPS:POPC(3:7 and 7:3)	POPS:POPC (3:7)
LPR	0.2 - 1.3	0.3
Protein concentration	0.5 - 2 mg/ml	2 mg/ml
pH	5, 6, 7, 8, 9	7
Buffer	Citrate, MES, Hepes, Tris, Bicine	Hepes
NaCl	50 - 500 mM	100 mM
$MgCl_2$	0, 5, 20 mM	5 mM
Additives	+/- 10 % glycerol	–

70 % of round-shaped vesicles that did not exhibit any crystallinity (Fig. 3.5a). $MgCl_2$ turned out to be crucial for successfull reconstitution as known for most other aquaporins, yet not above a concentration of 5 mM, which is also typical for His-tagged proteins as they tend to aggregate at higher $MgCl_2$ concentrations. Monovalent salt NaCl was used at various concentrations (50 - 500 mM), but no apparent differences dependent on NaCl concentration were observed. The same counts for the use of glycerol in the dialysis buffer, which seems to have no influence either.

3.2.4 Preliminary image processing

Electron micrographs of crystalline tubes were scanned and analyzed using the image processing package SEMPER in order to assess lattice properties and the crystallographic symmetry. Fourier-peak filtering and subsequent correlation averaging of unit cells gives a first glimpse on AQP8 tetramers in the 2D crystal. Lattice constants are a = b = 100 Å, $\gamma = 90°$, indicating that the unit cell comprises two AQP8 tetramers (Fig. 3.5e and f).

3.2.5 Water channel activity

To test whether heterologously expressed AQP8 is active, the protein was purified and reconstituted into proteoliposomes. In the literature, the most common lipid used for reconstitution of aquaporin water channels as well as other membrane proteins for activity assays is *E. coli* polar lipid extract [77, 57, 90]. In the case of AQP8 purified in DM, it was not possible to obtain vesicles with reconstituted protein. Moreover, the production of empty vesicles from DM-solublized *E. coli* polar lipids was not reproducible (M. Fellert, unpublished results). Since a POPS/POPC lipids mixture at 3:7 ratio was successfully used in initial crystallization trials, it was also applied for reconstitution into proteoliposomes at LPRs of 10 to 90. After removal of DM by dialysis during 7 days, the obtained vesicles were imaged by negative stain EM. In Figure 3.6, proteoliposomes at LPRs 10, 30, 60, 90 as well as control vesicles without protein

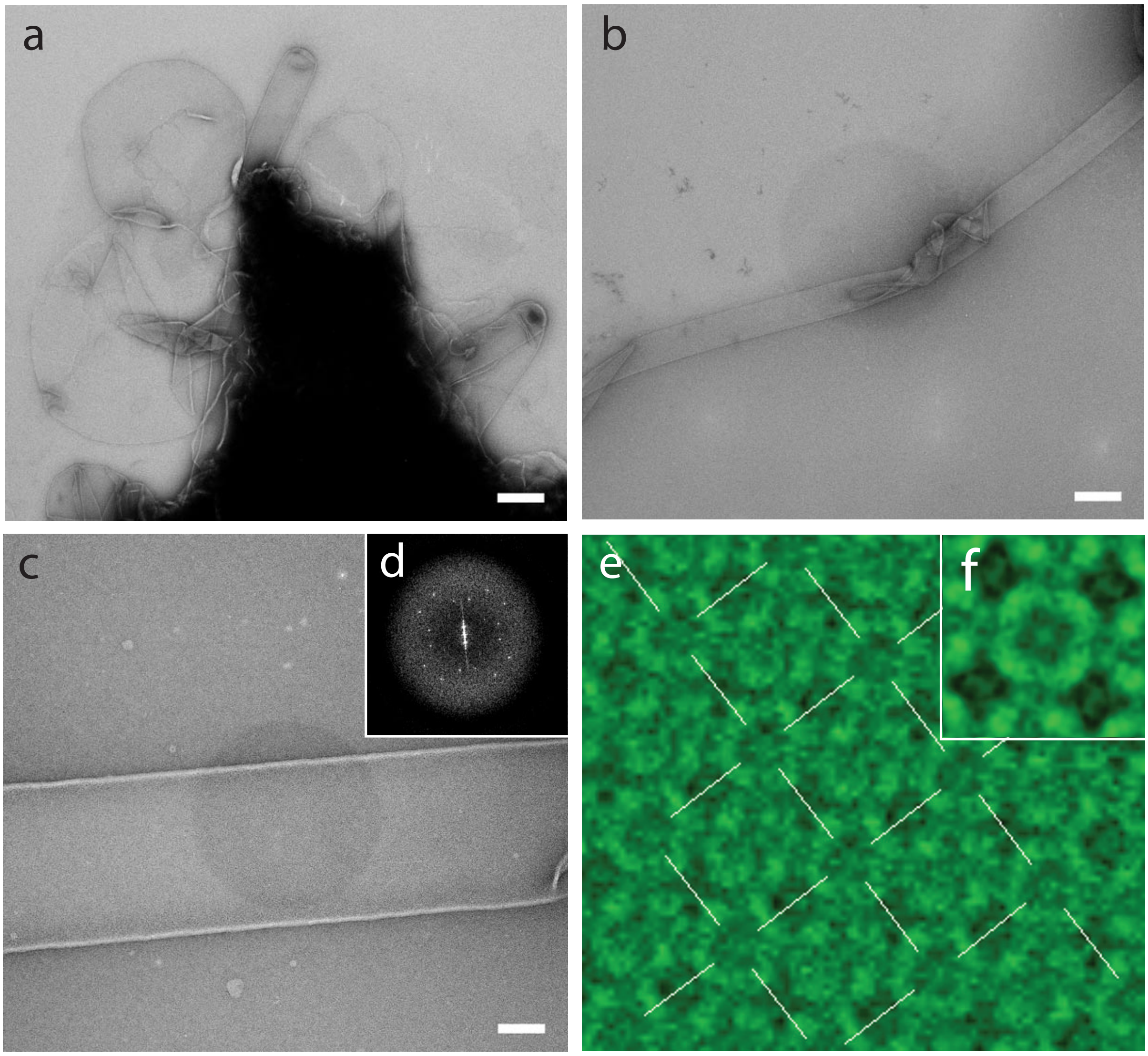

Figure 3.5: Tubular 2D crystals of AQP8. a) and b) Overviews taken at a magnification of 10'000x. c) A tube imaged at a magnification of 50'000x. A calculated power spectrum of the tube shown in c) is depicted in the inset d). e) Correlation averaging of a crystalline tube as shown in c). The lattice is shown by the overlay. Lattice constants are: a = b = 100 Å, $\gamma = 90°$. f) Four-fold symmetrization was applied on one tetramer. Scale bars are: 500 nm (a and b), 100 nm (c).

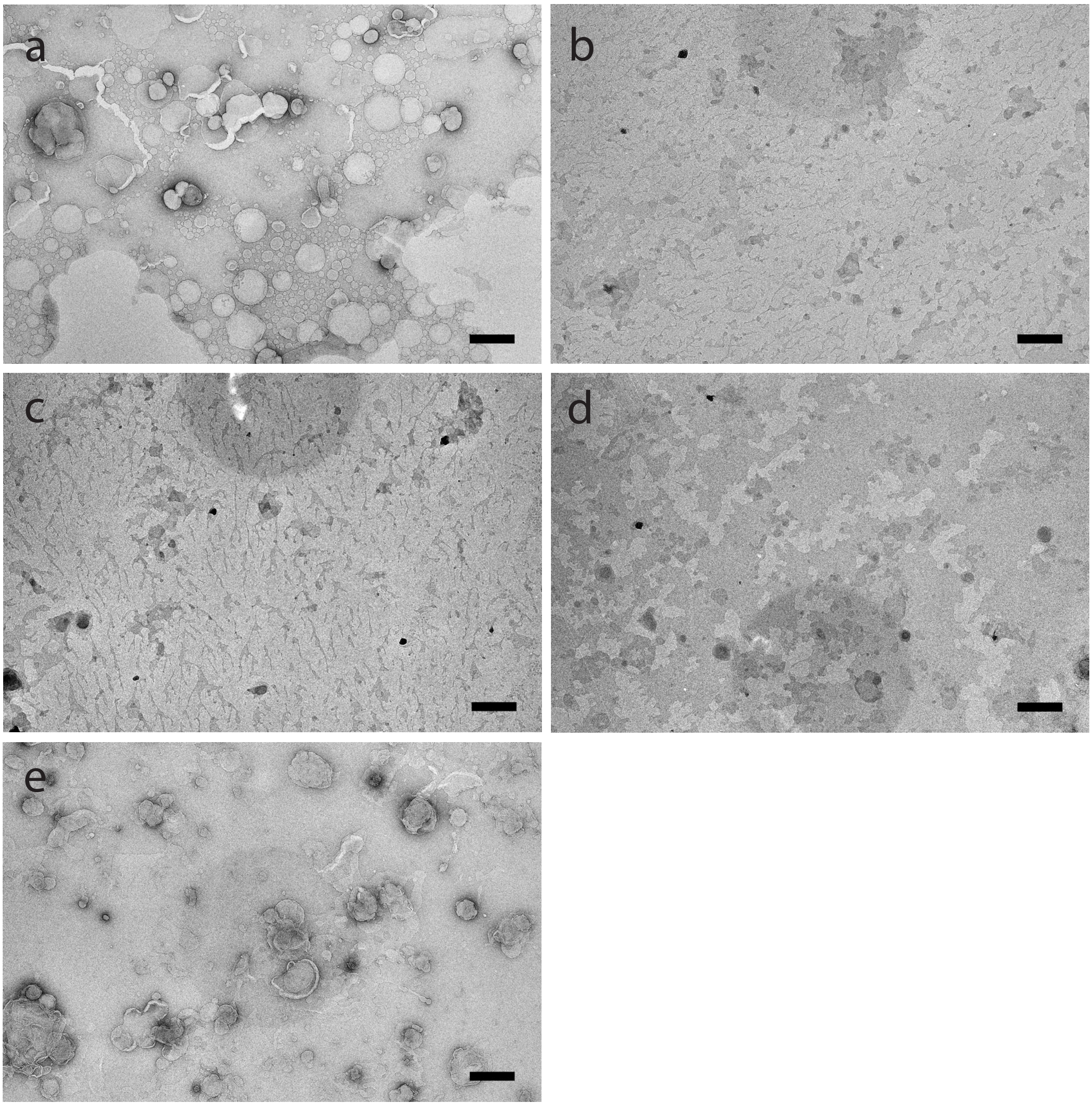

Figure 3.6: Control POPS/POPC liposomes (a) and proteoliposomes containing AQP8 at LPRs 10 (b), 30 (c), 60 (d) and 90 (e) imaged by negative stain EM. Scale bars: 500 nm.

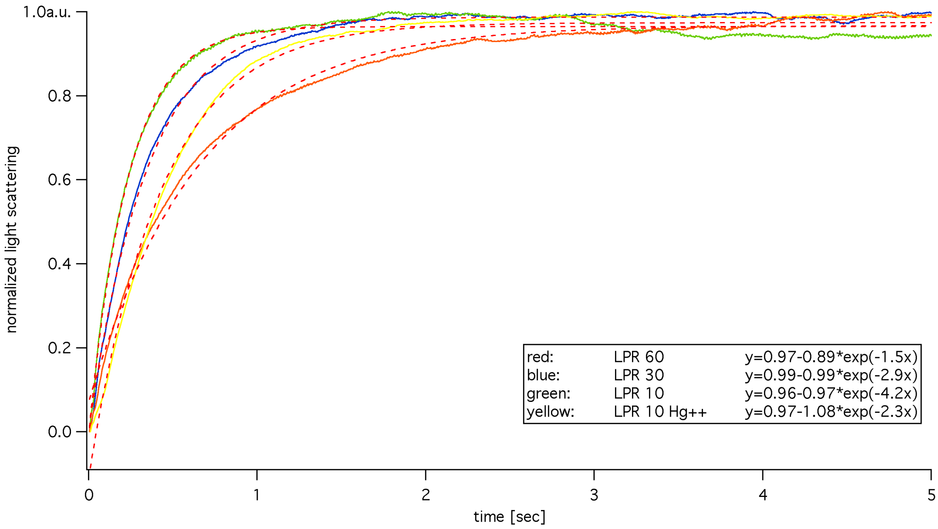

Figure 3.7: Water transport activity of AQP8 monitored by 90° light scattering in a stopped flow apparatus. When proteoliposomes are exposed to an osmotic shock, light scattering increases due to the shrinkage of the proteoliposomes. The rate of shrinkage decreases at higher LPRs, proving that water transport activity is dependent on the number of AQP8 molecules per proteoliposome. When proteoliposomes of LPR 10 were incubated with Hg^{++} prior to the osmotic shock (yellow trace), shrinkage was considerably slower than for untreated proteoliposomes at LPR 10 (green trace). Normalized and averaged time-courses were fitted to single exponential equations given in the figure legend.

are shown. Control vesicles exhibit spherical shape (Fig. 3.6a), but at LPRs 10 and 30, the proteoliposomes are rather elongated, branched structures (b and c). At LPR 60, the proteoliposomes become more round-shaped again (d), while at LPR 90 they resemble even more the spherical control vesicles (e).

Water channel activity was measured by exposing proteoliposomes to an osmotic shock and following the increase in 90° light scattering due to vesicle shrinkage. The time course of shrinking depends on the LPR as illustrated by the normalized and averaged traces of the particular experiments in Fig. 3.7. Thus at higher amounts of protein relative to lipid, the change of vesicle shape due to water efflux is faster. In contrast to activity measurements reported in the literature that were done with *E. coli* polar lipids, no significant increase of 90° light scattering was observed for the control POPS/POPC vesicles. Therefore the empty vesicles data was not processed and is not displayed in Fig. 3.7.

Normalized and averaged traces of the individual experiments were fitted to single exponential equations of the form $y = y_0 - Ae^{-kx}$, with k being the rate constant of the first order kinetic reaction (see also 2.4). Calculated rate constants are: 4.2 s^{-1} at LPR 10, 2.9 s^{-1} at LPR 30, 1.5 s^{-1} at LPR 60. When proteoliposomes at LPR 10 were blocked with mercury, the rate constant decreased to 2.3 s^{-1}.

Table 3.3: 2D Crystallization conditions of aquaporins crystallized to date

Protein	Conditions	
AQP0 [22]	Detergent	DM
	Lipids	DMPC
	Buffer	10mM Mes; pH 6, 50 mM $MgCl_2$, 150 mM NaCl, 5 mM DTT, 0.02 % NaN_3
	Method	Dialysis buttons
AQP1 [101]	Detergent	OG
	Lipids	E.coli lipids
	LPR	0.5
	Buffer	20 mM Tris-HCl; pH 6, 250 mM NaCl, 1 mM DTT, 1 mM NaN_3, +/- 10/100 mM Mg^{++} or Ca^{++}
	Method	Dialysis machine
AQP2 [20]	Detergent	OG
6xHis-tag	Lipids	E.coli or Heart polar lipids
	LPR	0.5
	Buffer	20 mM Mes; pH 6, 100 mM NaCl, 5 mM $MgCl_2$ or $MgSO_4$, 5 mM Histidine
	Method	Dialysis machine
AQP4 [21]	Detergent	OG
6xHis-tag	Lipids	E.coli total extract
	LPR	1
	Buffer	10 mM Mes; pH 6, 100 mM NaCl, 50 mM $MgCl_2$, 2 mM DTT, 10% glycerol
	Method	Dialysis buttons
AQPZ [102]	Detergent	OG
10xHis-tag	Lipids	POPC:DMPC (1:1)
	LPR	0.3 - 2
	Buffer	20 mM Citrate; pH 6, 200 mM NaCl, 100 mM $MgCl_2$, 3 mM NaN_3, 10% glycerol
	Method	Dialysis buttons and Eppendorf tube caps
GlpF [103]	Detergent	OG
10xHis-tag	Lipids	E.coli lipids
	LPR	0.6 - 1.4
	Buffer	10 mM Tricine; pH 8, 100 mM NaCl, 5 mM $MgCl_2$, 10 mM DTT
	Method	Dialysis machine
α-TIP [104]	Detergent	DHPC (lipids in DM)
	Lipids	Soybean phosphatidylcholine
	Buffer	25 mM TEA; pH 7.5, 100 mM NaCl, 3 mM NaN_3, 1 mM DTT
		0.1 mM Butylated hydroxytoluene, 0.1 mM EDTA
SoPIP2;1 (App. A)	Detergent	OG
	Lipids	E. coli polar lipid extract
	LPR	0.3-0.4
	Buffer	20 mM Tris; pH 8, 100 mM NaCl, 50 mM $MgCl_2$, 2 mM DTT, 0.03 % NaN_3
	Method	Dialysis machine

3.3 Discussion

3.3.1 Purification

Although a purification protocol using DDM has already been established before, solubilization expriments screening for other detergents were performed to find a detergent with higher CMC in order to be able to use dialysis as method of choice for 2D crystallization. It was found that beside DDM DM, Cymal-6 and Fos-Choline-12 are equally well solubilizing AQP8 from *Pichia pastoris* crude membranes. It is surprising that UDM, which is similar to DM and DDM, solubilizes so poorly compared to the latter ones (Fig. 3.1). While DM has 10 and DDM 12 carbon atoms in its hydrophobic tail, UDM differs in having 11 C-atoms. In nature, lipids and other amphiphiles occur with even chain length, which might indicate why UDM with its uneven number of C atoms does not solubilize as well as DM and DDM.

A well-solubilizing detergent is not necessarily good for protein purification and for keeping the protein stable until it is reconstituted into the lipid bilayer. Therefore parallel purifications of DDM-solubilized material were performed using DM, Cymal-6 and Fos-Choline-12 in wash and elution buffers. Apart from Fos-Choline-12 which gave a poor yield, DM and Cymal-6 are efficient alternatives to DDM. Moreover, although the contaminating band at approximately 40 kDa is present in all purifications, it seems to be slightly weaker in DM and in Cymal-6 compared to DDM. AQP8 is stable without significant aggregation in DDM, DM, Fos-choline-12 and Cymal-6 at 4°C as well as room temperature for at least 2 days as indicated by ultracentrifugation and SDS-PAGE. The monodispersity of AQP8 in DM was verified by single particle EM and was found to be equally good as in DDM. As DM is a common detergent for solubilization and purification of membrane proteins, it was decided to be used in following experiments.

3.3.2 2D crystallization

Most common crystallization conditions that have proved to be successfull in crystallizing other aquaporins (table 3.3) were tested for AQP8. In particular, conditions with varying lipids, pH and $MgCl_2$ as additive were screened. 2D crystals of AQP8 have so far only been obtained using a mixture of lipids consisting of 70 % POPC, which is neutral at the given pH 7 and 30% POPS, carrying a positive charge at pH 7. Mg^{++}, which is known to promote formation of 2D crystals in many cases (table 3.3), turned out to be crucial also in the case of AQP8. It could, however, only be added at concentrations up to 5 mM $MgCl_2$, since His-tagged AQP8 aggregates at higher Mg^{++} concentrations (see also discussion in 2.5.1). The crystals appear as long, narrow tubes (Fig. 3.5), similar to the tubular crystals formed by His-tagged SoPIP2;1 (Fig. 2.1). In the case of SoPIP2;1, highly ordered crystalline sheets could only be observed in the presence of 50 mM $MgCl_2$ for untagged SoPIP2;1. It could therefore be necessary to remove the His-tag of AQP8 to obtain crystalline sheets of high quality. On the other hand, several His-tagged aquaporins were reported to reconstitute into highly ordered 2D crystals at low $MgCl_2$ concentrations.

AQP8 crystals (shown in Fig. 3.5) make up only about 30% of the sample, the rest being non-crystalline round-shaped vesicles. Due to this inhomogenity of the sample and to the very narrow diameter of crystalline tubes the quality of these crystals cannot be assessed by electron diffraction as done for SoPIP2;1 (chapter 2).

To improve the crystals, the screening has to be continued. For instance, other synthetic lipid mixtures at different ratios can be tried. Also, the influence of monovalent salts such as NaCl or KCl can be re-screened in combination with a good lipid. In the case of His-tagged SoPIP2;1 in *E. coli* lipids, the NaCl concentration was inducing different crystals forms (see table 2.1). As an option to change kinetics of the reconstitution, purification can be done in

Cymal-6 instead of DM and reconstitution in Cymal-6-solubilized lipids.

The knowledge of crystallization conditions for homologous aquaporins was helpful, since some parameters such as the effect of MgCl, the pH and buffer substance, could be derived from known conditions. However, 2D crystallization is still an empiric field, and to make quantitative predictions of crystallization conditions is almost impossible. With AQP8, for example, we have observed how critical the choice of lipid is, as approved lipids failed to produce crystals and new lipid mixtures yielded much better results.

Recently, the structure of AQP4 which is the predominant water channel in mammalian brain, was determined by electron crystallography [21]. Like AQP8, it has an unusually long N-terminus compared to other mammalian aquaporins and exists in two alternative splicing isoforms of which one starts at Met23. Interestingly, only the shorter version formed highly ordered 2D crystals, while full-length AQP4 did not crystallize. Furthermore, the addition of a synthetic peptide consisting of the first 22 residues of AQP4 destroyed the order of AQP4M23 crystals. It was found that conserved residue Arg9 was responsible for destabilization of orthogonal arrays. Although the N-terminal sequence of hAQP8 does not contain any methionine indicating an alternative splicing version, the unusual length of the N-terminus and the presence of residue Arg13, which might correspond to Arg9 in AQP4, could have an influence on the formation of 2D crystals. It could therefore be worth considering crystallization of a truncated version.

3.3.3 Water channel activity

Purified AQP8 was reconstituted into POPC/POPS lipids at LPRs varying between 10 and 90, while control vesicles did not contain any protein. Taking into account that crystallization trials were only successful using the POPS/POPC lipid mixture but not in *E. coli* polar lipids, it is not surprising that reconstitution into proteoliposomes using *E. coli* polar lipids did not succeed, even though *E.coli* polar lipids were used for testing aquaporin water transport activity in many cases reported in the literature [77, 57, 90]. It is however astonishing that even empty vesicles could not be obtained by dialysis during 7 days using *E. coli* polar lipids solubilized in 1% DM, which is the same amount of detergent as used for solubilization of the POPS/POPC mixture. In one trial, vesicles were observed by negative stain EM after 2 weeks of dialysis. This unexpected behaviour of the DM-*E. coli* polar lipids system is difficult to explain. In the cases of other aquaporins that were reconstituted into *E. coli* polar lipids, both protein and lipids were solubilized in other detergents than DM.

The activity of reconstituted AQP8 was assessed by measuring the increase in 90° light scattering after exposing proteoliposomes to an osmotic shock. The rate constants determined for the individual experiments reflect the dependency on the number of water channels relative to lipid. Yet they are significantly lower than rate constants measured for other aquaporins. For example, AQP1 at LPR 10 gives a rate constant of 50.4 s^{-1}, while the rate constant of control vesicles is 3.9 s^{-1} [76]. AQP2 exhibits rate constants of 18.8 s^{-1} (LPR 60) and 13.1 (LPR 90), as calculated by substracting rate constants of Hg^{++} treated vesicles from untreated [77]. For SoPIP2;1, the rate constant calculated at LPR 30 is 16 s^{-1}, 9.9 s^{-1} at LPR 90 and 4.8 s^{-1} for control vesicles [57]. In these examples, the control vesicles containing no protein exhibit higher rate constants (i. e., 3.9 s^{-1}, 4.8 s^{-1}) than proteoliposomes of AQP8 (Fig. 3.7). Yet the observed signal must be due to the water transport activity of AQP8, since clear differences between the LPRs can be observed. The fact that control vesicles of POPS/POPC did not give any signal increase when exposed to the osmotic shock suggests that the intrinsic water permeability of the bilayer formed by POPS/POPC can be considered as very low compared to other lipids, which might also explain why the rate constant of AQP8 proteoliposomes is lower than the rate constant of control vesicles in other systems. Importantly, it has to be considered that the shape and size of proteoliposomes shown in Fig. 3.6 is far from spherical, thus they have a small volume compared to their surface, meaning that water efflux can induce only small changes in volume and shape. This might have an influence on the rate constant of water transport, too. Incubation with Hg^{++} does not completely inhibit water channel activity, the rate constant of inhibited proteoliposomes at LPR 10 is 2.3 s^{-1}, which is about half of untreated LPR 10. The cysteine which corresponds to the inhibitory site Cys189 in AQP1 [8] and is therefore thought to be responsible for inhibition by mercurials is located at the C-terminal end of helix 5 / loop E, meaning that only those AQP8 channels oriented with their extracellular faces towards outside of the proteoliposomes can be blocked by Hg^{++}. A blocking rate of 50 % could be therefore attributed to random orientation of AQP8 tetramers within the bilayer. On the other hand, 50 % blocking could reveal that only half of the water transport measured is mediated by AQP8, while the rest is due to leakiness of the lipid bilayer which is modulated by protein insertion. This hypothesis is supported by the fact that the shape of proteoliposomes depends very much on the amount of inserted protein (Fig. 3.6).

It cannot be ruled out that the low rate constant is a consequence of incomplete reconstitution, partial aggregation or not proper folding of the protein. But since AQP8 is rather exceptional in its localization and its substrate specificity which is still not be clarified, the poor water transport activity might be an intrinsic property of AQP8.

3.4 Materials and Methods

3.4.1 Solubilization and purification

Crude *Pichia pastoris* membranes were diluted to a total protein concentration of 24 mg/ml in buffer B (20 mM Hepes-NaOH, 300 mM NaCl, 2 mM β-Mercaptoethanol, 10 % (v/v) glycerol, 0.03 % NaN_3) and solubilized by dropwise addition of detergent solution (4 % DDM or 6 % DM in buffer B to a final concentration of 2 % DDM or 3 % DM, respectively) to a final total protein contentration of 12 mg/ml while mixing with a magnetic stirrer. The solution was stirred for another 1h at room temperature before pelleting unsolubilized material by centrifugation at 150'000 g, 4°C, 30 min. 10 mM imidazole were added to the solublized protein to minimize unspecific binding. Ni-NTA agarose (approx. 1 ml bed volume per 60 mg of total protein in crude membranes) was equilibrated by washing 5 x with twice the bed volume of buffer B with 0.04 % DDM and 0.4 % DM, respectively. For binding, the Ni-NTA-protein slurry was incubated overnight on a rocking table at 4°C. The next day the slurry was divided onto 3 PolyPrep columns (BioRad) and flowthrough was collected and passed a second time over the column to increase binding. Columns were washed with 40 times bed volume of buffer B with detergent and 70 mM imidazole. Wash fractions 3, 20 and 40 were saved for SDS-PAGE. The protein was eluted with 300 mM imidazole in buffer B with detergent. Elution 1 from the first column was poured on the second column to elute and then on the third column, same was done with the following elutions. Thus elutions 1 from all three columns were concentrated in one fraction and so on. Protein concentration was determined by measuring absorbance at 280 nm (ε_{280nm} = 42970 $M^{-1}cm^{-1}$, MW = 29934.9 Da), purity and homogenity were checked by SDS-PAGE and single particle electron microscopy.

3.4.2 Detergent screen and stability

For detergent screening, small scale solubilization was done using different detergents in parallel, detergent solutions in buffer B were added to end detergent concentrations of 2 % DDM, 4 % DM, 2 % Fos-choline-12, 2 % Cymal-6, 2 % LDAO, 4 % CHAPS, 2 % UDM, 4 % NG, 4 % Octyl-POE. Membrane-detergent mixtures were incubated in Falcon tubes on a rocking table for 1h at room temperature followed by ultracentrifugation at 150'000 g, 4°C, 30 min. Supernatants were loaded on SDS-PAGE for Western Blot Analysis for comparison of the solubilization efficiencies. For parallel purification in 4 best-solubilizing detergents, crude membranes were solublized in DDM as described above, split onto 4 columns and purified according to the protocol described above but with the following detergent concentrations in Ni-NTA equilibration, wash and elution buffers: 0.4 % DM, 0.04 % DDM, 0.15 % Cymal-6 and

0.3 % Fos-choline-12. Purity was checked by SDS-PAGE and concentrations determined by absorption measurements at 280 nm. Aliquots of the elutions were stored at 4°C and at room temperature for 2 days. To pellet possibly precipitated protein, samples were ultracentrifuged at 150'000 rpm, 4°C, 40 min and supernatants were loaded on a SDS-PAGE.

3.4.3 Single particles and sample homogenity

Single particle grids were prepared by adsorbing 4 μl of purified protein solutions at concentrations of 0.1 - 0.001 mg/ml for 5 sec to copper grids coated with a carbon film. Grids were washed 4 times with distilled water and stained twice for 12 sec with 2% uranyl acetate. Single particles were imaged with a Hitachi H8000 electron microscope operated at 200 kV.

3.4.4 Screening for 2D crystallization conditions

Samples for 2D crystallization trials were mixed with lipids at various LPRs, incubated for approximately 1 hour before loading into dialysis buttons and dialyzing for 2 weeks if the detergent used was DDM and 5 days in the case of DM. Samples were checked by negative stain EM (grids prepared as described for single particles but with an adsorption time of 30 sec - 1 min.) and imaged using a Hitachi H8000 TEM at magnifications of 10'000 and 50'000 x.

3.4.5 Activity assays

Purified AQP8 in DM was reconstituted in a lipid mixture of POPS/POPC (3:7) at LPRs 10, 30, 60 and 90 by dialysing against 20 mM Tris-HCl; pH 8, 154 mM NaCl, 0.03 % NaN_3 for 6 days. The lipid concentration was kept at 2 mg/ml and the detergent concentration was 2 % DM before starting dialysis in tubes with a cut-off at 12 - 14 kDa. As control, liposomes without protein were produced. The samples were checked by negative stain EM and filtered using a Minisart 0.2 μm filter unit. Proteoliposomes were exposed to an inwardly directed 100 mM sucrose gradient in a stopped flow apparatus, and shrinkage of vesicles was observed by measuring the increase in 90° light scattering at 530 nm over 5-10 sec. For blocking water channel activity, proteoliposomes of LPR 10 were incubated with 2 mM $HgCl_2$ for 30 min at room temperature before subjecting them to the sucrose gradient. Traces of 5-10 individual runs per experiment were normalized, averaged and fitted to single exponential equations using the program Igor Pro. In the case of control vesicles, were no change in light scattering could be observed at all, no data processing or fitting was performed.

3.5 Conclusions and Outlook

Characteristics of mammalian AQP8 are its expression in rat testis [95] (but absence in human testis [93]), liver [95, 96], intestines [93] and kidney [25], where its seems to be mainly localized in intracellular vesicles [25, 97]. Its unusual structure compared to other mammalian aquaporins puts it into a unique position within the aquaporin family and emphasizes the interest of its structural analysis. Within this work, heterologously overexpressed AQP8 was purified, tested for activity and initial screenings for 2D crystallization were made. The purity and homogenity of AQP8 in different detergents could be ascertained by SDS-PAGE and single particle EM. Proteoliposomes of AQP8 reconstituted at different LPRs show corresponding differences in water transport activity, while control vesicles without protein do not show any water transport. Initial crystallization screenings resulted in samples containing tubular crystals that were analyzed by correlation averaging, but still need improvement through fine-tuning the crystallization conditions. Although no highly ordered crystals suitable for structure determination have been obtained yet, the presented results are promising and motivating for further experiments aiming a structural characterization of AQP8.

Appendix A

The 5 Å Structure of Heterologously Expressed SoPIP2;1

In the following the publication "The 5 Å Structure of Heterologously Expressed SoPIP2;1" is appended as published in Journal of Molecular Biology, 2006, volume 350, pages 611-616. Contribution to this work was purification and 2D crystallization of SoPIP2;1, data collection, structure determination and fitting of the AQP1 atomic model into the 3D map of SoPIP2;1.

doi:10.1016/j.jmb.2005.05.001

J. Mol. Biol. (2005) **350**, 611–616

JMB

Available online at www.sciencedirect.com

SCIENCE DIRECT®

ELSEVIER

COMMUNICATION

The 5 Å Structure of Heterologously Expressed Plant Aquaporin SoPIP2;1

W. Kukulski[1], A. D. Schenk[1], U. Johanson[2], T. Braun[1], B. L. de Groot[3] D. Fotiadis[1], P. Kjellbom[2] and A. Engel[1]*

[1]*Maurice E. Müller Institute for Microscopy, Biozentrum University of Basel, CH-4056 Basel, Switzerland*

[2]*Department of Plant Biochemistry, Lund University S-221 00 Lund, Sweden*

[3]*Computational Biomolecular Dynamics Group Max-Planck-Institute for Biophysical Chemistry, Am Fassberg 11, D-37077 Göttingen Germany*

**Corresponding author*

SoPIP2;1 is one of the major integral proteins in spinach leaf plasma membranes. In the *Xenopus* oocyte expression system its water channel activity is regulated by phosphorylation at the C terminus and in the first cytosolic loop. To assess its structure, SoPIP2;1 was heterologously expressed in *Pichia pastoris* as a His-tagged protein and in the non-tagged form. Both forms were reconstituted into 2D crystals in the presence of lipids. Tubular crystals and double-layered crystalline sheets of non-tagged SoPIP2;1 were observed and analyzed by cryo-electron microscopy. Crystalline sheets were highly ordered and diffracted electrons to a resolution of 2.96 Å. High-resolution projection maps of tilted specimens provided a 3D structure at 5 Å resolution. Superposition of the SoPIP2;1 potential map with the atomic model of AQP1 demonstrates the generally well conserved overall structure of water channels. Differences concerning the extracellular loop A explain the particular crystal contacts between oppositely oriented membrane sheets of SoPIP2;1 2D crystals, and may have a function in rapid volume changes observed in stomatal guard cells or mesophyll protoplasts. This crystal packing arrangement provides access to the phosphorylated C terminus as well as the loop B phosphorylation site for studies of channel gating.

© 2005 Elsevier Ltd. All rights reserved.

Keywords: aquaporin; electron diffraction; electron microscopy; three-dimensional structure; two-dimensional crystals

Cytosolic osmoregulation is maintained at the single-cell level and whole-plant water homeostasis is an essential function for every plant. It is accomplished by a complex and only rudimentarily understood system. While long-distance water transport is fulfilled by the vascular tissue, the cells themselves provide a rapid short-distance water flow through membranes. Proteins of the aquaporin family are key components in cellular water homeostasis, and they account for a significant fraction of the total amount of integral membrane proteins of plant plasma membranes.[1] Their importance is demonstrated also by the fact that in *Arabidopsis* 35 genes encode expressed aquaporin-like proteins and around one-third of these are located at the plasma membrane.[2]

At the cellular level, the maintenance of the water balance is an interplay between plasma membrane and tonoplast aquaporins (plasma membrane intrinsic proteins (PIPs) and tonoplast intrinsic proteins (TIPs), respectively). The PIPs are subdivided into two groups, the PIP1 and PIP2 isoforms. The latter have a longer C-terminal region and, when expressed in *Xenopus* oocytes, show a higher water transport activity than the PIP1 isoforms.[3]

SoPIP2;1, in previous nomenclature called PM28A, is a PIP2 isoform in *Spinacia oleracea* (spinach) leaf plasma membranes, where aquaporins constitute ~20% of all integral membrane proteins.[4] In its C-terminal region, a serine residue was found to be phosphorylated *in vivo*, in response to increasing apoplastic water potential.[4] Results generated by using the *Xenopus* oocyte expression system in combination with site-directed

---

Abbreviations used: AQP, aquaporin; PIP, plasma membrane intrinsic protein; TIP, tonoplast intrinsic protein.

E-mail address of the corresponding author: andreas.engel@unibas.ch

0022-2836/$ - see front matter © 2005 Elsevier Ltd. All rights reserved.

mutagenesis suggested that phosphorylation at Ser274 in the C-terminal region regulates the water channel activity of SoPIP2;1.[5] Furthermore, another serine residue, Ser115, in a consensus phosphorylation site in the first cytosolic loop, i.e. loop B, was identified as an additional putative regulatory phosphorylation site.[5] A hypothetical model has been presented in which an osmosensor senses the difference and triggers the increase of the intracellular concentration of Ca^{2+} when the apoplastic water potential is higher than the water potential in the cell.[5,6] This leads to the activation of a plasma membrane-associated Ca^{2+}-dependent protein kinase, which phosphorylates SoPIP2;1 at the Ser274 residue and thus facilitates water influx. At low apoplastic water potential, the channel is dephosphorylated and water flow through the pore is restricted. The consensus phosphorylation site at Ser274 in the C-terminal region is conserved in all PIP2 isoforms, independent of species, but not in the PIP1 isoforms, which have a shorter C-terminal region. The consensus phosphorylation site in the loop B at Ser115 is conserved in all PIPs, i.e. in all PIP1 as well as PIP2 isoforms.[2]

Several aquaporin structures have been solved in the past few years; human AQP1,[7,8] AQP0 from sheep[9] and bovine[10] eye lens, as well as two bacterial members, GlpF[11] and AqpZ.[12] Together with molecular dynamics simulations,[13–17] these structures gave insight into function and selectivity of water channels. In the case of AQP0, clues about its specific pH-dependent regulation could be derived,[9] and the structures of the open[10] and closed[9] AQP0 water channel are now available. The only plant aquaporin for which structural data are available is a projection map of the vacuolar membrane aquaporin α-TIP determined by electron crystallography.[18] Thus, the density map presented here is the first 3D plant aquaporin structure. Furthermore, we report here, to our knowledge, the first structure of a heterologously expressed aquaporin in any eukaryotic species.

SoPIP2;1 was expressed both as His-tagged and as non-tagged protein in the methylotrophic yeast *Pichia pastoris*. These clones both express SoPIP2;1 variants at similarly high levels. When reconstituted into proteoliposomes and exposed to an osmotic gradient, recombinant SoPIP2;1 shows efficient water channel activity.[19]

Both His-tagged and non-tagged SoPIP2;1 could be reconstituted into several crystal forms. Although more different forms were obtained with the His-tagged protein (data not shown), better-ordered crystals resulted from non-tagged SoPIP2;1. We were interested in the native SoPIP2;1 in the spinach plasma membrane, and so we concentrated on the structural analysis of crystals reconstituted in the presence of lipids and the non-tagged protein. Non-tagged SoPIP2;1 crystallized in two forms. Tubular vesicles exhibited a specific surface texture, resulting from up-down oriented tetramers that are packed into alternating rows (data not shown). Image processing analysis revealed these crystals to be anisotropically ordered, and thus not suitable for high-resolution structural analysis. The second crystal type concerns membrane sheets that are mostly double-layered, exhibit $p4$ symmetry, and have lattice constants of $a=b=65$ Å. In contrast to the coaxially packed double-layered AQP0 crystals,[9,20] the two crystalline layers of SoPIP2;1 are shifted against each other by exactly half a unit cell in the x and y direction, and are thus packed in precise register as well. The crystallographic unit cell comprises a tetramer from one layer and four monomers from four neighboring tetramers in the opposing layer. Occasionally recorded single layers are generally less well ordered, suggesting that a stabilizing crystal contact exists between the two layers.

The crystal quality was assessed by electron diffraction at low electron dose (<5 é/Å^2). Strong diffraction spots could be observed to a resolution of 2.96 Å on untilted crystals and to 3.7 Å at a tilt angle of 60° (Figure 1). For structure determination

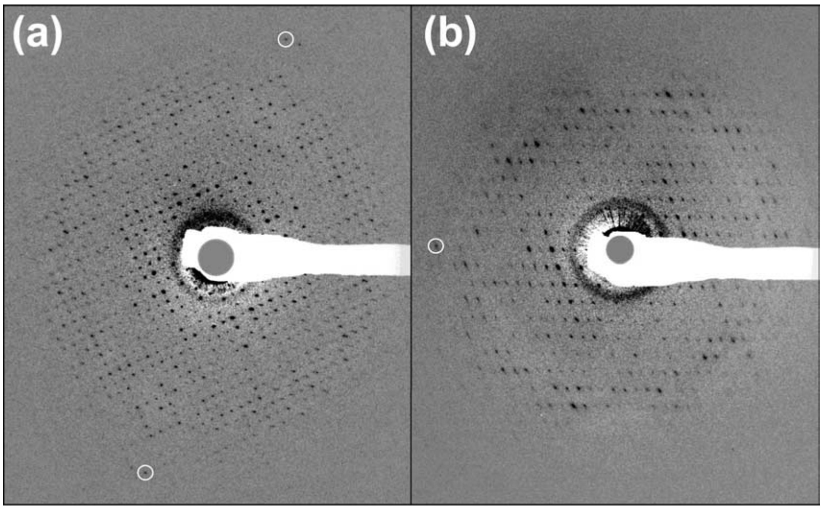

Figure 1. Electron diffraction of double-layered crystals at (a) 0° tilt and (b) 60° tilt. The circles in (a) indicate spots (16,15) corresponding to a resolution of 2.96 Å. In (b), the circle indicates spot (16,0) at a resolution of 3.7 Å. Crystal samples were embedded in 2% (w/v) glucose on molybdenum grids covered with a carbon film that was previously evaporated onto mica and floated on the grid. Electron diffraction patterns were recorded at low electron doses (<5 é/Å^2) on a Gatan 2K×2K CCD camera with a Philips CM200 FEG operated at 200 kV. The 2D crystals of OG-solubilized SoPIP2;1 were grown in the presence of *Escherichia coli* polar lipids at an LPR of 0.3 by dialysis for three days against a buffer containing 20 mM Tris–HCl (pH 8), 100 mM NaCl, 50 mM $MgCl_2$, 2 mM DTT, 0.03% (w/v) NaN_3.

high-resolution images of tilted specimens were collected and combined to obtain a 3D potential map (Table 1).

One tetramer and the complete unit cell are shown in Figure 2(a) and (b), respectively, with one monomer highlighted. Seven rod-like structures are clearly recognizable. By comparison with the atomic model of human AQP1,[21] they can be assigned to transmembrane helices 1–6 and loops B and E that form half-helices that fold back into the membrane to meet in the middle.[7] The remarkable arrangement of the two crystal layers stacked together by a tongue-and-groove fit of the extracellular surface, which is facilitated by the shift of one layer with respect to the other, is shown in Figure 2(c). This is radically different from the head-to-head coaxial packing of tetramers in the AQP0 double-layered crystals.[9]

The overall architecture of the channel has substantial similarity to AQP1, but some differences can be distinguished. The most remarkable difference is the length and straightness of helix 1. When compared to AQP1, helix 1 of SoPIP2;1 appears to protrude farther out from the extracellular membrane surface and to point towards the 4-fold axis of the tetramer (Figure 3(a) and (b)). A corresponding alteration is found for helix 2, which is more tilted at its N terminus than helix 2 of AQP1. All other helices fit well to the corresponding helices in AQP1. The visible differences in helices 1 and 2 dictate a different position of the connecting loop A in SoPIP2;1. In AQP1, this loop lies on top of helices 1 and 2, parallel with the side of the monomer. In the map of SoPIP2;1, however, the positions of the helix 1 C terminus and the helix 2 N terminus suggest that loop A is oriented towards the 4-fold center of the tetramer (Figure 3(a)). The tongue-and-groove packing arrangement results from the extracellular end of helix 1, which protrudes into the opposite layer, filling the gap between adjacent tetramers (Figure 2(b) and (c)). This suggests that the stability of the double-layered crystals might be the result of a contact between loops A from one layer with helices 3 and/or 6 of the opposing layer. Loop A in SoPIP2;1 is also different from that in AQP0, where tetramers are coaxially stacked face-to-face by prominent interactions between Pro38 in loop A, and a Pro–Pro motif (Pro109 and Pro110) in loop C.[9] It transpires that the crystalline packing of the two layers is, in both cases, dictated to a significant extent by the configuration of loop A.

Beside SoPIP2;1 and AQP0 a third aquaporin, AQP2, has been reported to preferably form double-layered two-dimensional crystals ordered to superior resolution.[22] In the case of AQP0,[9] this crystal form reflects the native state in the eye lens core, where AQP0 forms membrane junctions. AQP2 forms crystal contacts between the cytosolically located termini of the proteins and thereby differs from AQP0 and SoPIP2;1. The crystal packing of AQP2 is most probably not representing an *in vivo* situation but rather a crystallization artifact.[22] Whether the interactions of the extracellular parts of opposing SoPIP2;1 tetramers represent an *in vivo* situation has not been assessed. However, there are *in vivo* situations where different membrane domains of the plasma membrane of a cell are likely to interact *via* protein–protein interactions. Stomata closure and opening is accompanied by a substantial volume change of the guard cells. The membrane surface increase upon stomata opening cannot be explained by stretching of the plasma membrane.[23–25] It has to be attributed either to vesicles fusing with the plasma membrane or to plasma membrane invaginations being unfolded. Very fast cell volume changes necessitating vesicle fusion or invaginations unfolding have been recorded for mesophyll protoplasts isolated from leaf tissue.[26–28] Immunogold electron microscopy has demonstrated PIP subfamily members to be associated with plasmalemmasomes, invaginations of the plasma membrane protruding into the cytosol towards the central vacuole of *Arabidopsis* mesophyll cells.[29] It is possible that major integral proteins of the plasma membrane, such as

Table 1. Crystallographic data

Plane group symmetry	*p*4
Unit cell parameters	
$a=b$ (Å)	65
c (Å)	200 (assumed)
$\alpha=\beta=\gamma$ (deg.)	90
No. processed images	156 (0°, 21; 10°, 28; 15°, 16; 20°, 23; 30°, 37; 45°, 28; 60°, 3)
No. merged phases	24,479
Resolution limit for merging	5.0 Å (in the membrane plane; *x*,*y*-direction) 7.14 Å (perpendicular to the membrane plane; *z*-direction)
Phase residual (IQ-weighted) (deg.)	43.0 (overall) 34.4 (100–9.7 Å) 39.6 (9.7–6.9 Å) 50.6 (6.9–5.6 Å) 60.8 (5.6–5 Å)
Completeness[a] (%)	36.5 (resolution volume: 5 Å in *x*,*y*, 7.14 Å in *z*) 57 (resolution volume 6 Å in *x*,*y*, 7.14 Å in *z*) 65 (resolution volume 6 Å in *x*,*y*, 10 Å in *z*)

[a] Only reflections within the resolution volume having a figure of merit over 0.5 were included; the missing cone is comprised in this volume.

aquaporins, participate in interactions stabilizing membrane invaginations.

At the C terminus of loop A, PIPs exhibit a highly conserved Cys, which is not present in other aquaporin-like proteins in plants (Figure 3(c); U.J., unpublished results). Using the multiple sequence alignment reported by Heymann & Engel,[30] the conserved Cys of SoPIP2;1 was found to correspond to Thr44 in human AQP1 (Figure 3(c)). As displayed in Figure 3(a) and (b), the N-terminal part of the AQP1 helix 2 should be tilted towards the 4-fold axis to fit to the potential map of SoPIP2;1 in this region. The corresponding four Cys in SoPIP2;1 would then be remarkably close to each other, and close to the 4-fold axis of the tetramer. The high level of conservation suggests a special function for this Cys. According to their nearness, which is due to the particular configuration of loop A, these four Cys may stabilize the SoPIP2;1 tetramer by fostering hydrogen bonds or complexing a metal ion.

The particular arrangement of the four Cys was confirmed quantitatively by fitting helical segments to the 3D potential map of SoPIP2;1 using the program ROTTRANS.[31] In addition, the helical backbones of the atomic models of AQP1 and AQP0 in both open and closed conformation were fitted to the potential map of SoPIP2;1 and yielded cross-correlation scores of 0.37 (AQP1),[21] 0.366 (AQP0 open),[10] and 0.367 (AQP0 closed).[9] The question of whether the water channel of SoPIP2;1 is in an open or closed state cannot be answered at the resolution available. Differences are likely to be related to the conformation of single amino acid side-chains, such as the Tyr149 in AQP0.[9]

The high level of water permeability showed in activity measurements of proteoliposomes[19] suggests the water channels of SoPIP2;1 to be in an open conformation. However, the phosphorylation state of crystallized SoPIP2;1 is not known, and the mechanism of phosphorylation-mediated gating of the channel remains to be elucidated. The 2D crystals and the 3D map of the functional protein in a lipid bilayer provide a solid framework for this goal. As a result of the orientation of the tetramers within the double-layered crystals, the cytosolic C terminus as well as the B-loop are accessible for

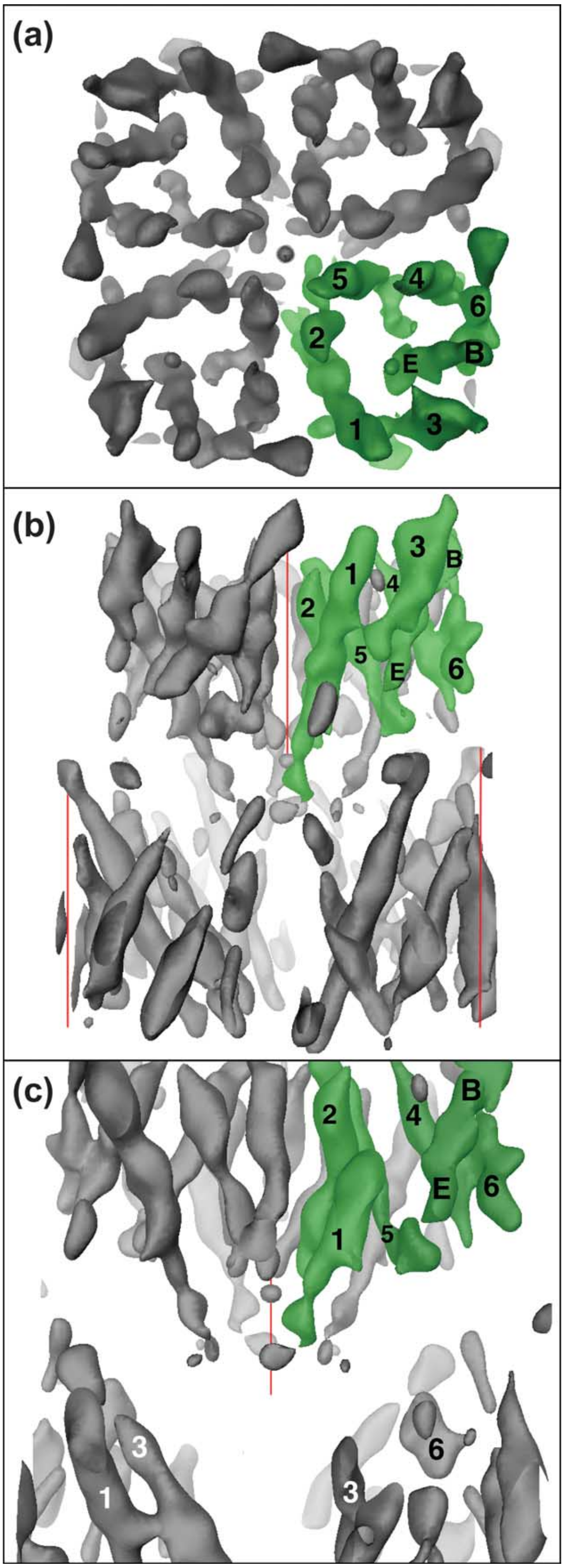

Figure 2. A 3D map of SoPIP2;1, calculated from 156 electron micrographs (see Table 1). (a) Cytosolic view of one tetramer. (b) Side-view of the unit cell comprising one tetramer and four monomers of the opposite layer. One monomer is highlighted in green. Helices 1–6 as well as loops B and E that fold back into the membrane and form a seventh transmembrane domain can be assigned as indicated. The 4-fold axes are drawn in red. (c) View into the center of the unit cell, where the extracellular ends of helices 1 from one tetramer protrude into the cleft between adjacent tetramers of the opposite layer. For clarity, parts of the map are cut away and the respective helices indicated. The map was calculated using the MRC software package.[32] Images were corrected for lattice distortions taking the Fourier-filtered images themselves as references. Measured phases and amplitudes were corrected for the tilted contrast transfer function and merged imposing $p4$ symmetry. Phase origins were refined and lattice lines for amplitudes and phases were fitted to create a 3D data set.

phosphorylation experiments, allowing the channel to be resolved in the open and closed states.

References

1. Johansson, I., Karlsson, M., Johanson, U., Larsson, C. & Kjellbom, P. (2000). The role of aquaporins in cellular and whole plant water balance. *Biochim. Biophys. Acta*, **1465**, 324–342.
2. Johanson, U., Karlsson, M., Johansson, I., Gustavsson, S., Sjövall, S., Fraysse, L. *et al.* (2001). The complete set of genes encoding major intrinsic proteins in *Arabidopsis* provides a framework for a new nomenclature for major intrinsic proteins in plants. *Plant Physiol.* **126**, 1358–1369.
3. Chaumont, F., Barrieu, F., Wojcik, E., Chrispeels, M. & Jung, R. (2000). Plasma membrane intrinsic proteins from maize cluster in two sequence subgroups with differential aquaporin activity. *Plant Physiol.* **122**, 1025–1034.
4. Johansson, I., Larsson, C., Ek, B. & Kjellbom, P. (1996). The major integral proteins of spinach leaf plasma membranes are putative aquaporins and are phosphorylated in response to Ca^{2+} and apoplastic water potential. *Plant Cell*, **8**, 1181–1191.
5. Johansson, I., Karlsson, M., Shukla, V. K., Chrispeels, M. J., Larsson, C. & Kjellbom, P. (1998). Water transport activity of the plasma membrane aquaporin SoPIP2;1 is regulated by phosphorylation. *Plant Cell*, **10**, 451–459.
6. Kjellbom, P., Larsson, C., Johansson, I., Karlsson, M. & Johanson, U. (1999). Aquaporins and water homeostasis in plants. *Trends Plant Sci.* **8**, 308–314.
7. Murata, K., Mitsuoka, K., Hirai, T., Walz, T., Agre, P., Heyman, B. *et al.* (2000). Structural determinants of water permeation through aquaporin-1. *Nature*, **407**, 605–612.
8. Sui, H., Han, B. G., Lee, J. K., Walian, P. & Jap, B. K. (2001). Structural basis of water-specific transport through AQP1 water channel. *Nature*, **414**, 872–878.
9. Gonen, T., Sliz, P., Kistler, J., Cheng, Y. & Walz, T. (2004). Aquaporin-0 membrane junctions reveal the structure of a closed water pore. *Nature*, **429**, 193–197.
10. Harries, W. E., Akhavan, D., Miercke, L. J., Khademi, S. & Stroud, R. M. (2004). The channel architecture of aquaporin 0 at a 2.2-Å resolution. *Proc. Natl Acad. Sci. USA*, **101**, 14045–14050.

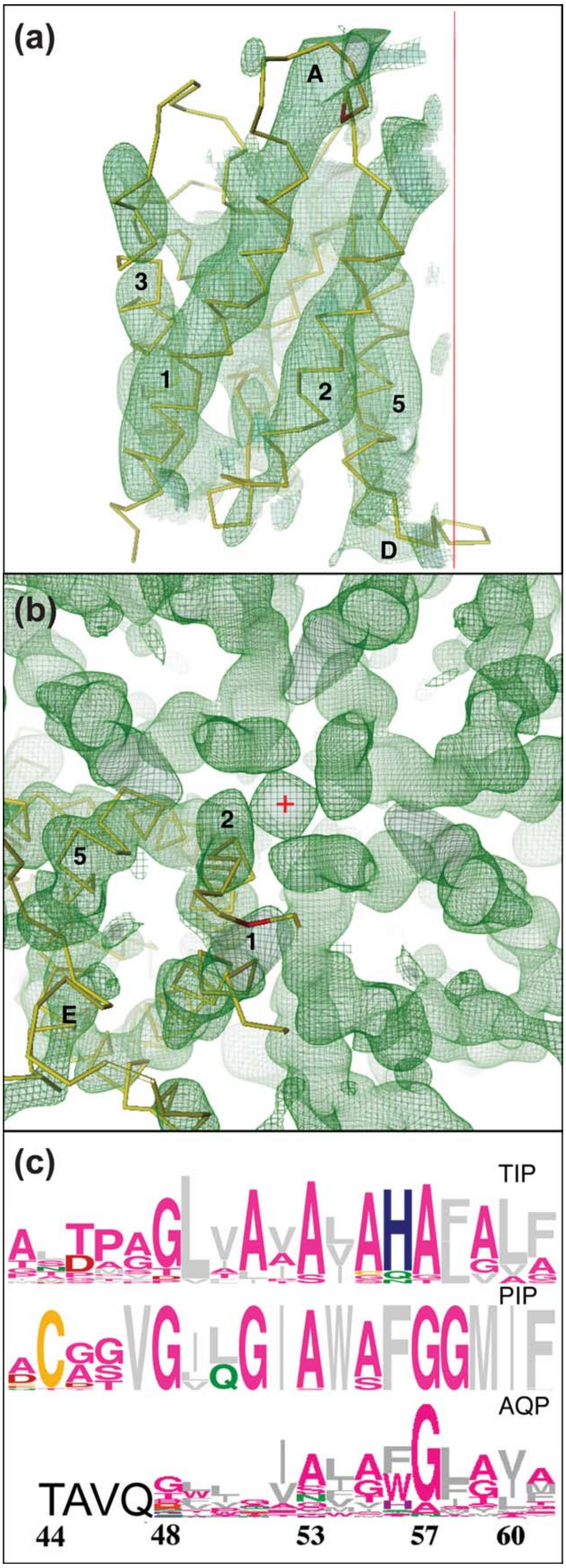

Figure 3. (a) Superposition of SoPIP2;1 potential map (green) with the C^{α} backbone of the atomic model of AQP1 (yellow); Thr44 is highlighted in red. The 4-fold axis is drawn in red in this side-view of the superimposed monomers, extracellular face up. (b) Extracellular view of a SoPIP2;1 tetramer with one AQP1 monomer fitted into a SoPIP2;1 monomer. The 4-fold center is indicated by a red cross. Superposition of the two structural datasets was performed using the program DINO (http://www.dino3D.org). (c) Alignment of the PIP and TIP consensus sequences of parts of loop A and helix 2 with the aquaporin consensus sequence of helix 2 (residues 48–61).[30] The PIP consensus sequence is based on SoPIP2;1 (AAA99274), all *Arabidopsis* PIPs,[2] maize PIPs,[33] and PIPs from *Picea abies* and *Physcomitrella patens* (CAB06080, CAB07783, AAS65964, translation of Physcobase contig 10071 http://moss.nibb.ac.jp/). The TIP consensus sequence is derived from *Arabidopsis*[2] and maize TIPs.[33] Sequence conservation is displayed by the sequence logos technique.[34,35] According to this alignment, the highly conserved Cys in PIPs corresponds to Thr44 in AQP1 (black letters).

11. Fu, D., Libson, A., Miercke, L. J. W., Weitzman, C., Nollert, P., Krucinski, J. & Stroud, R. M. (2000). Structure of a glycerol-conducting channel and the basis for its selectivity. *Science*, **290**, 481–486.
12. Savage, D. F., Egea, P. F., Robles-Colmenares, Y., O'Connell, J. D., III & Stroud, R. M. (2003). Architecture and selectivity in aquaporins: 2.5 Å X-ray structure of aquaporin Z. *PloS Bio.* **1**, 334–340.
13. De Groot, B. L. & Grubmüller, H. (2001). Water permeation across biological membranes: mechanism and dynamics of aquaporin-1 and GlpF. *Science*, **294**, 2352–2356.
14. Tajkhorshid, E., Nollert, P., Jensen, M. O., Miercke, L. J., O'Connell, J., Stroud, R. M. & Schulten, K. (2002). Control of the selectivity of the aquaporin water channel family by global orientational tuning. *Science*, **296**, 525–530.
15. De Groot, B. L., Frigato, T., Helms, V. & Grubmüller, H. (2003). The mechanism of proton exclusion in the aquaporin-1 water channel. *J. Mol. Biol.* **333**, 279–293.
16. Chakrabarti, N., Tajkhorshid, E., Roux, B. & Pomes, R. (2004). Molecular basis of proton blockage in aquaporins. *Structure (Camb.)*, **12**, 65–74.
17. Chakrabarti, N., Roux, B. & Pomes, R. (2004). Structural determinants of proton blockage in aquaporins. *J. Mol. Biol.* **343**, 493–510.
18. Daniels, M. J., Chrispeels, M. J. & Yeager, M. (1999). Projection structure of a plant vacuole membrane aquaporin by electron cryo-crystallography. *J. Mol. Biol.* **294**, 1337–1349.
19. Karlsson, M., Fotiadis, D., Sjövall, S., Johansson, I., Hedfalk, K., Engel, A. & Kjellbom, P. (2003). Reconstitution of water channel function of an aquaporin overexpressed and purified from *Pichia pastoris*. *FEBS Letters*, **537**, 68–72.
20. Fotiadis, D., Hasler, L., Müller, D. J., Stahlberg, H., Kistler, J. & Engel, A. (2000). Surface tongue-and-groove contours on lens MIP facilitate cell–cell adherence. *J. Mol. Biol.* **300**, 779–789.
21. De Groot, B. L., Engel, A. & Grubmüller, H. (2001). A refined structure of human aquaporin-1. *FEBS Letters*, **504**, 206–211.
22. Schenk, A. D., Werten, P. J. L., Scheuring, S., de Groot, B. L., Müller, S. A., Stahlberg, H. *et al*. (2005). The 4.5 Å structure of human AQP2. *J. Mol. Biol*. In the press.
23. Blatt, M. R. (2000). Cellular volume control in stomatal movements in plants. *Annu. Rev. Cell Dev. Biol.* **16**, 221–241.
24. Geelen, D., Leyman, B., Batoko, H., Di Sansebastiano, G. P., Moore, I. & Blatt, M. R. (2002). The abscisic acid-related SNARE homolog NtSyr1 contributes to secretion and growth: evidence from competition with its cytosolic domain. *Plant Cell*, **14**, 387–406.
25. Pratelli, R., Sutter, J. U. & Blatt, M. R. (2004). A new catch in the SNARE. *Trends Plant Sci.* **9**, 187–195.
26. Ramahaleo, T., Morillon, R., Alexandre, J. & Lassalles, J. P. (1999). Osmotic water permeability of isolated protoplasts. Modification during development. *Plant Physiol.* **119**, 885–896.
27. Morillon, R., Lienard, D., Chrispeels, M. J. & Lassalles, J. P. (2001). Rapid movements of plants organs require solute–water cotransporters or contractile proteins. *Plant Physiol.* **127**, 720–723.
28. Moshelion, M., Moran, M. & Chaumont, F. (2004). Dynamic changes in the osmotic water permeability of protoplast plasma membrane. *Plant Physiol.* **135**, 2301–2317.
29. Robinson, D. G., Sieber, H., Kammerloher, W. & Schaffner, A. R. (1996). PIP1 aquaporins are concentrated in plasmalemmasomes of *Arabidopsis thaliana* mesophyll. *Plant Physiol.* **111**, 645–649.
30. Heymann, J. B. & Engel, A. (2000). Structural clues in the sequence of the aquaporins. *J. Mol. Biol.* **295**, 1039–1053.
31. de Groot, B. L., Heymann, J. B., Engel, A., Mitsuoka, K., Fujiyoshi, Y. & Grubmüller, H. (2000). The fold of human aquaporin 1. *J. Mol. Biol.* **300**, 987–994.
32. Crowther, R. A., Henderson, R. & Smith, J. M. (1996). MRC image processing programs. *J. Struct. Biol.* **116**, 9–16.
33. Chaumont, F., Barrieu, F., Wojcik, E., Chrispeels, M. J. & Jung, R. (2001). Aquaporins constitute a large and highly divergent protein family in maize. *Plant Physiol.* **125**, 1206–1215.
34. Crooks, G. E., Hon, G., Chandonia, J. M. & Brenner, S. E. (2004). WebLogo: a sequence logo generator. *Genome Res.* **14**, 1188–1190.
35. Schneider, T. D. & Stephens, R. M. (1990). Sequence logos: a new way to display consensus sequences. *Nucl. Acids Res.* **18**, 6097–6100.

Edited by W. Baumeister

(Received 18 February 2005; received in revised form 25 April 2005; accepted 2 May 2005)

Appendix B

Controlled 2D Crystallization of Membrane Proteins Using Methyl-β-Cyclodextrin

In the following the publication "Controlled 2D Crystallization of Membrane Proteins Using Methyl-β-Cyclodextrin" is appended as published in Journal of Structural Biology, 2006. Contribution to this work was purification of SoPIP2;1 and collection of electron diffraction data.

ARTICLE IN PRESS

Available online at www.sciencedirect.com
ScienceDirect
Journal of Structural Biology xxx (2006) xxx–xxx
Journal of Structural Biology
www.elsevier.com/locate/yjsbi

Controlled 2D crystallization of membrane proteins using methyl-β-cyclodextrin

Gian A. Signorell, Thomas C. Kaufmann, Wanda Kukulski,
Andreas Engel, Hervé-W. Rémigy *

M. E. Müller Institute for Microscopy at the Biozentrum, University of Basel, Basel, Switzerland

Received 9 May 2006; received in revised form 21 July 2006; accepted 22 July 2006

Abstract

High-resolution structural data of membrane proteins can be obtained by studying 2D crystals by electron crystallography. Finding the right conditions to produce these crystals is one of the major bottlenecks encountered in 2D crystallography. Many reviews address 2D crystallization techniques in attempts to provide guidelines for crystallographers. Several techniques including new approaches to remove detergent like the biobeads technique and the development of dedicated devices have been described (dialysis and dilution machines). In addition, 2D crystallization at interfaces has been studied, the most prominent method being the 2D crystallization at the lipid monolayer. A new approach based on detergent complexation by cyclodextrins is presented in this paper. To prove the ability of cyclodextrins to remove detergent from ternary mixtures (lipid, detergent and protein) in order to get 2D crystals, this method has been tested with OmpF, a typical β-barrel protein, and with SoPIP2;1, a typical α-helical protein. Experiments over different time ranges were performed to analyze the kinetic effects of detergent removal with cyclodextrins on the formation of 2D crystals. The quality of the produced crystals was assessed with negative stain electron microscopy, cryo-electron microscopy and diffraction. Both proteins yielded crystals comparable in quality to previous crystallization reports.
© 2006 Elsevier Inc. All rights reserved.

Keywords: 2D Crystallization; Membrane protein; Cyclodextrin; Electron microscopy

1. Introduction

Detergents are used to extract proteins from membranes and during subsequent purification to obtain samples suitable for crystallization. During this process the membrane protein structure and function are affected by the loss of interaction with the lipids. To reconstitute membrane proteins into a lipid bilayer in order to obtain 2D crystals, the detergent must be removed from a protein–lipid–detergent ternary mixture. There are mainly three ways to remove detergent: dialysis, adsorption to biobeads and dilution (Rigaud et al., 1997; Hasler et al., 1998; Remigy et al., 2003). However, all of these methods have their limitations. For dialysis, the rate of detergent removal is closely related to the critical micellar concentration (CMC) of the detergent (Jap et al., 1992; Kuhlbrandt, 1992). For example, dialysis of low CMC detergents (such as Triton X-100 or dodecyl-β-D-maltoside (DDM)) takes weeks at room temperature. Low CMC detergents are often necessary to keep the protein in its active form, as they are better substitutes for the bilayer than high CMC detergents. When low CMC detergents are required, the use of biobeads offers the advantage of a fast detergent removal. However, this can be a problem, since the high efficiency of detergent adsorption to biobeads may result in too fast detergent removal leading to aggregation primarily when small (<20 μl) reconstitution volumes are used. Therefore a minimal initial volume of ternary mixture of 100 μl is required for removing the detergent in a controlled manner. This will lead to compromises

---

* Corresponding author. Fax: +41 61 267 21 09.
E-mail address: herve.remigy@unibas.ch (H.-W. Rémigy).

1047-8477/$ - see front matter © 2006 Elsevier Inc. All rights reserved.
doi:10.1016/j.jsb.2006.07.011

Please cite this article as: Gian A. Signorell et al., Controlled 2D crystallization of membrane proteins using methyl-β-cyclodextrin, Journal of Structural Biology (2006), doi:10.1016/j.jsb.2006.07.011

in the selection of screening conditions, considering the limited amount of protein sample usually available. In a dilution experiment, the protein concentration should remain above 0.2–0.5 mg/ml and the initial detergent concentration should be as low as possible (Remigy et al., 2003). An advantage inherent to dilution is the possibility to slow down or even interrupt the reconstitution process at any time, thereby allowing for slow and controlled passage through the critical phase of crystal assembly. The major drawback of the dilution approach, however, is the inability to remove the detergent completely.

Here, we present an alternative approach to produce 2D crystals by detergent removal based on inclusion complexes with cyclodextrins. α-, β- or γ-cyclodextrins are ring shaped molecules made of 6, 7 and 8 glucose molecules, respectively. The non-polar environment inside the ring enables cyclodextrin to enclose hydrophobic or amphiphilic molecules like cholesterol or detergents. This technique was already used to perform reconstitution of active membrane proteins into membranes at a high lipid-to-protein ratio (LPR) (Degrip et al., 1998; Turk et al., 2000; Zampighi et al., 2003). The reconstitution rate is directly related to the amount of cyclodextrin added. The higher affinity of the inclusion compounds of cyclodextrin for detergents than for lipids prevents the LPR to change during reconstitution. Affinity tests between cyclodextrin and many anionic, nonionic and zwitterionic detergents of various CMC have been made at high LPR and have shown an almost complete lipid recovery (Degrip et al., 1998). A suitable cyclodextrin (α-, β- or γ-cyclodextrin) with a sufficiently high binding affinity can be found for most detergents (Degrip et al., 1998). The affinity of a detergent molecule for a cyclodextrin is largely determined by the fit of the detergent's hydrophobic moiety with the cyclodextrin cavity (Degrip et al., 1998). All alkyl-chain-containing detergents have high affinity with β-cyclodextrin. γ-Cyclodextrin should be considered when a detergent with a bulky hydrophobic chain is used. Fully functional reconstitution of membrane proteins with any kind of detergent is therefore possible.

The cyclodextrin approach needs to be adapted to produce proteoliposomes used for membrane protein crystallization. Finding the conditions promoting intermolecular and intramolecular interactions is mandatory, e.g., lipid–protein interactions need to be optimized by screening lipids of different nature and by varying the LPR. Since specific protein–protein interactions depend on the pH and the presence of specific counterions, the search space for optimal crystallization conditions is of an even higher dimensionality.

OmpF and SoPIP2;1 were used to test this new 2D crystallization approach. OmpF is a β-barrel membrane protein from *Escherichia coli* and SoPIP2;1 an α-helical aquaporin from spinach leaf plasma membrane, over-expressed in *Pichia pastoris* (Karlsson et al., 2003). Both proteins have their structures already determined by X-ray crystallography (Cowan et al., 1992; Tornroth-Horsefield et al., 2005). In the present work, methyl-β-cyclodextrin (MBCD) was selected for its high solubility and its high affinity for a wide range of detergents commonly used in membrane protein chemistry.

2. Materials and methods

2.1. MBCD/detergent titration curve

The detergents octyl-β,D-glucoside (OG) and dodecyl-*N*,*N*-dimethylamine-*N*-oxide (LDAO) were purchased from Anatrace (Ohio, USA), whereas octyl-polyoxyethylene (Octyl-POE) was purchased from Alexis (Lausen, Switzerland). All detergents were of high purity grade (⩾98%) and were used without further purification. MBCD–detergent mixtures were obtained by dilution of appropriately combined stock solutions with reagent-grade water produced by a Milli-Q filtration system (>18 MΩ). The pipetted volumes were weighed on a balance (Mettler AE50) purchased from Mettler-Toledo (Greifensee, Switzerland). The different molar ratios were obtained by varying the MBCD concentration and keeping the detergent concentration constant above the corresponding CMC in order to have a constant surface tension reduction contribution from the detergent. Contact angles between a sample droplet and the supporting Parafilm were measured using a homemade device as described by Kaufmann et al. (2006). Measurements were carried out at room temperature.

For calculation purposes the mean molecular mass of the MBCD was determined by MALDI-TOF on a Bruker Scout 26 Reflex III instrument (Bruker Daltonik, Bremen, Germany). The mass spectrometric analysis revealed an average substitution rate of 1.77 methyl groups per glucose molecule, leading to a mean molecular mass of 1310.4 Da per MBCD molecule.

The molecular weight of Octyl-POE was calculated as the mean of the masses of all represented ethoxylated (EO) species ($n_{EO} = 1$–11) which gives 372.52 g/mol for the hypothetical number of ethylene-oxide units $n_{EO} = 5.5$. As density of Octyl-POE the value of 1.015 g/cm^3, determined by Rosenbusch et al. (2001) was used.

2.2. OmpF and SoPIP 2;1 purification and reconstitution

OmpF was produced in *E. coli*, purified as reported previously (Holzenburg et al., 1989) and solubilized in 1% Octyl-POE. SoPIP2;1, previously referred as PM28A, expressed in *Pichia pastoris* was purified according to Karlsson et al. (2003). The phospholipids used to prepare proteoliposomes were dissolved in chloroform at a concentration of 10 mg/ml, dried under a stream of argon, further dried overnight in a dessicator and weighed. Reagent-grade water was added and the lipid solutions were then sonicated for 2 min in a cold water bath using a Branson sonifier 250 tip at 20% of the maximum output power. An aqueous solution of the same detergent used for protein solubilization was added to the lipids to get a final detergent concentration of 1% (5 mg/ml dimyristoyl-phosphatidylcholine

Please cite this article as: Gian A. Signorell et al., Controlled 2D crystallization of membrane proteins using methyl-β-cyclodextrin, Journal of Structural Biology (2006), doi:10.1016/j.jsb.2006.07.011

(DMPC) lipids were solubilized in 1% Octyl-POE for OmpF, 5 mg/ml *E. coli* polar extract lipids in 1% OG for SoPIP2;1).

To have exactly defined starting conditions, the protein–detergent mixture was dialyzed overnight against the crystallization buffer containing detergent. OmpF was dialyzed at 4 °C overnight against 20 mM Hepes, pH 7, 100 mM NaCl, 10 mM $MgCl_2$, 3 mM NaN_3 and 1% Octyl-POE. SoPIP2;1 was dialyzed at 4 °C overnight against 20 mM Hepes, pH 7.5, 100 mM NaCl, 50 mM $MgCl_2$, 2 mM dithiothreitol, 3 mM NaN_3 and 1% OG. After dialysis the detergent concentration was measured as described above (Kaufmann et al., 2006) and adjusted to 1% Octyl-POE for OmpF and 1% OG for SoPIP2;1 by dilution with the corresponding buffer. The final protein concentrations before lipid addition were 1.5 and 1.2 mg/ml for OmpF and SoPIP2;1, respectively. DMPC was added to OmpF to cover LPRs ranging from 0.15 to 1 *E. coli* polar lipid extracts were added to SoPIP2; 1 to cover LPRs ranging from 0.3 to 0.4. After the detergent was removed by controlled MBCD addition (see below) at room temperature the samples were washed to eliminate the MBCD from the solution: after collection they were centrifuged for 15 min at 11 000 rpm using an Eppendorf centrifuge 5415C. The supernatant was discarded and the pellet resuspended in 400 μl detergent-free crystallization buffer. This procedure was repeated twice and after a final centrifugation the pellet was collected for cryo-electron microscopy (EM) characterization.

2.3. Controlled MBCD addition

MBCD was from Fluka. A dilution device described by Remigy et al. (2003) was used to perform the controlled addition of the MBCD. The MBCD solutions were obtained by addition of cyclodextrin to reagent grade water. The MBCD solution is supplied to a cuvette by a microsyringe. A valve prevents diffusion between the syringe and the cuvette. To keep the sample homogeneous, a stirrer is placed at the bottom of the cuvette. Fast reconstitutions lasting 30 min, 2 h and 12 h with initial ternary mixture volumes of 20 μl were performed. During these experiments the samples were constantly stirred. The volume of MBCD solution added was evaluated to compensate evaporation, and the concentration of MBCD in solution was calculated to exceed the minimal amount of cyclodextrin required (see MBCD/detergent titration curves) to remove completely the detergent from the ternary mixture (Kaufmann et al., 2006). For 30 min and 2 h, 10 μl of a 30% MBCD solution were added to the solution. For 12 h, 25 μl of a 10% MBCD solution were added. 30, 30 and 15 μl of crystalline sample were recovered from the 30 min, 2 h and 12 h experiments, respectively. Seventy-two hours and 144 h experiments were carried out with and without stirring with an initial ternary mixture volume of 40 μl. To overcome liquid loss during these longer experiments, bigger volumes of less concentrated cyclodextrin solutions were added. Four-hundred microliters of a 2% MBCD solution were added over 72 h and 600 μl of a 1.3% MBCD solution were added over 144 h. Two-hundred to 230 μl of crystalline sample were collected after the experiments.

2.4. Phospholipase A2 treatment

OmpF crystals were treated with bee venom phospholipase A2 (available from Sigma) to remove lipids from the proteoliposome and thus get closer crystal packing. This procedure was described by Mannella (1984). Loosely packed OmpF crystals (1 mg/ml) in a buffer containing 20 mM Hepes, pH 7, 100 mM NaCl, 10 mM $MgCl_2$, 3 mM NaN_3 and 1% Octyl-POE were used to perform this treatment. Ten microliters of OmpF were added to 2 ml of low salt buffer (0.005% MBCD, 1 mM Tris–HCl, 0.1 mM ethylene diamine tetra acetic acid, pH 7.5). 0, 0.3, 0.6 and 1.2 U/ml of phospholipase A2 were added to OmpF aliquoted in low salt buffer (1 mg of phospholipase corresponds to 1500 U). The mixture was incubated overnight at 4 °C. The solution was centrifuged in a Beckmann TL-100 ultracentrifuge for 90 min at 55 000 rpm (100 000*g*) at 4 °C. The supernatant was discarded and the pellet was resuspended in the low salt buffer.

2.5. Electron microscopy

Specimens for negative stain electron microscopy were prepared by adsorbing proteoliposomes onto carbon films previously rendered hydrophilic by glow discharging in air. The grids were washed three times with distilled water and stained with saturated uranyl acetate (2%). Micrographs were taken on a Hitachi H-7000 transmission electron microscope operated at 100 kV using magnifications of 5000–50 000. An optical bench with a laser beam was used to evaluate the diffraction quality of the micrographs. Well-ordered crystals were embedded in 2% glucose on molybdenum grids covered with a carbon film that was previously evaporated onto mica and floated on the grid. Electron diffraction patterns were recorded at low electron doses (<5 electrons per $Å^2$) on a Gatan 2K × 2K CCD camera with a Philips CM-200 FEG microscope operated at 200 kV.

3. Results

3.1. MBCD/detergent titration

The titration curves (Fig. 1) reveal the amount of MBCD needed for the neutralization of the respective detergents. All three curves show a sudden increase in the contact angle reflecting the MBCD–detergent complexation depleting the solution from detergent monomers, which can no more adsorb to the liquid–vapor and solid–liquid interfaces. The points at which the curves reach the plateau correspond to the molar ratios needed for complete complexation of the detergents by MBCD, i.e., the minimal amount required in an experiment. At the same time these

Please cite this article as: Gian A. Signorell et al., Controlled 2D crystallization of membrane proteins using methyl-β-cyclodextrin, Journal of Structural Biology (2006), doi:10.1016/j.jsb.2006.07.011

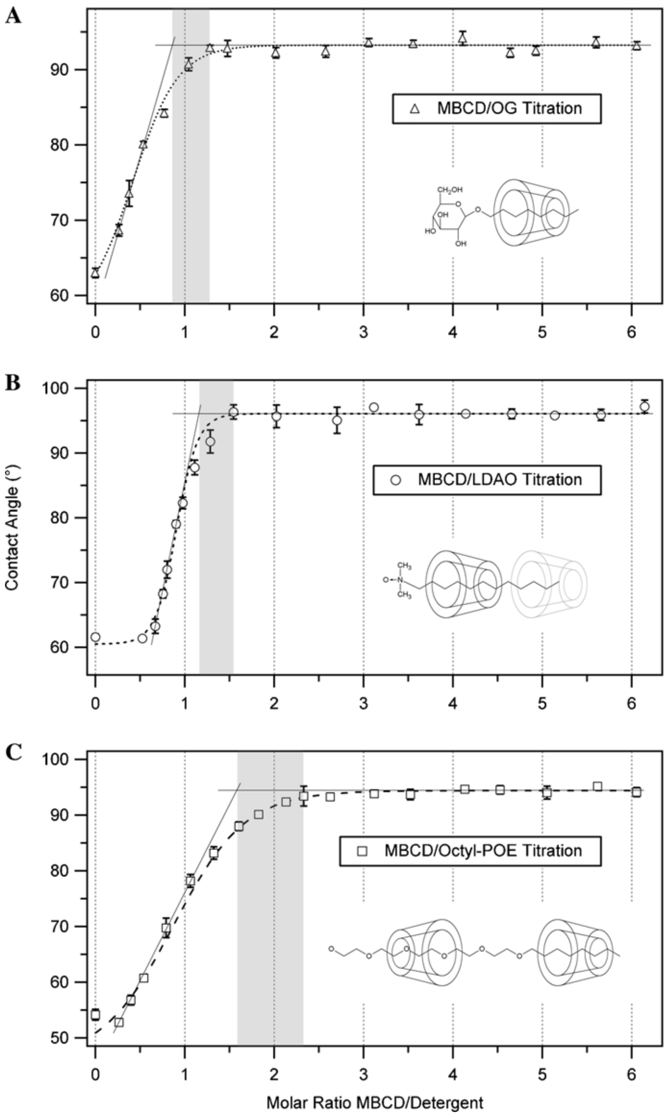

Fig. 1. MBCD–detergent titration curves. The measurements were performed at constant detergent concentration above the respective CMC of the detergents. One curve represents the mean of three measurements for each MBCD–detergent pair. The possible ranges for the stoichiometry of complex formation are shaded in gray. The illustrations depict the most probable inclusion stoichiometries as deduced from the measurements. In the case of the polydisperse Octyl-POE, pentaethylene glycol monooctyl ether (C_8E_5) is shown as a representative structure. (A) OG at 21 mM (CMC = 25 mM). (B) LDAO at 2.5 mM (CMC = 1.9 mM). (C) Octyl-POE at 10 mM (CMC = 6.6 mM).

points correspond to the upper boundary of the complex stoichiometry. The lower boundary is given by the intersection between the extrapolated plateau and the extrapolated initial slope reflecting the highest possible association constant for the complex formation.

The obtained ranges for the stoichiometries of complex formation are 0.9–1.3 for MBCD/OG, 1.2–1.5 for MBCD/LDAO and 1.6–2.3 for MBCD/Octyl-POE. The results suggest a 1:1 complex for MBCD and OG. In the case of LDAO the results comply with the formation of a predominant 1:1 complex and with a fraction of the species carrying a second MBCD molecule but with much lower affinity. The mean complex stoichiometry for the polydisperse Octyl-POE levels off at a molar ratio of around 2. This suggests that while the aliphatic chain is occupied by one MBCD molecule, the polyoxyethylene chain, which is variable in length, can be decorated with different amounts of MBCD molecules.

3.2. 2D Crystallization of the porin OmpF

Experiments ranging from 30 min to 144 h yielding OmpF crystals show that faster detergent removal rates (2 h and less) result in low quality crystals having diameters ranging from 50 to 500 nm, with a trigonal lattice ($a = b = 9 \pm 0.5$ nm; $\gamma = 60°$), which diffracted up to 2.7 nm resolution (Fig. 2A). Slower rates (12–144 h) result in the formation of large sheets having diameters ranging from 1 to 2 μm, with a trigonal lattice ($a = b = 9 \pm 0.5$ nm; $\gamma = 60°$) diffracting up to 2.4 nm resolution (Fig. 2B). Stirring did not affect the crystal quality. After phospholipase A2 treatment (Mannella, 1984) on OmpF crystals obtained after 144 h runs, crystals with a trigonal lattice ($a = b = 7.2 \pm 0.2$ nm; $\gamma = 60°$) diffracting beyond 2.2 nm resolution (Fig. 2C) were obtained.

3.3. 2D Crystallization of SoPIP2;1

SoPIP2;1 reconstitutions lasting 2 h (Fig. 3A) and less yielded large vesicles and small sheets but no significant diffraction was observed. Large sheets comparable to those previously reported (Kukulski et al., 2005) were obtained after 72 and 144 h experiments (Fig. 3B). Stirring did not affect the crystal quality. The largest sheets obtained after 144 h were used to perform direct electron diffraction. Images of electron diffraction patterns were taken from unwashed (Fig. 3C) and washed crystals (Fig. 3D). The electron diffraction patterns exhibit a p4 symmetry with the same lattice constants of $a = b = 9{,}6$ nm for both, unwashed and washed samples. The indicated spots for the unwashed crystals are 24,2 (Fig. 3C) and 24,3 for washed crystals (Fig. 3D), corresponding to a resolution of 4 Å. The unwashed sample (Fig. 3C) displays strong additional diffraction spots, arranged in a sixfold symmetry overlaying the typical diffraction pattern of SoPIP2;1. These spots are not present in the washed sample (Fig. 3D).

4. Discussion

The capability of cyclodextrin to complex any kind of detergent molecule, independently from the CMC, is a crucial advantage over the dialysis method. The removal of detergents like Triton TX-100 or DDM can be performed. Such “mild” detergents are widely used for the purification of large and sensitive complexes like *Chlorobium tepidum* reaction center (Remigy et al., 1999). The nature of the detergent, the detergent removal rate and the detergent

Please cite this article as: Gian A. Signorell et al., Controlled 2D crystallization of membrane proteins using methyl-β-cyclodextrin, Journal of Structural Biology (2006), doi:10.1016/j.jsb.2006.07.011

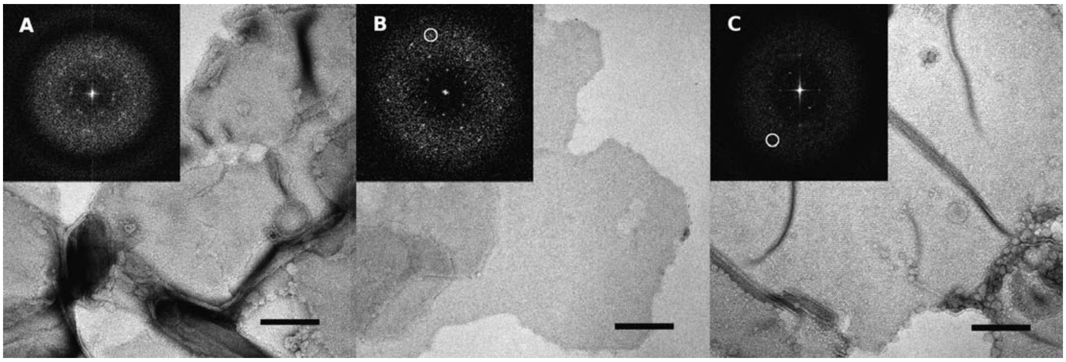

Fig. 2. OmpF 2D crystallization using the MBCD procedure. Experiments ranging from 30 min to 144 h show that (A) faster detergent removal rates (2 h and less) result in low quality crystals having diameters ranging from 50 to 500 nm, with a trigonal lattice ($a = b = 9 \pm 0.5$ nm; $\gamma = 60°$). (B) Slower rates (12–144 h) result in the formation of large sheets having a diameter ranging from 1 to 2 μm, with a trigonal lattice ($a = b = 9 \pm 0.5$ nm; $\gamma = 60°$) diffracting up to 2.4 nm resolution (spot marked by a circle). (C) After phospholipase A2 treatment on OmpF crystals obtained after a 144 h run, crystals with a trigonal lattice ($a = b = 7.2 \pm 0.2$ nm; $\gamma = 60°$) diffracting beyond 2.2 nm resolution were obtained (spot marked by a circle). The scale bars represent 100 nm.

removal technique affect size and quality of the resulting proteoliposomes and crystals (Wingfield et al., 1979; Hovmoller et al., 1983; Chami et al., 2001; Remigy et al., 2003). Even if the detergent is removed in an efficient way, there is no guarantee that 2D crystals will form during the reconstitution process. For this reasons the validation of the cyclodextrin approach in its ability to produce membrane protein crystals was needed.

4.1. Cyclodextrin and detergent removal

To perform reconstitution with MBCD accurately, a precise evaluation of the amount of MBCD needed to remove all the detergent from a solution is required. A homemade device (Kaufmann et al., 2006) to measure the detergent concentration of any solution (detergent solution, binary or ternary mixtures) was used to measure the MBCD–detergent molecular ratios after cyclodextrin addition to detergent solutions. The insets in Fig. 1 show the most probable complexes between MBCD and the detergents. The obtained ratios for OG (1:1), LDAO (1:1 and a weak 2:1) and Octyl-POE (2:1) are in good agreement with expected values based on the alkyl-chain length. The cavity of a β-cyclodextrin molecule is about 8 Å deep, offering accommodation for a C8 chain (Fig. 1A). The longer chain of LDAO might be shielded by an additional cyclodextrin ring occasionally forming a 2:1 complex (Fig. 1B). Alternatively a 3:2 complex could also be envisaged, where two LDAO molecules carry one MBCD each and an additional MBCD molecule is shared between the two. This, however, is purely speculative and might not be very probable for thermodynamic reasons. Octyl-POE has a lower stoichiometry than expected. One MBCD molecule is strung onto the C8 aliphatic chain, whereas only one more is occupying the polyethylene oxide (PEO) chain (Fig. 1C). The latter could reflect a lower affinity for PEO fragments due to the oxygen atoms possibly hydrogen bonding with surrounding water molecules. Thus, the change of free energy is lower for PEO units. However, the polydisperse character of Octyl-POE clearly interferes with the assignment of a single stoichiometric ratio and this might be reflected in the comparatively smaller gradient of the curve. Additionally, one should keep in mind that in solution both the aliphatic chains and the polyoxyethylene chains are not only present as an extended species and therefore the geometric reasoning is of approximative nature.

Schmidt-Krey et al. (1998) have shown that the size of microsomal glutathione transferase 2D crystals changes according to the initial detergent concentration. The MBCD approach allows us to use an excess of detergent even with low CMC detergents. Having established MBCD–detergent titration curves (Figs. 1A–C) we can calculate the exact amount of MBCD that needs to be added to a solution to remove all the detergent. For practical purposes one needs to add the highest molar ratio (see Section 3.1) since complete neutralization of the detergent is required. Also, since the detergent removal rate is directly related to the cyclodextrin addition, a mixture of detergents can be reproducibly used during crystallization. Hence, one can easily combine low and high CMC detergents without the drawbacks related to dialysis. This enables us to explore 2D crystallization conditions that could not be tested yet.

4.2. 2D Crystallization of OmpF

Using the cyclodextrin approach to remove detergent produced OmpF crystals of different qualities depending on the reconstitution time. Short reconstitution periods (up to 2 h) yielded low quality crystals (Fig. 2A) similar to the crystals reported by Dorset et al. (1983). Longer reconstitution experiments (12–144 h) led to bigger proteoliposomes having an average diameter of 1.5 μm that diffracted up to 2.4 nm (Fig. 2B). These results are in agreement (according to the size of the proteoliposomes and the lattice parameters) with previous works on OmpF (Dolder et al., 1996; Remigy et al., 2003) where dilution and dialysis yielded double-layered trigonal crystals. To improve the crystal packing of OmpF, we adapted the procedure using phospholipase A2 (PLA2) described by

Please cite this article as: Gian A. Signorell et al., Controlled 2D crystallization of membrane proteins using methyl-β-cyclodextrin, Journal of Structural Biology (2006), doi:10.1016/j.jsb.2006.07.011

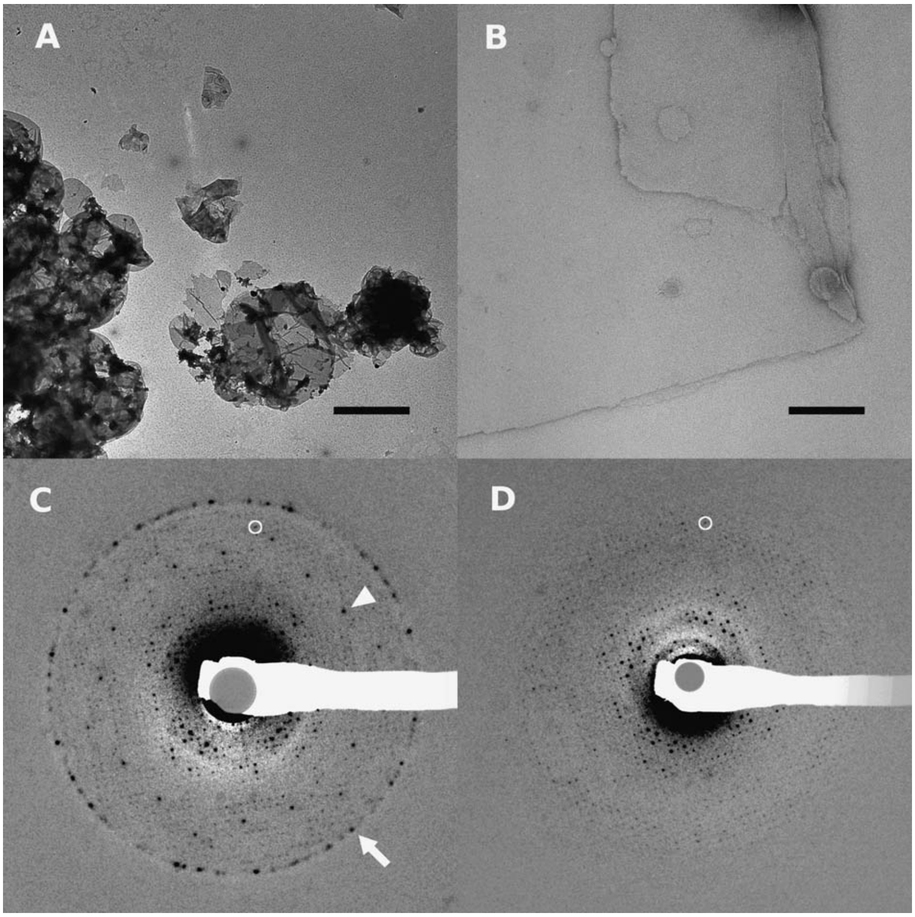

Fig. 3. SoPIP2;1 2D crystallization using MBCD. (A and B) Electron microscopy images using negative stain. (A) Overview at 5k magnification of a 2 h run and (B) sheet at 50k magnification of a crystal obtained after a 144 h reconstitution. The scale bar in (A) represents 1 μm and in (B) 100 nm. (C and D) Electron diffraction patterns of crystals obtained after 144 h. Both images show a p4 symmetry with lattice constants of $a = b = 96$ Å. (C) The unwashed sample shows strong additional diffraction spots arranged in a sixfold symmetry (arrowhead). The spots arranged in circle are from water crystals (arrow). The spot marked by a circle on the diffraction image is indexed 24,2. (D) The washed sample shows no additional spot overlaying the typical diffraction pattern of SoPIP2;1. The spot marked by a circle (24,3) corresponds to a resolution of 4 Å.

Mannella (1984) to the cyclodextrin method. PLA2 catalyzes the hydrolysis of the ester linkage in the sn-2 position of glycerophospholipids like DMPC, yielding free fatty acids and lysophospholipids. To avoid the solubilization of the proteoliposomes by these degradation products the solution is dialyzed against a low salt buffer (Mannella, 1984). The ability of cyclodextrin to bind free fatty acids and lysophospholipids allowed us to perform the PLA2 treatment without dialysis and thus to simplify the procedure. After PLA2 treatment the packing of the proteins was denser and a smaller trigonal lattice was revealed (Fig. 2C). These crystals are similar to the densely packed OmpF crystals that have undergone a PLA2 treatment described by Regenass et al. (1985) and Engel et al. (1992). Due to the limitations of negative staining these crystals diffracted only up to 2.2 nm (Fig. 2C). Thus PLA2 treatment can be applied directly on loosely packed crystals obtained with the MBCD method given that there is enough MBCD to capture the digested lipids. This approach is appropriate when the initial amount of lipid is higher than is optimal for crystallization. This can be required to keep the protein stable during the reconstitution step.

4.3. 2D Crystallization of SoPIP2;1

Reconstitutions of SoPIP2;1 lasting 2 h and less did not yield large sheets and did not diffract in negative stain (Fig. 3A). The weak contrast in negative stained samples is due to the smooth surface of double-layered SoPIP2;1 crystals preventing negative stain to penetrate (Kukulski, personal communication). Only cryo-EM could correctly assess the quality of such crystals. Reconstitutions of SoPIP2;1 over 144 h produced large crystals (Fig. 3B) so that electron diffraction could be performed. The diffraction patterns (Figs. 3C and D) correspond to one type of 2D crystal, obtained by dialysis during the determination of the 5 Å structure of SoPIP2;1 (Kukulski et al., 2005). The quality of the crystals in the present work is comparable, having spots diffracting up to a resolution of 4 Å. The unwashed sample (Fig. 3C) displays strong additional diffraction spots arranged in a sixfold symmetry and over-

Please cite this article as: Gian A. Signorell et al., Controlled 2D crystallization of membrane proteins using methyl-β-cyclodextrin, Journal of Structural Biology (2006), doi:10.1016/j.jsb.2006.07.011

laying the typical diffraction pattern of SoPIP2;1. These spots disappear when the sample is washed (Fig. 3D). Because washing mainly removed the MBCD from the solution, we assume that the spots in the unwashed sample result from MBCD crystallization during grid preparation.

4.4. Large screenings for 2D crystals using cyclodextrin

To parallelize 2D crystallization experiments to test as many conditions as possible, it is important to have the smallest possible initial volume of ternary mixtures. The accuracy in the addition of salts, lipids and other compounds imposes a limit in reducing this initial sample volume. Evaporation poses the problem of keeping the sample volume constant over long time spans, which is a difficult task to handle, especially with small volumes. Using microdroplet pipettes to dispense cyclodextrin solution and water in combination with an accurate volume measurement method could overcome these drawbacks. We estimate that small volumes in the order of 10 μl can be handled automatically. In this way up to 100 different reconstitution conditions could be tested with 1 mg of protein. This is a decisive step towards the reproducibility of 2D crystallization experiments. Still remaining is the problem of preparing and inspecting a large quantity of individual specimens by electron microscopy (Kuhlbrandt, 1992).

In our experiments crystallization mixtures were dialyzed overnight to have precise starting conditions. To diversify conditions (salts concentrations, LPRs etc.) it makes sense to dialyze batches of detergent–protein mixtures against buffers of various pHs overnight and to add subsequently additional substances to the solution (lipids, salts, inhibitors etc.).

Short experiments (12 h and less) yielded crystals of lower quality (small and less ordered), whereas large sheets were obtained after 72 h and more for both OmpF and SoPIP2;1. From these results we assume that longer duration will in general increase the size and the quality of the crystals. Also, over longer experiments (72 and 144 h) mixing did not affect crystal quality. To achieve homogeneous conditions over longer reconstitutions, a stirrer was used in our setup. In parallel experiments a shaker would be more appropriate, since shaking does not interfere with the sample directly (no contamination) and commercially available microplates (with 96 or 384 wells) could be used. A more sophisticated device than the dilution apparatus, controlling all pertinent parameters of the ternary mixture during crystallization would enable us to perform longer experiments promoting crystallogenesis in a reproducible manner.

The transition phase temperature increases according to the ratio of saturated/unsaturated fatty acid chains of lipids. Therefore, the temperature during reconstitution is a crucial parameter (Engel et al., 1992). For example, the phase transition temperature of DMPC, commonly used for crystallization, is beyond 23 °C (Nakayama et al., 1980). The effects of the temperature as parameter on the crystallization using cyclodextrins have not been investigated extensively. Since MBCD is highly soluble in water even at low temperatures, the described procedure shows no restriction in experimenting any temperature profiles during crystallization.

The reconstitution and crystallization using the cyclodextrin approach requires only small sample volumes and no additional surrounding buffer like in the dialysis method. This makes the cyclodextrin method very suitable to screen conditions where expensive or difficult to produce compounds are used (proteins, chemicals, substrates or inhibitors). A certain protein conformation or better-ordered crystals may be achieved if such compounds (ATP, antagonists or substrates) are added to the ternary mixture. In the dialysis method these compounds have to be added to the dialysis buffer solution to keep their concentrations constant since they are usually small enough to pass through the dialysis membrane. Many examples of co-crystallization in the 3D crystallization field involving inhibitors with high affinity, transiently bound substrates (e.g., NAD^+), designed protein (e.g., ankyrin repeats), or other cofactors have been reported (Schindler et al., 2000; Scott et al., 2004; Brautigam et al., 2005; Kohl et al., 2005; Sundaresan et al., 2005). Such conditions have not being explored by 2D crystallization because of the limitations mentioned above. Therefore, the cyclodextrin approach appears to be a promising alternative to traditional 2D crystallization methods.

5. Conclusion

Cyclodextrin can be used in protein reconstitution, crystallization and to improve crystal quality in combination with phospholipase. Proteins of known structure were chosen to test this new method of 2D crystallography. The quality of both OmpF and SoPIP2;1 crystals were comparable with previously published results (Dolder et al., 1996; Remigy et al., 2003; Kukulski et al., 2005). One advantage of this method is the accuracy of the detergent removal, allowing us to control the kinetics of the whole process in a precise way. The detergent removal rate is controlled by the amount of cyclodextrin added and therefore does not depend on the CMC of the detergent. Another advantage of the cyclodextrin method over other methods lies in its applicability in systematic screenings for crystallization conditions. The sample volume can be very small allowing to work with a small amount of protein per condition and with compounds that are expensive or not available in large quantities. The possibility of large parallel screenings of 2D crystallization conditions needs to be complemented with the effort to automate electron microscopy in such a way that all the conditions can be inspected in a reasonable time. The approach needs to be explored with a large range of membrane proteins in order to acquire a solid know-how of kinetics, choice of detergents and choice of the right cyclodextrin partner. Only these systematic experiments will give us the knowledge to produce 2D crystals of any membrane protein in a reproducible way.

Please cite this article as: Gian A. Signorell et al., Controlled 2D crystallization of membrane proteins using methyl-β-cyclodextrin, Journal of Structural Biology (2006), doi:10.1016/j.jsb.2006.07.011

Acknowledgments

We are grateful to Per Kjellbom for providing *Pichia pastoris* over-expressing SoPIP2;1 and Mohamed Chami for fruitful feedback on membrane protein reconstitution. Heiko Heerklotz is acknowledged for critically discussing the results of detergent complexation by MBCD. This work was supported by the NCCR Nano, the NCCR Structural Biology, the SNF grant to Andreas Engel (SNF 501 221) and the NoE 3DEM.

References

Brautigam, C.A., Chuang, J.L., Tomchick, D.R., Machius, M., Chuang, D.T., 2005. Crystal structure of human dihydrolipoamide dehydrogenase: NAD$^+$/NADH binding and the structural basis of disease-causing mutations. J. Mol. Biol. 350, 543–552.

Chami, M., Pehau-Arnaudet, G., Lambert, O., Ranck, J.L., Levy, D., Rigaud, J.L., 2001. Use of octyl-β-thioglucopyranoside in two-dimensional crystallization of membrane proteins. J. Struct. Biol. 133, 64–74.

Cowan, S.W., Schirmer, T., Rummel, G., Steiert, M., Ghosh, R., Pauptit, R.A., Jansonius, J.N., Rosenbusch, J.P., 1992. Crystal structures explain functional properties of two *E. Coli* porins. Nature 358, 727–733.

Degrip, W.J., Vanoostrum, J., Bovee-Geurts, P.H., 1998. Selective detergent-extraction from mixed detergent/lipid/protein micelles, using cyclodextrin inclusion compounds: a novel generic approach for the preparation of proteoliposomes. Biochem. J. 330, 667–674.

Dolder, M., Engel, A., Zulauf, M., 1996. The micelle to vesicle transition of lipids and detergents in the presence of a membrane protein: towards a rationale for 2D crystallization. FEBS Lett. 382, 203–208.

Dorset, D.L., Engel, A., Haner, M., Massalski, A., Rosenbusch, J.P., 1983. Two-dimensional crystal packing of matrix porin. A channel forming protein in *Escherichia coli* outer membranes. J. Mol. Biol. 165, 701–710.

Engel, A., Hoenger, A., Hefti, A., Henn, C., Ford, R.C., Kistler, J., Zulauf, M., 1992. Assembly of 2-D membrane protein crystals: dynamics, crystal order, and fidelity of structure analysis by electron microscopy. J. Struct. Biol. 109, 219–234.

Hasler, L., Heymann, J.B., Engel, A., Kistler, J., Walz, T., 1998. 2D crystallization of membrane proteins: rationales and examples. J. Struct. Biol. 121, 162–171.

Holzenburg, A., Engel, A., Kessler, R., Manz, H.J., Lustig, A., Aebi, U., 1989. Rapid isolation of OmpF porin-LPS complexes suitable for structure-function studies. Biochemistry 28, 4187–4193.

Hovmoller, S., Slaughter, M., Berriman, J., Karlsson, B., Weiss, H., Leonard, K., 1983. Structural studies of cytochrome reductase. Improved crystals of the enzyme complex and crystallization of a subcomplex. J. Mol. Biol. 165, 401–406.

Jap, B.K., Zulauf, M., Scheybani, T., Hefti, A., Baumeister, W., Aebi, W., Engel, A., 1992. 2D crystallization: from art to science. Ultramicroscopy 46, 45–84.

Karlsson, M., Fotiadis, D., Sjovall, S., Johansson, I., Hedfalk, K., Engel, A., Kjellbom, P., 2003. Reconstitution of water channel function of an aquaporin overexpressed and purified from Pichia pastoris. FEBS Lett. 537, 68–72.

Kaufmann, T.C., Engel, A., Remigy, H.W., 2006. A novel method for detergent concentration determination. Biophys. J. 90, 310–317.

Kohl, A., Amstutz, P., Parizek, P., Binz, H.K., Briand, C., Capitani, G., Forrer, P., Plückthun, A., Grütter, M., 2005. Allosteric inhibition of aminoglycoside phosphotransferase by a designed ankyrin repeat protein. Structure 13, 1131–1141.

Kuhlbrandt, W., 1992. Two-dimensional crystallization of membrane proteins. Q. Rev. Biophys. 25, 1–49.

Kukulski, W., Schenk, A.D., Johansson, U., Braun, T., de Groot, B.L., Fotiadis, D., Kjellbom, P., Engel, A., 2005. The 5Å structure of heterologously expressed plant aquaporin SoPIP2;1. J. Mol. Biol. 350, 611–616.

Mannella, C.A., 1984. Phospholipase-induced crystallization of channels in mitochondrial outer membranes. Science 224, 165–166.

Nakayama, A., Mitsui, T., Nishihara, M., Kito, M., 1980. Relation between growth temperature of *E. coli* and phase transition temperatures of its cytoplasmic and outer membranes. Biochim. Biophys. Acta 601, 1–10.

Regenass, M., Hardmeyer, A., Rosenbusch, J.P., Engel, A., 1985. Phospholipids in reconstituted porin membranes: conversion of one crystal habit in another by phospholipase. Experientia 41, 808.

Remigy, H.W., Stahlberg, H., Fotiadis, D., Müller, S.A., Wolpensinger, B., Engel, A., Hauska, G., Tsiotis, G., 1999. The reaction complex from the green sulfur bacterium *Chlorobium tepidum*: a structural analysis by scanning transmission electron microscopy. J. Mol. Biol. 290, 851–858.

Remigy, H.W., Caujolle-Bert, D., Suda, K., Schenk, A., Chami, M., Engel, A., 2003. Membrane protein reconstitution and crystallization by controlled dilution. FEBS Lett. 555, 160–169.

Rigaud, J.L., Mosser, G., Lacapere, J.J., Olofsson, A., Levy, D., Ranck, J.L., 1997. Bio-beads: an efficient strategy for two-dimensional crystallization of membrane proteins. J. Struct. Biol. 118, 226–235.

Rosenbusch, J.P., Lustig, A., Grabo, M., Zulauf, M., Regenass, M., 2001. Approaches to determining membrane protein structures to high resolution: do selections of subpopulations occur? Micron 32, 75–90.

Schindler, T., Bornmann, W., Pellicena, P., Miller, W.T., Clarkson, B., Kuriyan, J., 2000. Structural Mechanism for STI-571 inhibition of Abelson Tyrosine Kinase. Science 289, 1938–1942.

Schmidt-Krey, I., Lundqvist, G., Morgenstern, R., Hebert, H., 1998. Parameters for the two-dimensional crystallization of the membrane protein microsomal glutathione transferase. J. Struct. Biol. 123, 87–96.

Scott, E.E., White, M.A., He, Y.A., Johnson, E.F., Stout, C.D., Halpert, J.R., 2004. Structure of mammalian cytochrome P450 2B4 complexed with 4-(4-Chlorophenyl) imidazole at 1.9-Å resolution. J. Biol. Chem. 279, 27294–27301.

Sundaresan, V., Chartron, J., Yamaguchi, M., Stout, C.D., 2005. Conformational diversity in NAD(H) and interacting transhydrogenase nicotinamide nucleotide binding domains. J. Mol. Biol. 346, 617–629.

Tornroth-Horsefield, S., Wang, Y., Johanson, U., Karlsson, M., Tajkhoshid, D., Neutze, R., Kjellbom, P., 2005. Structural mechanism of plant aquaporin gating. Nature 439, 688–694.

Turk, E., Kim, O., le Coutre, J., Whitelegge, J.P., Eskandari, S., Lam, J.T., Kreman, M., Zampighi, G., Faull, K.F., Wright, E.M., 2000. Molecular characterization of *Vibrio parahaemolyticus* vSGLT: a model for sodium-coupled sugar cotransporters. J. Biol. Chem. 275, 25711–25716.

Wingfield, P., Arad, T., Leonard, K., Weiss, H., 1979. Membrane crystals of ubiquinone: cytochrome c reductase from *Neurospora* mitochondria. Nature 280, 696–697.

Zampighi, G.A., Kreman, M., Lanzavecchia, S., Turk, E., Eskandari, S., Zampighi, L., Wright, E.M., 2003. Structure of functional single AQP0 channels in phospholipid membranes. J. Mol. Biol. 325, 201–210.

Please cite this article as: Gian A. Signorell et al., Controlled 2D crystallization of membrane proteins using methyl-β-cyclodextrin, Journal of Structural Biology (2006), doi:10.1016/j.jsb.2006.07.011

Abbreviations

2D Two Dimensional
3D Three Dimensional
8-POE Octyl Polydisperse Oligooxyethylene
AFM Atomic Force Microscope
AOX1 Alcohol Oxidase 1
ATP Adenosine Tri-Phosphate
AQP Aquaporin
AqpZ Aquaporin Z from *Escherichia coli*
BCA Bicinchoninic Acid
Bicine *N,N*-bis(2-hydrocyethyl)glycine
BMGY Buffered Glycerol-complex Medium
BMMY Buffered Methanol-complex Medium
BSA Bovine Serum Albumine
CCD Charge Coupled Device
CDPK Calcium Dependent Protein Kinase
CHAPS 3-[(3-cholamidopropyl)-demethylammonio]-1-propanesulfonate
CHIP Channel-forming Integral Protein
Ci Curie
CMC Critical Micelle Concentration
DAG Diacyl-glycerol
DDM n-Dodecyl-β-D-maltopyranoside
DM n-Decyl-β-D-maltopyranoside
DMPC 1,2-Dimyristoyl-sn-Glycero-3-Phosphocholine
DMSO 3-[(3-cholamidopropyl)-demethylammonio]-1-propanesulfonate
DOPC 1,2-Dioleoyl-sn-Glycero-3-Phosphocholine
DOPG 1-Palmitoyl-2-Oleoyl-sn-Glycero-3-[Phospho-rac-(1-glycerol)]
DOPS 1,2-Dioleoyl-sn-Glycero-3-[Phospho-L-Serine]
DTT Dithiothreitol
EDTA Ethyl-n-diamin-tetraacetat
EGTA Ethyleneglycol-bis(2-amineethyl)-N,N,N',N'-tetraacetic acid
EM Electron Microscopy
EO Ethoxylated
ESI-MS Electrospray Ionization - Mass Spectroscopy

FEG Field Emission Gun

FFT Fast Fourier Transform

GFP Green Fluorescent Protein

GLP Glyceroporin

GlpF Glycerol facilitator from *Escherichia coli*

HPLC High Pressure Liquid Chromatography

IPLT Image Processing Library and Toolkit

kDa kilo Dalton

LB Luria Bertani

LC-MS Liquid Chromatography - Mass Spectroscopy

LDAO Lauryldimethylamine-oxide

LPR Lipid-to-Protein Ratio

MALDI-TOF Matrix-Assisted Laser Desorption Ionization - Time Of Flight

MAP kinase Mitogen-activated protein kinases

MBCD Methyl-β-cyclodextrin

MD Molecular Dynamics

MES 2-(*N*-morpholino)ethanesulfonic acid

MIP Major Intrinsic Protein

MRC Medical Research Council

MS Mass Spectrometry

MW Molecular Weight

NG n-Nonyl-β-D-glyopyronaoside

NAD$^+$ Nicotinamide Adenine Dinucleotide

NiNTA Ni^{++}-Nitrilotriacetic acid

NIP Noduline-like Intrinsic Protein

NPA Asparagine - Proline - Alanine

Octyl-POE Octyl Polydisperse Oligooxyethylene

OD Optical Density

OG n-Octyl-β-D-glycopyranoside

OmpF Outer Membrane Porin F

OTG n-Octyl 1-β-D-glycopyranoside

PAGE Polyacrylamide gel electrophoresis

PCR Polymerase Chain Reaction

PEO Polyethylene Oxide

PIP Plasma Membrane Intrinsic Protein

PKA Protein Kinase A

PKC Protein Kinase C

PLA2 Phospholipase A2

PM28A Plasma Membrane 28kDa protein A from *Spinacia oleracea*

PMSF Phenylmethylsulfonylfluoride

POPC	1-Palmitoyl-2-Oleoyl-sn-Glycero-3-Phosphocholine
POPG	1-Palmitoyl-2-Oleoyl-sn-Glycero-3-[Phospho-rac-(1-glycerol)]
POPS	1-Palmitoyl-2-Oleoyl-sn-Glycero-3-[Phospho-L-Serine]
ppm	Pixel Per Millimeter
RT	Room Temperature
SDS	Sodium-dodecyle sulfate
SIP	Small Intrinsic Protein
SNR	Signal-to-Noise ratio
SOC	Super Optimal Broth with Catabolite repression
SoPIP2;1	*Spinacia oleracea* Plasma Membrane Intrinsic Protein 2;1
STEM	Scanning Transmission Electron Microscope
TEM	Transmission Electron Microscope
TFA	Trifluoroacetic Acid
TIP	Tonoplast Intrinsic Protein
Tris	Tis(hydoxymethyl)-aminoethane
Triton X-100	Polyethylene glycol-p-isooctylphenylether
UDM	Undecyl-β-D-maltopyranoside
YPD	Yeast Peptone Dextrose

Bibliography

[1] S. J. Singer and G. L. Nicholson. The fluid mosaic model of the structure of cell membranes. *Science*, 175:720–731, 1972.

[2] D. M. Engelman. Membranes are more mosaic than fluid. *Nature*, 438:578–580, 2005.

[3] B. J. Heymann and A. Engel. Aquaporins: Phylogeny, structure, and physiology of water channels. *News Physiol. Sci.*, 14:187–193, 1999.

[4] R. I. Macey. Transport of water and urea in red blood cells. *American Journal of Physiology*, 246:195–203, 1984.

[5] G. M. Preston, T. P. Carroll, W. B. Guggino, and P. Agre. Appearance of water channels in *Xenopus* oocytes expressing red cell CHIP28 protein. *Science*, 256:385–387, 1992.

[6] J. S. Jung, G. M. Preston, B. L. Smith, W. B. Guggino, and P. Agre. Molecular structure of the water channel through aquaporin CHIP. The hourglass model. *The Journal of Biological Chemistry*, 269:14648–14654, 1994.

[7] G. M. Pao, L. F. Wu, K. D. Johnson, H. Hofte, M. J. Chrispeels, G. Sweet, N. N. Sandal, and M. H. Jr. Saier. Evolution of the MIP family of integral membrane proteins. *Mol Microbiol.*, 1:33–37, 1991.

[8] G. M. Preston, J. S. Jung, W. B. Guggino, and P. Agre. The mercury-sensitive residue at cysteine 189 in the CHIP28 water channel. *Journal of Biological Chemistry*, 268:17–20, 1993.

[9] T. Walz, T. Hirai, K. Murata, B. J. Heymann, K. Mitsuoka, Y. Fujiyoshi, B. L. Smith, P. Agre, and A. Engel. The three-dimensional structure of Aquaporin-1. *Nature*, 387:624–627, 1997.

[10] K. Mitsuoka, K. Murata, T. Walz, T. Hirai, P. Agre, J. B. Heymann, A. Engel, and Y. Fujiyoshi. The structure of aquaporin-1 at 4.5 å resolution reveals short α-helices in the center of the monomer. *Journal of Structural Biology*, 128:34–43, 1999.

[11] B. L. de Groot, B. J. Heymann, A. Engel, K. Mitsuoka, Y. Fujiyoshi, and H. Grubmüller. The fold of human Aquaporin 1. *Journal of Molecular Biology*, 300:987–994, 2000.

[12] K. Murata, K. Mitsuoka, T. Hirai, T.and Walz, P. Agre, J. B. Heymann, A. Engel, and F. Yoshinori. Structural determinants of water permeation through Aquaporin-1. *Nature*, 407:605–612, 2000.

[13] B. L. de Groot, A. Engel, and H. Grubmüller. A refined structure of human Aquaporin-1. *FEBS Letters*, 504:206–211, 2001.

[14] B. L. de Groot and H. Grubmüller. Water permeation across biological membranes: Mechanism and dynamics of Aquaporin-1 and GlpF. *Science*, 294:2353–2357, 2001.

[15] B. L. de Groot, T. Frigato, V. Helms, and H. Grubmüller. The mechanism of proton exclusion in the Aquaporin-1 water channel. *Journal of Molecular Biology*, 333:279–293, 2003.

[16] B. L. de Groot and H. Grubmüller. The dynamics and energetics of water permeation and proton exclusion in aquaporins. *Current Opinion in Structural Biology*, 15:176–183, 2005.

[17] D. Fu, A. Libson, L. J. W. Miercke, C. Weitzman, P. Nollert, J. Krucinski, and R. M. Stroud. Structure of a glycerol conducting channel and the basis for its selectivity. *Science*, 290:481–486, 2000.

[18] H. Stahlberg, T. Braun, B. de Groot, A. Philippsen, M. J. Borgnia, P. Agre, W. Kühlbrandt, and A. Engel. The 6.9-å structure of GlpF: A basis for homology modelling of the glycerol channel from *Escherichia coli*. *Journal of Structural Biology*, 132:133–141, 2000.

[19] D. F. Savage, P. F. Egea, Y. Robles-Colmenares, J. D. III O'Connell, and R. M. Stroud. Architecture and selectivity in aquaporins: 2.5 Å x-ray structure of Aquaporin Z. *PloS Biology*, 1:334–340, 2003.

[20] A. D. Schenk, P. J. L. Werten, S. Scheuring, B. L. de Groot, S. A. Müller, H. Stahlberg, A. Philippsen, and A. Engel. The 4.5 Å structure of human AQP2. *Journal of Molecular Biology*, 350:278–289, 2005.

[21] Y. Hiroaki, K.i Tani, A. Kamegawa, N. Gyobu, K. Nishikawa, H. Suzuki, T. Walz, S. Sasaki, K. Mitsuoka, K. Kimura, A. Mizoguchi, and Y. Fujiyoshi. Implications of the Aquaporin-4 structure on array formation and cell adhesion. *Journal of Molecular Biology*, 355:628–639, 2005.

[22] T. Gonen, P. Sliz, J. Kistler, Y. Cheng, and T. Walz. Aquaporin-0 membrane junctions reveal the structure of a closed water pore. *Nature*, 429:193–197, 2004.

[23] T. Gonen, Y. Cheng, P. Sliz, Y. Hiroaki, Y. Fujiyoshi, S. C. Harrison, and T. Walz. Lipid-protein interactions in double-layered two-dimensional AQP0 crystals. *Nature*, 438:633–638, 2005.

[24] S. Nielsen, J. Frokiaer, and M. A. Knepper. Renal aquaporins: Key roles in water balance and water balance disorders. *Curr. Opin. Nephrol. Hypertens.*, 6:367–371, 1998.

[25] M. L. Elkjaer, L. N. Nejsum, V. Gresz, T.-H. Kwon, U. B. Jensen, J. Frøkiaer, and S. Nielsen. Immunolocalization of Aquaporin-8 in rat kidney, gastrointestinal tract, testis and airways. *Am J Physiol Renal Physiol*, 281:F1047–F1057, 2001.

[26] M. Yasui, Hazama A., T. H. Kwon, S. Nielsen, W. B. Guggino, and P. Agre. Rapid gating and anion permeability of an intracellular aquaporin. *Nature*, 402:184–187, 1999.

[27] D. Ferri, G. E. Mazzone, A. Liquori, G. Cassano, M. Svelto, and G. Calamita. Ontogeny, distribution, and possible functional implications of an unusual aquaporin, AQP8, in mouse liver. *Hepatology*, 38:947–957, 2003.

[28] K. Ishibashi, S. Sasaki, K. Fushimi, S. Uchida, M. Kuwahara, H. Saito, T. Furukawa, K. Nakajima, Y. Yamaguchi, and T. Gojobori. Molecular cloning and expression of a member of the aquaporin family with permeability to glycerol and urea in addition to water expressed at the basolateral membrane of kidney collecting duct cells. *PNAS*, 14:6269–6273, 1994.

[29] G. Fruehbeck. Obesity: Aquaporin enters the picture. *Nature*, 438:436–437, 2005.

[30] J. M. Carbrey, D. A. Gorelick-Feldman, D. Kozono, J. Praetorius, S. Nielsen, and P. Agre. Aquaglyceroporin AQP9: solute permeation and metabolic control of expression in liver. *PNAS*, 100:2945–2950, 2003.

[31] K. Ishibashi, T. Morinaga, M. Kuwahara, S. Sasaki, and M. Imai. Cloning and identification of a new member of water channel (AQP10) as an aquaglyceroporin. *Biochimica et Biophysica Acta*, 1576:335–340, 2002.

[32] S. Hatakeyama, Y. Yoshida, T. Tani, Y. Koyama, K. Nihei, K. Ohshiro, J.-I. Kamiie, E. Yaoita, T. Suda, K. Hatakeyama, and T. Yamamoto. Cloning of a new aquaporin (AQP10) abundantly expressed in duodenum and jejunum. *Biochem Biophys Res Commun.*, 287:814–819, 2001.

[33] D. A. Gorelick, J. Praetorius, T. Tsunenari, S. Nielsen, and P. Agre. Aquaporin-11: A channel protein lacking apparent transport function expressed in brain. *BMC Biochem.*, 7:1–14, 2006.

[34] T. Itoh, T. Rai, M. Kuwahara, S. Ko, S. Uchida, S.and Sasaki, and K. Ishibashi. Identification of a novel aquaporin, AQP12, expressed in pancreatic acinar cells. *Biochemical and Biophysical Research Communications*, 330:832–838, 2005.

[35] U. Johanson, M. Karlsson, I. Johansson, S. Gustavsson, S. Sjovall, L. Fraysse, A. R. Weig, and P. Kjellbom. The complete set of genes encoding major intrinsic proteins in Arabidopsis provides a framework for a new nomenclature for major intrinsic proteins in plants. *Plant Physiology*, 126:1358–1369, 2001.

[36] F. Chaumont, F. Barrieu, E. Wojcik, M. J. Chrispeels, and R. Jung. Aquaporins constitute a large and highly divergent protein family in maize. *Plant Physiology*, 125:1206–1215, 2001.

[37] P. Gerbeau, J. Güclü, P. Ripoche, and C. Maurel. Aquaporin Nt-TIPa can account for the high permeability of tobacco cell vacuolar membrane to small neutral solutes. *The Plant Journal*, 18:577–587, 1999.

[38] L. M. Holm, T. P. Jahn, A. L. Moller, J. K. Schjoerring, D. Ferri, D. A. Klaerke, and T. Zeuthen. NH(3) and NH(4)(+) permeability in aquaporin-expressing *Xenopus* oocytes. *Pflugers Arch.*, 450:415–428, 2005.

[39] C. Maurel, R. T. Kado, J. Guern, and M. J. Chrispeels. Phosphorylation regulates the water channel activity of the seed-specific aquaporin α-TIP. *EMBO Journal*, 14:3028–3035, 1995.

[40] M. J. Daniels and M. Yeager. Phosphorylation of aquaporin PvTIP3;1 defined by mass spectrometry and molecular modeling. *Biochemistry*, 44, 2005.

[41] M. G. Fortin, N. A. Morrison, and D. P. S. Verma. Nodulin-26, a peribacteroid membrane nodulin is expressed independently of the development of the peribacteroid compartment. *Nucleic Acids Research*, 15:813–824, 1987.

[42] S. Biswas. Functional properties of soybean nodulin 26 from a comparative three-dimensional model. *FEBS Lett.*, 558:39–44, 2004.

[43] U. Johanson and S. Gustavsson. A new subfamily of intrinsic proteins in plants. *Mol Biol Evol.*, 19:456–461, 2002.

[44] F. Ishikawa, S. Suga, T. Uemura, M. H. Sato, and M. Maeshima. Novel type of aquaporin SIPs are mainly localized to the ER membrane and show cell-specific expression in Aradopsis thaliana. *FEBS Lett.*, 579, 2005.

[45] F. Chaumont, F. Barrieu, R. Jung, and M. J. Chrispeels. Plasma membrane intrinsic proteins from maize cluster in two sequence subgroups with differential aquaporin activity. *Plant Physiology*, 122:1025–1034, 2000.

[46] A. Biela, K. Grote, B. Otto, S. Hoth, R. Hedrich, and R. Kaldenhoff. The nicotiana tabacum plasma membrane aquaporin NtAQP1 is mercury-insensitive and permeable for glycerol. *Plant Journal*, 18:565–570, 1999.

[47] M. Moshelion, D. Becker, A. Biela, Uehlein N., R. Hedrich, B. Otto, H. Levi, N. Moran, and R. Kaldenhoff. Plasma membrane aquaporins in the motor cells of samanea saman: diurnal and circadian regulation. *Plant Cell*, 14:727–739, 2002.

[48] I. Johansson, B. Larsson, C.and Ek, and P. Kjellbom. The major integral proteins of spinach leaf plasma membranes are putative aquaporins and are phosphorylated in response to Ca^{2+} and apoplastic water potential. *The Plant Cell*, 8:1181–1191, 1996.

[49] I. Johansson, M. Karlsson, V. K. Shukla, M. J. Chrispeels, C. Larsson, and P. Kjellbom. Water transport activity of the plasma membrane aquaporin PM28A is regulated by phosphorylation. *The Plant Cell*, 10:451–459, 1998.

[50] C. Tournaire-Roux, M. Sutka, H. Javot, E. Gout, P. Gerbeau, D.-T. Luu, R. Bligny, and C. Maurel. Cytosolic pH regulates root water transport during anoxic stress through gating of aquaporins. *Nature*, 425:393–397, 2003.

[51] P. Kjellbom, C. Larsson, I. Johansson, M. Karlsson, and U. Johanson. Aquaporins and water homeostasis in plants. *Trends Plant Sci.*, 4:308–314, 1999.

[52] H. Sui, B.-G. Han, J. K. Lee, P. Walian, and B. K. Jap. Structural basis of water-specific transport through AQP1 water channel. *Nature*, 414:872–878, 2001.

[53] W. E. C. Harries, D. Akhavan, L. J. W. Miercke, S. Khademi, and R. M. Stroud. The channel architecture of Aquaporin 0 at a 2.2-Å resolution. *Proc Natl Acad Sci USA*, 101:14045–14050, 2004.

[54] E. Tajkhorshid, P. Nollert, M. Ø. Jensen, L. J. W. Miercke, J. O'Connell, R. M. Stroud, and K. Schulten. Control of the selectivity of the aquaporin water channel family by global orientational tuning. *Science*, 296:525–530, 2002.

[55] N. Chakrabarti, E. Tajkhorshid, B. Roux, and R. Pomes. Molecular basis of proton blockage in aquaporins. *Structure*, 12:65–74, 2004.

[56] N. Chakrabarti, B. Roux, and R. Pomes. Structural determinants of proton blockage in aquaporins. *Journal of Molecular Biology*, 343:493–510, 2004.

[57] M. Karlsson, D. Fotiadis, S. Sjövall, I. Johansson, K. Hedfalk, A. Engel, and P. Kjellbom. Reconstitution of water channel function of an aquaporin overexpressed and purified from *Pichia pastoris*. *FEBS Letters*, 537:68–72, 2003.

[58] T. Gonen, Y. Cheng, J. Kistler, and T. Walz. Aquaporin-0 membrane junctions form upon proteolytic cleavage. *Journal of Molecular Biology*, 342:1337–1345, 2004.

[59] K. L. Németh-Cahalan and J. E. Hall. pH and calcium regulate the water permeability of Aquaporin 0. *The Journal of Biological Chemistry*, 275:6777–6782, 2000.

[60] T. Zeuthen and D. A. Klaerke. Transport of water and glycerol in Aquaporin 3 is gated by H^+. *Journal of Biological Chemistry*, 274:21632–21636, 1999.

[61] S. Törnroth-Horsefield, Y. Wang, K. Hedfalk, U. Johanson, M. Karlsson, E. Tajkhorshid, R. Neutze, and P. Kjellbom. Structural mechanism of plant aquaporin gating. *Nature*, 439:488–494, 2006.

[62] P. Gerbeau, G. Amodeo, T. Henzler, V. Santoni, P. Ripoche, and C. Maurel. Water permeability of *arabidopsis* plasma membrane is regulated by divalent cations and pH. *The Plant Journal*, 30:71–81, 2001.

[63] D. Fotiadis, P. Jenö, T. Mini, S. Wirtz, S. A. Müller, L. Fraysse, P. Kjellbom, and A. Engel. Structural characterization of two aquaporins isolated from native spinach leaf plasma membranes. *The Journal of Biological Chemistry*, 276(3):1707–1714, 2001.

[64] W. Kukulski. Purification, 2D-crystallization and electron microscopy of the plant aquaporin PM28A. Diploma thesis, 2002.

[65] B. K. Jap, M. Zulauf, T. Scheybani, A. Hefti, W. Baumeister, U. Aebi, and A. Engel. 2D crystallization: From art to science. *Ultramicroscopy*, 46:45–84, 1992.

[66] D. Fotiadis, L. Hasler, D. J. Müller, H. Stahlberg, J. Kistler, and A. Engel. Surface tongue-and-groove contours on lens MIP facilitate cell-cell adherence. *Journal of Molecular Biology*, 300:779–789, 2000.

[67] W. Chiu and R. M. Glaeser. Evaluation of photographic emulsions for low-exposure imaging. *Electron Microscopy at Molecular Dimensions, Springer Verlag*, pages 194–199, 1980.

[68] A. Philippsen, A. D. Schenk, G. A. Signorell, V. Mariani, S. Berneche, and A. Engel. Collaborative EM image processing with the IPLT processing library and toolbox. *Journal of Structural Biology*, 2006.

[69] A. D. Wegener and L. R. Jones. Phosphorylation-induced mobility shift in phospholamban in sodium dodecyl-polyacrylamide gels. *The Journal of Biological Chemistry*, 258:1834–1841, 1984.

[70] S. Aoufouchi and S. Shall. Regulation by phosphorylation of *Xenopus laevis* poly(adp-ribose) polymerase enzyme activity during oocyte maturation. *Biochemical Journal*, 325:543–551, 1997.

[71] K.-S. Park, D. P. Mohapatra, H. Misonou, and J. S. Trimmer. Graded regulation of the Kv2.1 potassium channel by variable phosphorylation. *Science*, 313:976 – 979, 2006.

[72] M. Li, R. Cornea, J. M. Autry, L. R. Jones, and D. D. Thomas. Phosphorylation-induced structural change in phospholamban and its mutants, detected by intrinsic fluorescence. *Biochemistry*, 37:7869–7877, 1998.

[73] S. Ohno and K. Suzuki. Protein kinase C (vertebrates). *The Protein Kinase Facts Book, G. Hardie and S. Hanks, eds (London: Academic Press)*, pages 80 –88, 1995.

[74] P. J. Kennelly and E. G. Krebs. Consensus sequences as substrate specificity determinants for protein kinases and protein phosphatases. *Journal of Biological Chemistry*, 266:15555–15556, 1991.

[75] C. C. Wu, M. J. MacCoss, K. E. Howell, and J. R. Yates III. A method for the comprehensive proteomic analysis of membrane proteins. *Nature Biotechnology*, 21:532 – 538, 2003.

[76] V. Laizé, P. Ripoche, and F. Tacnet. Purification and functional reconstitution fo the human CHIP28 water channel expressed in *S*accharomyces cerevisiae. *Protein Expression and Purification*, 11:284–288, 1997.

[77] P. J. L. Werten, L. Hasler, J. B. Koenderink, C. H. W. Klaassen, W. J. de Grip, A. Engel, and P. M. T. Deen. Large-scale purification of functional recombinant human aquaporin-2. *FEBS Letters*, 504:200–205, 2001.

[78] R. C. Ford, A. Hefti, and A. Engel. Ordered arrays of the photosystem I reaction centre after reconstitution: projections and surface reliefs of the complex at 2 nm resolution. *EMBO Journal*, 9:3067–3075, 1990.

[79] P. D. Lampe, J. Kistler, A. Hefti, J. Bond, S. Muller, R. G. Johnson, and A. Engel. In vitro assembly of gap junctions. *Journal of Structural Biology*, 107:281–290, 1991.

[80] J. Zhuang, A. Engel, J. M. Pages, and J. M. Bolla. The campylobacter jejuni porin trimers pack into different lattice types when reconstituted in the presence of lipid. *European J Biochem.*, 244:575–579, 1997.

[81] D. G. Robinson, H. Sieber, W. Kammerloher, and A. R. Schäffner. PIP1 aquaporins are concentrated in plasmalemmasomes of *Arabidopsis thaliana* mesophyll. *Plant Physiology*, 111:645–649, 1996.

[82] S. Sjövall-Larsen, E. Alexandersson, I. Johansson, M. Karlsson, U. Johanson, and P. Kjellbom. Purification and characterization of two protein kinases acting on the aquaporin SoPIP2;1. *Biochimica and Biophysica Acta*, 2006.

[83] N. Gyobu, K. Tani, Y. Hiroaki, A. Kamegawa, K. Mitsuoka, and Y. Fujiyoshi. Improved specimen preparation for cryo-electron microscopy using a symmetric carbon sandwich technique. *Journal of Structural Biology*, 146:325–333, 2004.

[84] H. J. Butt, Wang D. N., P. K. Hansma, and W. Kühlbrandt. Effect of surface roughness of carbon support films on high-resolution electron diffraction of two-dimensional crystals. *Ultramicroscopy*, 36:307–318, 1991.

[85] R. M. Glaeser. Specimen flatness of thin crystalline arrays: Influence of the substrate. *Ultramicroscopy*, 46:33–44, 1992.

[86] R. A. Crowther, R. Henderson, and J. M. Smith. MRC image processing programs. *Journal of Stuctural Biology*, 116:9–16, 1996.

[87] M. L. Zeidel, S. V. Ambudkar, B. L. Smith, and P. Agre. Reconstitution of functional water channels in liposomes containing purified red cell CHIP28 protein. *Biochemistry*, 31:7436–7440, 1992.

[88] V. Laizé, G. Rousselet, J.-M. Verbavatz, V. Berthonaud, R. Gobin, N. Roudier, L. Abrami, P. Ripoche, and F. Tacnet. Functional expression of the human CHIP28 water channel in a yeast secretory mutant. *FEBS letters*, 373:269–274, 1995.

[89] M. J. Daniels, M. R. Wood, and M. Yeager. In vivo functional assay of a recombinant aquaporin in *Pichia pastoris*. *Appl Environ Microbiol.*, 72:1507–1514, 2006.

[90] G. White, K. I Racher, A. Lipski, F. R. Hallett, and J. M. Wood. Physical properties of liposomes and proteoliposomes prepared from *Escherichia coli* polar lipids. *Biochimica and Biophysica Acta*, 1468:175–186, 2000.

[91] M. L. Zeidel, S. Nielsen, B. L. Smith, S. V. Ambudkar, A. B. Maunsbach, and P. Agre. Ultrastructure, pharmacologic inhibition, and transport selectivity of aquaporin channel-forming integral protein in proteoliposomes. *Biochemistry*, 33:1606–1615, 1994.

[92] L. Hasler, T. Walz, P. Tittman, H. Gross, J. Kistler, and A. Engel. Purified lens major intrinsic (MIP) forms highly ordered tetragonal two-dimensional arrays by reconstitution. *Journal of Molecular Biology*, 279:855–864, 1998.

[93] Y. Koyama, K. Ishibashi, M. Kuwahara, N. Inase, M. Ichioka, S. Sasaki, and F. Marumo. Cloning and functional expression of human Aquaporin 8 cDNA and analysis of its gene. *Genomics*, 54:169–172, 1998.

[94] K. Ishibashi, M. Kuwahara, A. Kageyama, F. Marumo, and S. Sasaki. Cloning and functional expression of a second new aquaporin abundantly expressed in testis. *Biochem Biophys Res Commun.*, 237:714–718, 1997.

[95] Y. Koyama, T. Yamamoto, D. Kondo, H. Funaki, E. Yaoita, K.i Kawasaki, N. Sato, K. Hatakeyama, and I. Kihara. Molecular cloning of a new aquaporin from rat pancreas and liver. *Journal of Biological Chemistry*, 272:30329–30333, 1997.

[96] T. Ma, B. Yang, and A. S. Verkman. Cloning of a novel water and urea-permeable aquaporin from mouse expressed strongly in colon, placenta, liver and heart. *Biochem Biophys Res Commun.*, 240:324–328, 1997.

[97] F. Garcia, A. Kierbel, M. C. Larocca, S. A. Gradilone, P. Splinter, N. F. LaRusso, and R. A. Marinelli. The water channel Aquaporin-8 is mainly intracellular in rat hepatocytes, and its plasma membrane insertion is stimulated by cyclic AMP. *Journal of Biological Chemistry*, 276:12147–12152, 2001.

[98] B. Yang, Y. Song, D. Zhao, and Verkman A. S. Phenotype analysis of Aquaporin-8 null mice. *Am J Physiol Cell Physiol*, 288:1161–1170, 2005.

[99] B. Yang, D. Zhao, and A. S. Verkman. Evidence against functionally significant aquaporin expression in mitochondria. *Journal of Biological Chemistry*, 281:16202–16206, 2006.

[100] D. Levy, M. Chami, and J.-L. Rigaud. Two-dimensional crystallization of membrane proteins: The lipid layer strategy. *FEBS*, 504:187–193, 2001.

[101] T. Walz, B. L. Smith, P. Agre, and A. Engel. The three-dimensional structure of erythrocyte aquaporin CHIP. *The EMBO Journal*, 13:2985–2993, 1994.

[102] P. Ringler, M. J. Borgnia, H. Stahlberg, P.C. Maloney, P. Agre, and A. Engel. Structure of the water channel AqpZ from *Escherichia coli* revealed by electron crystallography. *Journal of Molecular Biology*, 291:1181–1190, 1999.

[103] T. Braun, A. Philippsen, S. Wirtz, M. J. Borgnia, P. Agre, W. Külbrandt, A. Engel, and H. Stahlberg. The 3.7 Å projection map of the glycerol facilitator GlpF: A variant of the aquaporin tetramer. *EMBO Reports*, 1:183–189, 2000.

[104] M. J. Daniels, M. J. Chrispeels, and M. Yeager. Projection structure of a plant vacuole aquaporin by electron cryo-crystallography. *Journal of Molecular Biology*, 294:1337–1349, 1999.

Acknowledgements

Many thanks to ...

Andreas Engel for giving me the possibility to do my PhD in his group. Thank you for teaching me to persistently keep track and not to give up despite keen competition!

Thomas Braun, my supervisor in the starting time, for always having time to solve a problem and for helpful advice in all kinds of situations.

Mohamed Chami for sharing his enormous experience and knowledge about electron microscopy. Your patience and dedication to science impresses me a lot.

Kitaru Suda for incomparable advice in biochemical and technical questions. I keep asking myself how we all will get along when you leave the lab!

Myriam Duckely for help during the expression project. I was glad to be your molecular biology student.

Hervé Rémigy for involving me into the MBCD project! It is always impressing to see how your machines become alive.

Ansgar Philippsen and Andreas Schenk for help with the image processing and all related software problems.

Nora Eifler for help with the stopped flow measurement. But particularly thank you for your friendship.

Thomas K, Marco and the whole Engel group for the great atmosphere and the fruitful discussions!

I would also like to thank Per Kjellbom for being co-referee of my thesis and for the long lasting collaboration. Thanks also to Maria, Mia and Erik!

This thesis is dedicated to my parents, my brother and Steffen. For your love and support and for believing in me.

Curriculum Vitae

Wanda Kukulski

Date of birth: 15.03.1979

Place of birth: Katowice, Poland

Nationalites: Swiss, Polish

Education

1985 - 1993 Primar- and Sekundarschule, Visp, Switzerland

1993 - 1998 Kollegium Spiritus Sanctus, Brig, Switzerland: Matura Typus D

1998 - 2002 Studies in Biology II, University of Basel, Switzerland. Diploma thesis: Purification, 2D-Crystallization and Electron Microscopy of the Plant Aquaporin PM28A. In the group of Prof. A. Engel.

2002 - present PhD thesis, University of Basel, Switzerland. Title: Structure and Function of Aquaporins. Supervised by Prof. Andreas Engel.

Courses

2002 NCCR Course: " Protein Biochemistry" ETH Hoenggerberg, Zurich, Switzerland
EMBO Course: "Cryo-Electron Microscopy and 3-D Image Reconstruction" EMBL Heidelberg, Germany

Teaching

2002 Instructor in the "Blockkurs in Biophysik und Strukturbiologie" in the image processing and electron crystallography exercises.
Instructor in the "Blockkurs in Biophysik und Strukturbiologie" in the laboratory week course.
Tutoring "Uebungen zu Grundlagen der Biologie" for undergraduate students at the University of Basel, Switzerland.

2003 Instructor in the "Blockkurs in Biophysik und Strukturbiologie" in the image processing and electron crystallography exercises.
Tutoring in "Grundlagen der Ethik" for undergraduate students at the University of Basel, Switzerland.

2004 Instructor at the 3rd NCCR Practical Course: "Membrane protein expression, purification, 2-D crystallization and imaging" at the Biozentrum, University of Basel, Switzerland.
Instructor in the "Blockkurs in Biophysik und Strukturbiologie" in the image processing and electron crystallography exercises.
Tutoring in "Grundlagen der Ethik" for undergraduate students at the University of Basel, Switzerland.

2005 Instructor in the "Blockkurs in Biophysik und Strukturbiologie" in the image processing and electron crystallography exercises.
Instructor in the "Blockkurs in Biophysik und Strukturbiologie" in the laboratory week course.
Tutoring in "Grundlagen der Ethik" for undergraduate students at the University of Basel, Switzerland.

2006 Instructor in the "Blockkurs in Biophysik und Strukturbiologie" in the image processing and electron crystallography exercises.

Publications

W. Kukulski, A. D. Schenk, U. Johanson, T. Braun, B. L. de Groot, D. Fotiadis, P.

Kjellbom and A. Engel. 2005. The 5 Å Structure of Heterologously Expressed Plant Aquaporin SoPIP2;1. *Journal of Molecular Biology*. 350: 611-616.

W. Kukulski, T. Kaufmann, T. Braun, H. Remigy, D. Fotiadis and A. Engel. 2006. Assessing Structure and Dynamics of Native Membrane Proteins. in: *Structural Biology of Membrane Proteins*. Edited by R. Grisshammer and S. Buchanan. RSC Publishing.

G. A. Signorell, T. C. Kaufmann, W. Kukulski, A. Engel, H. W. Remigy. 2006. Controlled 2D Crystallization of Membrane Proteins Using Methyl-β-Cyclodextrin. *Journal of Structural Biology*. in press.

Oral Presentations

2002 "Purification and 2D Crystallization of PM28A." 4th EU biotech Aquaplugs meeting meeting, Haute- Nendaz, Switzerland.
"Purification and Crystallization of the Plant Aquaporin PM28A." EMBO Course Cryo-Electron Microscopy, EMBL Heidelberg, Germany.

2003 "2D Crystallization of the Plant Aquaporin PM28A." 5th EU biotech Aquaplugs meeting meeting, Aarhus, Denmark.

2004 "Electron Crystallography on the Plant Aquaporin PM28A." NCCR Structural Biology monthly seminar, ETH Zurich, Switzerland.

2005 "The 5 Å Structure of the Plant Aquaporin SoPIP2;1 determined by Electron Crystallography." 4th Conference on Aquaporins, Genval (Brussels), Belgium.